

UCSF

UC San Francisco Electronic Theses and Dissertations

Title

A brainstem circuit mechanism for coordinating the head and eyes during gaze movements

Permalink

<https://escholarship.org/uc/item/3j93j7k1>

Author

Taylor, David

Publication Date

2023

Peer reviewed|Thesis/dissertation

A brainstem circuit mechanism for coordinating the head and eyes during gaze movements

by
David Taylor

DISSERTATION
Submitted in partial satisfaction of the requirements for degree of
DOCTOR OF PHILOSOPHY

in
Neuroscience

in the
GRADUATE DIVISION
of the
UNIVERSITY OF CALIFORNIA, SAN FRANCISCO

Approved:

DocuSigned by:

3A5C1850C2F1412... Michael Brainard
Chair

DocuSigned by:

DocuSigned by: 4CE... Evan Feinberg

DocuSigned by:

DocuSigned by: FEB... Alexandra Nelson

DocuSigned by:

4AF406E430B7472... Massimo Scanziani

Committee Members

Copyright 2023

by

David Taylor

Acknowledgements

I was uncertain what I wanted to do in graduate school, but during my first meeting with Dr. Evan Feinberg I felt immediately at ease discussing research ideas and was excited at the prospect of joining a new lab where I could help plot its early trajectory. Thank you for your mentorship, Evan—your guidance and support have been invaluable throughout my research journey. There were many times when I felt overwhelmed, discouraged, or out of my comfort zone, but your optimism and willingness to try out new ideas encouraged me to persist.

To my collaborator and friend, Sebi, it's hard to express how much I appreciate your role in my PhD journey. Our collaboration began unexpectedly when a last-minute change of plans forced us to collaborate on a winter quarter rotation project. That experience was so fruitful and enjoyable that we went on to do another rotation together, and later, joined the same lab. Throughout the years, I have been constantly inspired by your creativity, optimism, and fearlessness in tackling new challenges. You are an exceptional scientist and your ideas have pushed me to think outside the box and try new approaches, and your friendship has also made this experience far more enjoyable than I could have anticipated. For all of that, I am immensely grateful.

To the wonderful individuals who constitute the Feinberg Lab, both present and past, I extend my heartfelt appreciation. Whether through friendship, advice, or direct contribution on my projects, you were all important to my success and wellbeing.

To the members of my thesis committee—Dr. Michael Brainard, Dr. Alexandra Nelson, and Dr. Massimo Scanziani—and qualifying exam committee—Dr. Jonathan

Horton, Dr. Michael Brainard, Dr. Felice Dunn, and Dr. Vikaas Sohal—thank you very much for your support, guidance, and patience as I navigated graduate school.

To my friends, I am grateful to you all. You've shared in my moments of utmost joy and provided solace during the times of trial.

To my family—Mom, Dad, and Kristen—thank you for your unconditional support, encouragement, and love throughout this journey and the countless things you have done, large and small, that got me to this point.

To my wife and best friend, Tara, I am thankful for you in more ways than I could possibly convey. In brief, thank you for your unwavering support and love—you brought me perspective on what truly matters in life that kept me anchored through the highs and lows of this journey.

And, finally, special thanks to Leia for her mercurial feline affection, Lucy for long walks and insatiable demand for cuddles, and both of these adorable furballs for adding warmth and liveliness to my days while tolerating the occasional testing of their orienting responses to tactile stimuli.

Contributions

Chapter 2 is adapted from the following publication:

Sebastian H. Zahler*, David E. Taylor*, Joey Y. Wong, Julia M. Adams, Evan H. Feinberg. Superior colliculus drives stimulus-evoked directionally biased saccades and attempted head movements in head-fixed mice. eLife. 2021 Dec 31;10:e73081. <https://doi.org/10.7554/eLife.73081>.

*These authors contributed equally.

Chapter 3 is adapted from the following publication:

Sebastian H. Zahler*, David E. Taylor*, Brennan S. Wright, Joey Y. Wong, Varvara A. Shvareva, Yusol A. Park, and Evan H. Feinberg. Hindbrain modules differentially transform activity of single collicular neurons to coordinate movements. Cell. 2023 Jul 6; 186(14): 3062-78. <https://doi.org/10.1016/j.cell.2023.05.031>.

*These authors contributed equally.

A brainstem circuit mechanism for coordinating the head and eyes during gaze movements

David Taylor

Abstract

Many actions involve coordinated movements of multiple body parts. Motor coordination is thought to rely on a hierarchical sequence of computations that transforms overarching movement objectives into specific commands for each body part, but how these hierarchical computations are implemented within anatomical hierarchies remains largely unknown. In Chapter 1, I introduce additional background on motor hierarchies and propose that the motor hierarchy coordinating head-eye gaze shifts could be interrogated in a systematic, stepwise fashion using the genetically tractable mouse model. In Chapter 2, I present work showing that mice make innate, stimulus-evoked gaze movements involving coincident head and eye movements that are mediated by superior colliculus (SC). These findings reveal unexpected flexibility in mouse gaze shifts and provide an experimental paradigm for studying coordinated movement of multiple body parts. In Chapter 3, I present original research that systematically interrogates different levels of the mouse gaze hierarchy. This research unexpectedly reveals that no individual stage of this anatomical hierarchy computes the desired overall displacement. Instead, single SC upper motor neurons specify a mixture of endpoints and displacements for different body parts, with displacements for different body parts computed independently and at distinct anatomical stages.

Table of Contents

Chapter 1: Introduction.....	1
1.2 Figures.....	12
1.3 References.....	13
Chapter 2: Superior colliculus drives stimulus-evoked directionally biased saccades and attempted head movements in mice	25
2.1 Abstract.....	25
2.2 Introduction	26
2.3 Results.....	30
2.4 Discussion.....	45
2.5 Methods	56
2.6 Figures.....	64
2.7 Supplemental Figures	74
2.8 References.....	92
Chapter 3: Hindbrain modules differentially transform activity of single collicular neurons to coordinate movements	100
3.1 Abstract.....	100
3.2 Introduction	101
3.3 Results.....	104
3.4 Discussion.....	118

3.5 Methods	125
3.6 Figures	142
3.7 Supplemental Figures	155
3.8 References.....	166

List of Figures

Figure 1.1: A modular circuit architecture for coordinating the head and eyes.....	12
Figure 2.1: Optogenetic stimulation of the superior colliculus evokes coincident and directionally biased attempted head and eye movements.....	64
Figure 2.2: Mice innately make sound- and touch-evoked gaze shifts	65
Figure 2.3: Sensory-evoked eye and attempted head movements	66
Figure 2.4: Head-eye coupling during spontaneous and touch-evoked gaze shifts	69
Figure 2.5: Saccade and head movement direction, amplitude, and probability depend on initial eye position	71
Figure 2.6: Superior colliculus controls touch-evoked gaze shifts	72
Figure S2.1: Airpuffs evoke horizontal saccades	74
Figure S2.2: Evoked saccades occur within a narrow window after stimulus delivery.....	75
Figure S2.3: Saccade endpoints as a function of initial eye position.....	76
Figure S2.4: Endpoints of airpuff-evoked saccades are ordered according to site of stimulation	77
Figure S2.5: Endpoints and trajectories of sensory-evoked saccades for an additional cohort of mice	78
Figure S2.6: Head-eye coupling for different stimuli.....	80
Figure S2.7: Different head-eye coupling during spontaneous and touch-evoked gaze shifts is not due to differences in saccade start and end points.....	82

Figure S2.8: Head-eye coupling across and within sessions	83
Figure S2.9: Ear- and whisker- airpuff trials matched for attempted head movement amplitude have different saccade endpoints.....	84
Figure S2.10: Gain of head-eye coupling variability across mice	85
Figure S2.11: Saccade amplitude, saccade endpoint, and attempted head movement amplitude binned by initial eye position	86
Figure S2.12: Relationship between initial eye position and saccade probability	87
Figure S2.13: Effects of sensory history and arousal on saccade generation	88
Figure S2.14: Relationship between initial head position and saccade and head movement amplitude	89
Figure S2.15: Controlling for the effects of initial eye position on superior colliculus manipulations.....	90
Figure 3.1: Superior colliculus specifies head displacement and saccade endpoint but not overall gaze displacement in freely moving mice.....	142
Figure 3.2: Mouse superior colliculus comprises topographic maps of head displacement and saccade endpoint	144
Figure 3.3: Tectoreticular neurons drive sensory-guided eye and head movements with stereotyped endpoints and displacements, respectively.....	145
Figure 3.4: Tectoreticular neurons encode stimulus location and head displacement.....	147

Figure 3.5: SC-recipient Gi and PPRF modules drive head movements with stereotyped displacements and saccades with stereotyped endpoints, respectively	149
Figure 3.6: Individual tectoreticular neurons collateralizing to Gi and PPRF drive both head and eye movements	152
Figure 3.7: Saccade tuning emerges in PPRF	153
Figure S3.1: Further characterization of superior colliculus-evoked head and eye movements in freely moving mice and abducens stimulation in head-fixed mice.....	156
Figure S3.2: Further characterization of head and eye movements evoked by SC microstimulation along the anterior-posterior axis	157
Figure S3.3: Tectoreticular recording sites and additional example cells.....	159
Figure S3.4: Responses of tagged SC neurons to airpuffs on one side, responses of untagged SC neurons, and spatial distributions of responses within SC	162
Figure S3.5: Spatial distributions of responses in Gi and PPRF	163
Figure S3.6: Responses of additional Gi and PPRF neurons and movement-aligned responses	164
Figure S3.7: Responses of additional SC-recipient PPRF neurons and movement-aligned responses	165

List of Abbreviations

AAV: Adeno-associated virus

Gi: Gigantocellular nucleus

HSV: Herpes simplex virus

PPRF: Paramedian Pontine Reticular Formation

PMRF: Ponto-medullary reticular formation

SC: Superior Colliculus

VOR: Vestibular ocular reflex

Chapter 1: Introduction

Everyday behaviors often involve the coordinated movements of multiple body parts. For example, plucking fruit off a tree involves shoulder, elbow, and finger movements while scanning a bookshelf for a particular title involves head and eye movements. Each body part possesses its own unique properties and limitations, such as range of motion and starting position, and thus may traverse a distinct trajectory during a coordinated movement. Understanding how the nervous system selects the appropriate movement for each body part needed to compose a unified action remains an important question in neuroscience.

Movement coordination is commonly understood to involve a hierarchical series of computations. For instance, the textbook model for generating coordinated movements depicts that overall movement trajectory is determined before the calculation of each individual body part's movement, such as joint trajectories or muscle activations needed to achieve each joint trajectory (Kandel et al., 2013). Similarly, motor control theory invokes hierarchical frameworks where desired movement trajectories serve as inputs to internal models that generate the motor commands necessary to achieve the desired movement (Kawato, 1999; Miall and Wolpert, 1996; Wolpert et al., 1998). The brain is thought to implement these hierarchical series of computations within an anatomical hierarchy. Neurons near the top of the hierarchy (i.e., further removed from the periphery) specify high-level parameters, such as the overall desired movement, while neurons further down the hierarchy (i.e., closer to the periphery) specify low-level parameters that control the movement of individual body parts.

In accordance with such hierarchical models, the stimulation of neurons higher in the anatomical hierarchy can induce complex coordinated movements involving multiple body parts. For example, electrically stimulating parts of monkey precentral cortex has been shown to reliably elicit complex behaviors, such as driving the hand to the open mouth in a manner suggestive of eating (Graziano et al., 2002; Graziano and Aflalo, 2007). Similarly, optogenetically stimulating genetically defined subpopulations of brainstem neurons in mice can evoke complex whole-body movements, including grooming, rearing, food-handling, and reaching (Ferreira-Pinto et al., 2021; Ruder et al., 2021; Ruder and Arber, 2019). Conversely, when neurons situated lower in the anatomical hierarchy are stimulated, such as those in the spinal cord or cortical areas projecting directly to the spinal cord, more elementary movements are evoked like the contraction of a muscle group by a defined amount (Bizzi et al., 1995; D'Avella et al., 2003; Overduin et al., 2012; Wang et al., 2017).

Although signatures of motor hierarchy are evident throughout the brain, little is known about where and how this hierarchical series of computations is instantiated within these anatomical hierarchies (Diedrichsen et al., 2010; Merel et al., 2019; Todorov and Jordan, 2002). Existing research on hierarchical frameworks has primarily focused on volitional behaviors, such as trained reaching, which involve multiple redundant degrees of freedom that complicate the mapping between high-level and low-level parameters (Diedrichsen et al., 2010; Guo et al., 2015; Merel et al., 2019; Shenoy et al., 2013). Trained reaches have been observed to both reliably achieve goals while still displaying substantial trial-to-trial variability, leading newer models to blur the distinction between motor planning and execution to allow for online feedback control

and course correction (Todorov, 2004; Todorov and Jordan, 2002). Moreover, there is still lively debate on the fundamental response properties and functions of areas involved in volitional movements, such as primary motor cortex (Shenoy et al., 2013). As a consequence, current models of hierarchical motor control remain abstract and lack grounding in specific neural circuits.

Additionally, there are numerous innate behaviors, such as grooming, avoidance, consummation, escape, and gaze shifts, that also require coordination of multiple body parts (Isa et al., 2021; Ruder and Arber, 2019; Shang et al., 2019; Xie et al., 2022). There has been growing interest in examining neural circuits in the context of natural behaviors (Krakauer et al., 2017), facilitated by the development of improved tools to track behavior (Datta et al., 2019; Mathis et al., 2018; Pereira et al., 2020). However, it remains unclear whether the hierarchical principles believed to underlie volitional behaviors can be generalized to all coordinated movements.

Elucidating the mechanisms by which motor hierarchies transform high-level movement objectives into specific motor commands for each body part necessitates a systematic investigation of these neural circuits. Many studies have proposed that upper motor neurons in regions such as motor cortex and superior colliculus (SC) play pivotal roles in this process. Upper motor neurons connect higher centers to controllers in brainstem and spinal cord, and the axons of single upper motor neurons often collateralize to innervate multiple target areas. For instance, corticospinal neurons innervate numerous other structures besides spinal cord, including motor areas like striatum and brainstem (Arber and Costa, 2022; Hooks et al., 2018; Keizer and Kuypers, 1989; Kita and Kita, 2012; Lemon, 2008; Nelson et al., 2021; Ugolini and

Kuypers, 1986; Wang et al., 2017). Similarly, SC motor neurons have branching axons projecting throughout brainstem involved in eye, head, forelimb, and locomotion movements (Grantyn et al., 2004; Isa et al., 2020, 2021; Masullo et al., 2019; Takahashi and Shinoda, 2018). These observations suggest a circuit mechanism whereby individual upper motor neurons encoding higher-order parameters may carry signals to coordinate multiple body parts (Arber and Costa, 2022).

A popular system for investigating movement coordination is the gaze system because of its few degrees of freedom and relatively compact neuroanatomy (Bizzi et al., 1971; Freedman, 2008; Gandhi and Katnani, 2011; Guitton, 1992; Land, 2019; Paré et al., 1994; Sajad et al., 2020). In particular, SC controls head and rapid eye movements (i.e., saccades) across a wide range of species via projections to brainstem (Isa et al., 2021; Isa and Sasaki, 2002; Sparks, 2002), and a series of overlapping maps linking sensory space to movement-related activity enables SC to direct movements toward stimuli (Sparks, 2002, 1986). Early studies in head-restrained monkeys reported that SC encodes a motor map of saccade displacements (vectors) (Robinson, 1972; Schiller and Stryker, 1972), but subsequent experiments in head-free cats and monkeys found that SC stimulation drove coordinated movements of the head and eye such that the magnitude of the overall gaze shift remained constant for a given stimulation site (Freedman et al., 1996; Paré et al., 1994). These findings have contributed to the current model in which the higher-order parameter specified by SC upper motor neurons is overall gaze displacement (Bergeron et al., 2003; Freedman, 2008; Guitton, 1992; Sajad et al., 2020). However, ongoing debate persists regarding where and how

the desired overall gaze displacement is transformed into its component head and eye displacements (Bergeron et al., 2003; Freedman, 2008; Sajad et al., 2020).

While our knowledge of gaze and gaze circuitry has primarily been derived from species with high-acuity vision, such as primates and cats, the mouse model offers distinct methodological advantages due to its mature set of genetic and viral tools that allow for precise manipulation and recording of cell-type specific neuronal subpopulations, enabling a more detailed examination of the neural circuitry responsible for coordinated head-eye gaze movements (Cui et al., 2013; Gradinaru et al., 2010; Lima et al., 2009). Furthermore, mice have emerged as an increasingly important model organism in vision research (Huberman and Niell, 2011) and rely on vision to execute a diverse array of appetitive, avoidance, discrimination, and attentional behaviors (Burgess et al., 2017; Hoy et al., 2016; Land and Nilsson, 2012; Meyer et al., 2020; Michaiel et al., 2020; Yilmaz and Meister, 2013). Although mice lack the high-acuity retinal specializations found in primates and cats (i.e., fovea centralis and area centralis, respectively), their retinae exhibit subtle asymmetric distributions and densities of photoreceptor and retinal ganglion cell subtypes (Baden et al., 2013; Bleckert et al., 2014). Additionally, visual centers such as the superior colliculus (SC) and visual cortex in mice display variations in magnification factor, receptive field sizes, and response tuning across the visual field (de Malmazet et al., 2018; Drager and Hubel, 1976; Feinberg and Meister, 2015; Li et al., 2020; van Beest et al., 2021). These modest specializations may potentially confer advantages to specific gaze postures during natural behavior. Despite their increasing relevance in vision research, the gaze

movement strategies employed by mice and the neural circuitry underpinning these movements remain incompletely understood.

Neuroanatomical and functional investigations suggest that much of the neural circuitry responsible for generating gaze shifts may be conserved in mice (May, 2006; Sparks, 2002, 1986). Electrical stimulation in SC of head-fixed mice generates contraversive (toward the opposite side) saccades that increase in size as the stimulation site moves posteriorly, mirroring the observed saccade motor map in primates and cats (Sakatani and Isa, 2008; Wang et al., 2015). Similarly, optogenetic stimulation of genetically defined SC motor output neurons in unrestrained mice produces a comparable motor map of head movement (Masullo et al., 2019). Mouse SC also exhibits sensory maps of visual, auditory, and somatosensory space that roughly align with these motor maps, akin to findings in monkeys and cats (Drager and Hubel, 1976, 1975). Despite these similarities, the role of mouse SC in generating coordinated head and eye movements has not been evaluated while simultaneously recording both body parts, nor have head and eye movements been analyzed in conjunction with the animal's initial body posture. Consequently, it remains uncertain whether mouse SC encodes the same parameters as primate and cat SC (i.e., overall gaze displacement).

The output layers of SC send projections to various sites throughout the contralateral ponto-medullary reticular formation (PMRF), a heterogeneous brainstem structure housing circuits responsible for controlling saccades and head movements (Grantyn et al., 2004). In primates and cats, saccades are controlled by what is collectively known as the saccade generator circuits. Horizontal saccades initiate when SC tectoreticular neurons engage excitatory burst neurons (EBNs) situated in the

paramedian pontine reticular formation (PPRF). These EBNs, in turn, project to neurons in the abducens nucleus, controlling the lateral rectus muscle (Sparks, 2002). In mice, many of the homologs to neurons comprising the saccade generator circuit have yet to be fully substantiated, with the only known similarity being the abducens nucleus, which displays properties akin to those in other species (Stahl et al., 2015; Stahl and Thumser, 2012). Head movements by primates and cats can be generated by stimulating reticulospinal neurons in the gigantocellular reticular nucleus (Gi), which both receive input from SC and project to spinal motoneurons in the neck that control horizontal head movements (Freedman, 2008; Isa and Sasaki, 2002). In mice, potential homologs to these neurons were identified via optogenetic stimulation of genetically defined populations of neurons in Gi, revealing subpopulations that project to the cervical spinal cord and specifically induce horizontal head movements (Cregg et al., 2020; Usseglio et al., 2020). One such subpopulation, reticulospinal V2a neurons, also received direct input from neurons in SC, indicating that the SC-Gi pathway might be responsible for generating SC-mediated head movements in mice (Usseglio et al., 2020).

Despite the similarities between the gaze circuitry of mice and foveates, it is believed that gaze movements in mice (and other afoveate species) differ significantly. In primates and other foveate species, gaze shifts often involve tightly coupled directed saccades and head movements making them suitable for studying how motor hierarchies transform high-level movement objectives into specific motor commands for each body part (Bizzi et al., 1972; Freedman, 2008; Lee, 1999; Zangemeister and Stark, 1982). In contrast, the prevailing view holds that afoveate species execute gaze shifts primarily driven by head movements that are followed by eye movements to stabilize

vision (Land, 2019; Land and Nilsson, 2012). Recent studies tracking head and eye movements in freely moving mice support this notion, where spontaneous and visually evoked mouse gaze shifts align with this description (Meyer et al., 2020, 2018; Michael et al., 2020; Payne and Raymond, 2017). Specifically, during a gaze shift, slow eye movements stabilize the retinal image by counteracting the rotation of the head. These slow eye movements are punctuated with fast saccadic eye movements in the opposite direction that recenter the eyes in the orbits before they reach the edge of their orbital range. These recentering saccades, also known as "compensatory" saccades or the quick phase of nystagmus, are believed to be driven by vestibular or optokinetic signals acting on circuits in the brainstem (Curthoys, 2002; Hepp et al., 1993; Kitama et al., 1995; Meyer et al., 2020; Michael et al., 2020; Payne and Raymond, 2017). As a result, the head and eye components of mouse gaze shifts are only indirectly coupled, with head movements triggering gaze-stabilizing eye reflexes.

However, there are two observations that are inconsistent with the idea that all saccades in mice exclusively serve to recenter the eyes and compensate for head movements. First, mouse saccades are not solely a result of vestibular or optokinetic cues, as head-fixed mice lacking these signals still generate saccades, although infrequently (~7 per minute) (Sakatani and Isa, 2007). Second, neuroanatomical and functional evidence suggest that the circuits that underlie directed saccades are conserved in mice. Specifically, microstimulation of mouse SC showed that it contains a topographic map of saccade and head movement direction and amplitude roughly aligned with maps of visual, auditory, and somatosensory space (Drager and Hubel, 1976, 1975; Masullo et al., 2019; Wang et al., 2015). These maps resemble those

believed to underlie primates' and cats' ability to make saccade-led gaze shifts towards stimuli of these modalities (Sparks, 2002, 1986).

Surprisingly, mice have not been observed to reliably make saccades in response to sensory stimuli. Previous studies in head-fixed mice observed occasional undirected saccades in response to extensive changes in the visual environment (Samonds et al., 2018) and visually guided saccades only after weeks of training and at long latencies (~700 ms, roughly three times that of primates) (Itokazu et al., 2018). In contrast, humans and other foveates have been shown to innately make targeted saccades towards salient stimuli from many modalities, including visual, auditory, and somatosensory (Kandel et al., 2013; Land, 2019; Land and Nilsson, 2012; Liversedge et al., 2012; Walls, 1962). Furthermore, it's been shown that the coupling between head and eye movements varies depending on the individual, species, and context (Goldring et al., 1996; Populin, 2006; Ruhland et al., 2013; Tollin et al., 2005). This coupling can also vary depending on the stimulus modality (Populin and Rajala, 2011; Ruhland et al., 2013). The fact that mice have not been observed to produce gaze shifts, stimulus driven or otherwise, composed of saccades simultaneous with or preceding head movements may reflect the limited scope of contexts in which gaze movements have been studied in mice.

To advance our understanding of mouse gaze shifts and assess the mouse gaze system's suitability as a model for studying coordinated movements, we sought a condition in which mice innately generate gaze shifts comprising tightly coupled saccades and head movements that had been previously overlooked. In Chapter 2, I present original research where we conducted experiments using head-fixed mice and

presented a battery of stimuli from various modalities at precise craniotopic locations. This approach allowed us to systematically determine whether these stimuli elicited gaze shifts and evaluate the head-eye coupling in the absence of vestibular and optokinetic cues. We observed that mice make innate, stimulus-evoked directed gaze movements involving simultaneous head and eye movements that are mediated by SC. These findings resolve a previous discrepancy between mouse neuroanatomy and behavior, and they offer a novel behavioral model to investigate the circuitry underlying gaze control.

As discussed earlier, motor coordination is thought to be implemented through a series of computational hierarchies that are instantiated within anatomical brain hierarchies, but the location and mechanistic implementation of these hierarchies remains poorly understood and circuit models remain abstract. In Chapter 3, I will return to the topic of motor hierarchies and present original research that systematically investigates the motor circuits underlying a relatively simple movement—coordinated head-eye gaze movements—in order to better understand the mechanisms of coordinated movements (Figure 1.1). We find that mouse SC upper motor neurons unexpectedly do not specify the overall gaze displacement, but instead specify the displacement for the head but only the endpoint for the eyes. Subsequent analyses found that single SC upper motor neurons innervate two separate hindbrain populations (PPRF and Gi) that drive head movements with fixed displacements and eye movements with fixed endpoints, respectively. Neural recordings showed that head displacement information emerges in SC, whereas saccade information does not emerge until the hindbrain. Our study thus reveals that overall displacements are not

computed at any anatomical stage within the mouse gaze hierarchy. Instead, displacements for different body parts are independently computed at distinct anatomical stages, revealing unexpected diversity in the mechanisms of coordinated movements.

1.2 FIGURES

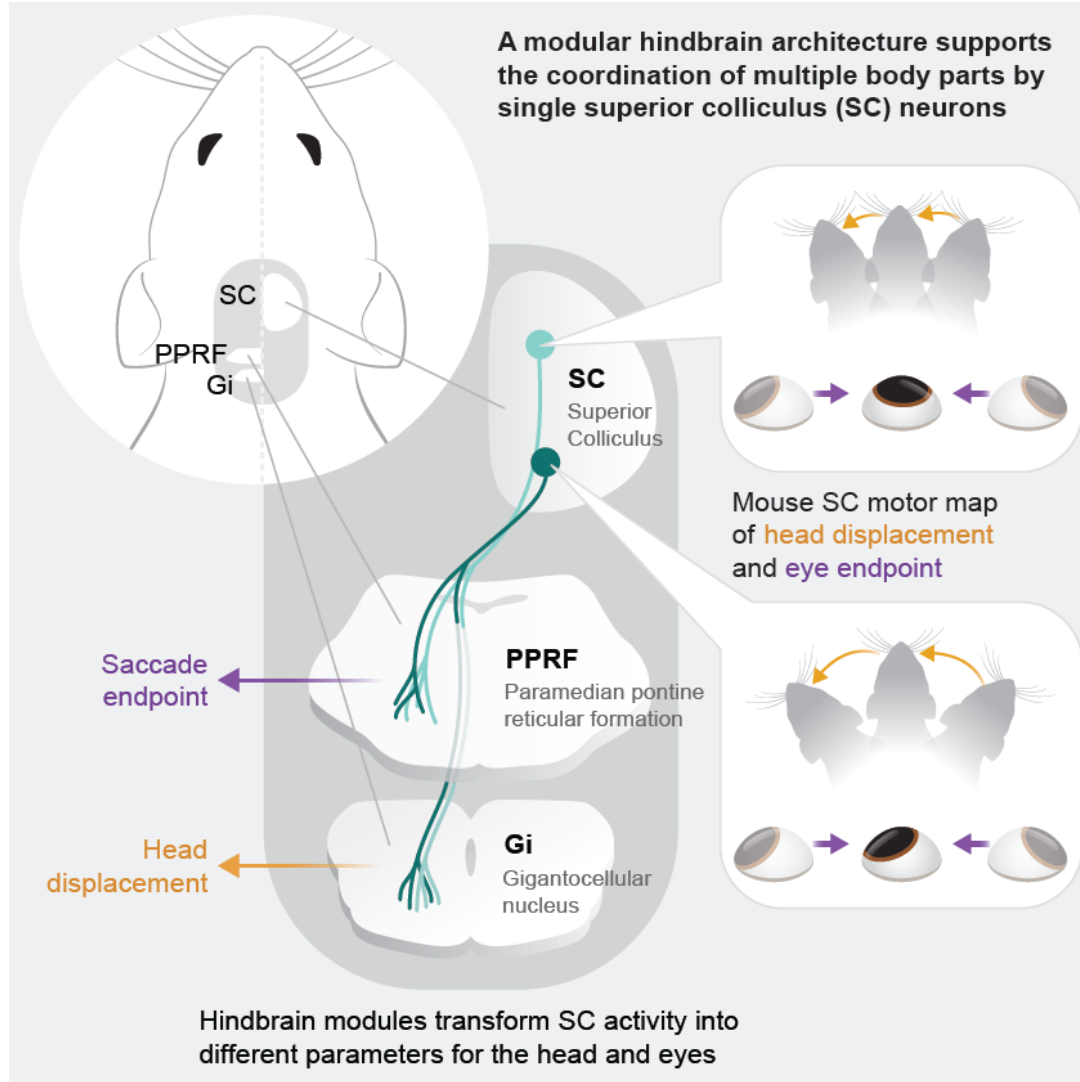


Figure 1.1: A modular circuit architecture for coordinating the head and eyes
A, Schematic of the main findings from Chapter 2. Mouse SC comprises superimposed topographic maps of head movement displacements and saccade endpoints. To achieve this, SC neurons encode head displacement and stimulus location information, and their activity is differentially transformed by downstream brainstem modules, Gi and PPRF, into head displacement and saccade endpoint, respectively. Adapted from Zahler, Taylor, et al., 2023.

1.3 REFERENCES

- Arber, S., Costa, R.M., 2022. Networking brainstem and basal ganglia circuits for movement. *Nature Reviews Neuroscience* 23, 342–360.
- Baden, T., Schubert, T., Chang, L., Wei, T., Zaichuk, M., Wissinger, B., Euler, T., 2013. A tale of two retinal domains: Near-Optimal sampling of achromatic contrasts in natural scenes through asymmetric photoreceptor distribution. *Neuron* 80, 1206–1217.
- Bergeron, A., Matsuo, S., Guitton, D., 2003. Superior colliculus encodes distance to target, not saccade amplitude, in multi-step gaze shifts. *Nature Neuroscience* 6, 404–413.
- Bizzi, E., Giszter, S.F., Loeb, E., Mussa-Ivaldi, F.A., Saltiel, P., 1995. Modular organization of motor behavior in the frog's spinal cord. *Trends in Neurosciences* 18, 442–446.
- Bizzi, E., Kalil, R., Tagliasco, V., 1971. Eye-head coordination in monkeys: evidence for centrally patterned organization. *Science* 173, 452–454.
- Bizzi, E., Kalil, R.E., Morasso, P., 1972. Two modes of active eye-head coordination in monkeys. *Brain Research* 40, 45–48.
- Bleckert, A., Schwartz, G.W., Turner, M.H., Rieke, F., Wong, R.O.L., 2014. Visual space is represented by nonmatching topographies of distinct mouse retinal ganglion cell types. *Current Biology* 24, 310–315.

- Burgess, C.P., Lak, A., Steinmetz, N.A., Zatzka-Haas, P., Bai Reddy, C., Jacobs, E.A.K., Linden, J.F., Paton, J.J., Ranson, A., Schröder, S., Soares, S., Wells, M.J., Wool, L.E., Harris, K.D., Carandini, M., 2017. High-Yield Methods for Accurate Two-Alternative Visual Psychophysics in Head-Fixed Mice. *Cell Reports* 20, 2513–2524.
- Cregg, J.M., Leiras, R., Montalant, A., Wanken, P., Wickersham, I.R., Kiehn, O., 2020. Brainstem neurons that command mammalian locomotor asymmetries. *Nature Neuroscience* 23, 730–740.
- Cui, G., Jun, S.B., Jin, X., Pham, M.D., Vogel, S.S., Lovinger, D.M., Costa, R.M., 2013. Concurrent activation of striatal direct and indirect pathways during action initiation. *Nature* 494, 238–242.
- Curthoys, I.S., 2002. Generation of the quick phase of horizontal vestibular nystagmus. *Experimental Brain Research* 143, 397–405.
- Datta, S.R., Anderson, D.J., Branson, K., Perona, P., Leifer, A., 2019. Computational Neuroethology: A Call to Action. *Neuron* 104, 11–24.
- D’Avella, A., Saltiel, P., Bizzi, E., 2003. Combinations of muscle synergies in the construction of a natural motor behavior. *Nature Neuroscience* 6, 300–308.
- de Malmazet, D., Kühn, N.K., Farrow, K., 2018. Retinotopic Separation of Nasal and Temporal Motion Selectivity in the Mouse Superior Colliculus. *Current Biology* 28, 2961-2969.e4.

- Diedrichsen, J., Shadmehr, R., Ivry, R.B., 2010. The coordination of movement: optimal feedback control and beyond. *Trends in Cognitive Sciences* 14, 31–39.
- Drager, U.C., Hubel, D.H., 1976. Topography of visual and somatosensory projections to mouse superior colliculus. *Journal of Neurophysiology* 39, 91–101.
- Drager, U.C., Hubel, D.H., 1975. Responses to visual stimulation and relationship between visual, auditory, and somatosensory inputs in mouse superior colliculus. *Journal of neurophysiology* 38, 690–713.
- Feinberg, E.H., Meister, M., 2015. Orientation columns in the mouse superior colliculus. *Nature* 519, 229–232.
- Ferreira-Pinto, M.J., Kanodia, H., Falasconi, A., Sigrist, M., Esposito, M.S., Arber, S., 2021. Functional diversity for body actions in the mesencephalic locomotor region. *Cell* 184, 4564-4578.e18.
- Freedman, E.E.G., Stanford, T.R.T., Sparks, D.L.D., 1996. Combined eye-head gaze shifts produced by electrical stimulation of the superior colliculus in rhesus monkeys. *Journal of Neurophysiology* 76, 927–952.
- Freedman, E.G., 2008. Coordination of the Eyes and Head during Visual Orienting. *Experimental brain research. Experimentelle Hirnforschung. Experimentation cerebrale* 190, 369.
- Gandhi, N.J., Katnani, H.A., 2011. Motor functions of the superior colliculus. *Annual Review of Neuroscience* 34, 205–231.

- Goldring, J.E., Dorris, M.C., Corneil, B.D., Ballantyne, P.A., Munoz, D.P., 1996. Combined eye-head gaze shifts to visual and auditory targets in humans. *Experimental Brain Research* 111, 68–78.
- Gradinaru, V., Zhang, F., Ramakrishnan, C., Mattis, J., Prakash, R., Diester, I., Goshen, I., Thompson, K.R., Deisseroth, K., 2010. Molecular and Cellular Approaches for Diversifying and Extending Optogenetics. *Cell* 141, 154–165.
- Grantyn, A., Moschovakis, A.K., Kitama, T., 2004. Control of orienting movements: role of multiple tectal projections to the lower brainstem. *Progress in brain research* 143, 423–438.
- Graziano, M.S.A., Aflalo, T.N., 2007. Mapping Behavioral Repertoire onto the Cortex. *Neuron* 56, 239–251.
- Graziano, M.S.A., Taylor, C.S.R., Moore, T., 2002. Complex movements evoked by microstimulation of precentral cortex. *Neuron* 34, 841–851.
- Guitton, D., 1992. Control of eye-head coordination during orienting gaze shifts. *Trends in Neurosciences* 15, 174–179.
- Guo, J.Z., Graves, A.R., Guo, W.W., Zheng, J., Lee, A., Rodríguez-González, J., Li, N., Macklin, J.J., Phillips, J.W., Mensh, B.D., Branson, K., Hantman, A.W., 2015. Cortex commands the performance of skilled movement. *eLife* 4.
- Hepp, K., Opstal, V.A.J., Straumann, D., Hess, B.J., Henn, V., 1993. Monkey superior colliculus represents rapid eye movements in a two-dimensional motor map. *Journal of Neurophysiology* 69, 965–979.

- Hooks, B.M., Papale, A.E., Paletzki, R.F., Feroze, M.W., Eastwood, B.S., Couey, J.J., Winnubst, J., Chandrashekar, J., Gerfen, C.R., 2018. Topographic precision in sensory and motor corticostriatal projections varies across cell type and cortical area. *Nature Communications* 9.
- Hoy, J.L., Yavorska, I., Wehr, M., Niell, C.M., 2016. Vision Drives Accurate Approach Behavior during Prey Capture in Laboratory Mice. *Current Biology* 26, 3046–3052.
- Huberman, A.D., Niell, C.M., 2011. What can mice tell us about how vision works? *Trends in Neurosciences* 34, 464–473.
- Isa, K., Sooksawate, T., Kobayashi, Kenta, Kobayashi, Kazuto, Redgrave, P., Isa, T., 2020. Dissecting the Tectal Output Channels for Orienting and Defense Responses. *eNeuro* 7, 1–18.
- Isa, T., Marquez-Legorreta, E., Grillner, S., Scott, E.K., 2021. The tectum/superior colliculus as the vertebrate solution for spatial sensory integration and action. *Current Biology* 31, R741–R762.
- Isa, T., Sasaki, S., 2002. Brainstem control of head movements during orienting; Organization of the premotor circuits. *Progress in Neurobiology* 66, 205–241.
- Kandel, E.R., Schwartz, J.H., Jessell, T.M., Siegelbaum, S.A., Hudspeth, A.J., 2013. *Principles of Neural Science, Fifth Edition*, 2013.
- Kawato, M., 1999. Internal models for motor control and trajectory planning. *Current Opinion in Neurobiology* 9, 718–727.

- Keizer, K., Kuypers, H.G.J.M., 1989. Distribution of corticospinal neurons with collaterals to the lower brain stem reticular formation in monkey (*Macaca fascicularis*). *Experimental Brain Research* 74, 311–318.
- Kita, T., Kita, H., 2012. The subthalamic nucleus is one of multiple innervation sites for long-range corticofugal axons: a single-axon tracing study in the rat. *The Journal of Neuroscience* 32, 5990–5999.
- Kitama, T., Ohki, Y., Shimazu, H., Tanaka, M., Yoshida, K., 1995. Site of interaction between saccade signals and vestibular signals induced by head rotation in the alert cat: functional properties and afferent organization of burster-driving neurons. *Journal of Neurophysiology* 74, 273–287.
- Krakauer, J.W., Ghazanfar, A.A., Gomez-Marin, A., Maclver, M.A., Poeppel, D., 2017. Neuroscience Needs Behavior: Correcting a Reductionist Bias. *Neuron* 93, 480–490.
- Land, M.F., 2019. The Evolution of Gaze Shifting Eye Movements, in: *Current Topics in Behavioral Neurosciences*. pp. 3–11.
- Land, M.F., Nilsson, D.-E., 2012. *Animal Eyes*, Oxford Animal Biology Series. Oxford University Press.
- Lee, C., 1999. Eye and head coordination in reading: roles of head movement and cognitive control. *Vision Research* 39, 3761–3768.
- Lemon, R.N., 2008. Descending pathways in motor control. *Annual Review of Neuroscience* 31, 195–218.

- Li, Y. tang, Turan, Z., Meister, M., 2020. Functional Architecture of Motion Direction in the Mouse Superior Colliculus. *Current Biology* 30, 3304-3315.e4.
- Lima, S.Q., Hromádka, T., Znamenskiy, P., Zador, A.M., 2009. PINP: A New Method of Tagging Neuronal Populations for Identification during In Vivo Electrophysiological Recording. *PLoS ONE* 4, 6099.
- Liversedge, S.P., Gilchrist, I.D., Everling, S., 2012. The Oxford Handbook of Eye Movements, *The Oxford Handbook of Eye Movements*. Oxford University Press, Oxford.
- Masullo, L., Mariotti, L., Alexandre, N., Freire-Pritchett, P., Boulanger, J., Tripodi, M., 2019. Genetically defined functional modules for spatial orienting in the mouse superior colliculus. *Current Biology* 1–13.
- Mathis, A., Mamidanna, P., Cury, K.M., Abe, T., Murthy, V.N., Mathis, M.W., Bethge, M., 2018. DeepLabCut: markerless pose estimation of user-defined body parts with deep learning. *Nature Neuroscience* 21, 1281–1289.
- May, P.J., 2006. The mammalian superior colliculus: Laminar structure and connections. *Progress in Brain Research* 151, 321–378.
- Merel, J., Botvinick, M., Wayne, G., 2019. Hierarchical motor control in mammals and machines. *Nature Communications* 10, 1–12.
- Meyer, A.F., O'Keefe, J., Poort, J., 2020. Two Distinct Types of Eye-Head Coupling in Freely Moving Mice. *Current Biology* 30, 2116-2130.e6.

- Meyer, A.F., Poort, J., O'Keefe, J., Sahani, M., Linden, J.F., 2018. A Head-Mounted Camera System Integrates Detailed Behavioral Monitoring with Multichannel Electrophysiology in Freely Moving Mice. *Neuron* 100, 46-60.e7.
- Miall, R.C., Wolpert, D.M., 1996. Forward models for physiological motor control. *Neural Networks* 9.
- Michaël, A.M.M., Abe, E.T.T.T.T., Niell, C.M.M., 2020. Dynamics of gaze control during prey capture in freely moving mice. *eLife* 9, 1–27.
- Nelson, A., Abdelmesih, B., Costa, R.M., 2021. Corticospinal populations broadcast complex motor signals to coordinated spinal and striatal circuits. *Nature Neuroscience* 24, 1721–1732.
- Overduin, S.A., d'Avella, A., Carmena, J.M., Bizzi, E., 2012. Microstimulation Activates a Handful of Muscle Synergies. *Neuron* 76, 1071–1077.
- Paré, M., Crommelinck, M., Guitton, D., 1994. Gaze shifts evoked by stimulation of the superior colliculus in the head-free cat conform to the motor map but also depend on stimulus strength and fixation activity. *Experimental brain research* 101, 123–139.
- Payne, H.L., Raymond, J.L., 2017. Magnetic eye tracking in mice. *eLife* 6, 1–24.
- Pereira, T.D., Shaevitz, J.W., Murthy, M., 2020. Quantifying behavior to understand the brain. *Nat Neurosci* 23, 1537–1549.
- Populin, L.C., 2006. Monkey sound localization: Head-restrained versus head-unrestrained orienting. *Journal of Neuroscience* 26, 9820–9832.

- Populin, L.C., Rajala, A.Z., 2011. Target modality determines eye-head coordination in nonhuman primates: Implications for gaze control. *Journal of Neurophysiology* 106, 2000–2011.
- Robinson, D.A., 1972. Eye movements evoked by collicular stimulation in the alert monkey. *Vision Research* 12, 1795–1808.
- Ruder, L., Arber, S., 2019. Brainstem Circuits Controlling Action Diversification. *Annual Review of Neuroscience* 42, 485–504.
- Ruder, L., Schina, R., Kanodia, H., Valencia-Garcia, S., Pivetta, C., Arber, S., 2021. A functional map for diverse forelimb actions within brainstem circuitry. *Nature* 590, 445–450.
- Ruhland, J.L., Yin, T.C.T., Tollin, D.J., 2013. Gaze shifts to auditory and visual stimuli in cats. *JARO - Journal of the Association for Research in Otolaryngology* 14, 731–755.
- Sajad, A., Sadeh, M., Crawford, J.D., 2020. Spatiotemporal transformations for gaze control. *Physiological Reports* 8.
- Sakatani, T., Isa, T., 2008. Superior Colliculus and Saccade Generation in Mice, in: Chalupa, L., Williams, R. (Eds.), *Eye, Retina, and Visual System of the Mouse*. MIT Press.
- Sakatani, T., Isa, T., 2007. Quantitative analysis of spontaneous saccade-like rapid eye movements in C57BL/6 mice. *Neuroscience Research* 58, 324–331.

- Schiller, P.H., Stryker, M., 1972. Single-unit recording and stimulation in superior colliculus of the alert rhesus monkey. *Journal of Neurophysiology* 35, 915–924.
- Shang, C., Liu, A., Li, D., Xie, Z., Chen, Z., Huang, M., Li, Y., Wang, Y., Shen, W.L., Cao, P., 2019. A subcortical excitatory circuit for sensory-triggered predatory hunting in mice. *Nature Neuroscience* 22, 909–920.
- Shenoy, V.K., Sahani, M., Churchland, M.M., 2013. Cortical Control of Arm Movements: A Dynamical Systems Perspective. *Annual Review of Neuroscience* 36, 337–359.
- Sparks, D.L., 2002. The brainstem control of saccadic eye movements. *Nature Reviews Neuroscience* 3, 952–964.
- Sparks, D.L., 1986. Translation of sensory signals into commands for control of saccadic eye movements: Role of primate superior colliculus. *Physiological Reviews* 66, 118–171.
- Stahl, J.S., Thumser, Z.C., 2012. Dynamics of abducens nucleus neurons in the awake mouse. *Journal of Neurophysiology* 108, 2509–2523.
- Stahl, J.S., Thumser, Z.C., May, P.J., Andrade, F.H., Anderson, S.R., Dean, P., 2015. Mechanics of mouse ocular motor plant quantified by optogenetic techniques. *Journal of Neurophysiology* 114, 1455–1467.
- Takahashi, M., Shinoda, Y., 2018. Brain Stem Neural Circuits of Horizontal and Vertical Saccade Systems and their Frame of Reference. *Neuroscience* 392, 281–328.

- Todorov, E., 2004. Optimality principles in sensorimotor control. *Nature Neuroscience* 7, 907–915.
- Todorov, E., Jordan, M.I., 2002. Optimal feedback control as a theory of motor coordination. *Nature Neuroscience* 5, 1226–1235.
- Tollin, D.J., Populin, L.C., Moore, J.M., Ruhland, J.L., Yin, T.C.T., 2005. Sound-localization performance in the cat: The effect of restraining the head. *Journal of Neurophysiology* 93, 1223–1234.
- Ugolini, G., Kuypers, H.G.J.M., 1986. Collaterals of corticospinal and pyramidal fibres to the pontine grey demonstrated by a new application of the fluorescent fibre labelling technique. *Brain Research* 365, 211–227.
- Usseglio, G., Gatier, E., Heuzé, A., Hérent, C., Bouvier, J., 2020. Control of Orienting Movements and Locomotion by Projection-Defined Subsets of Brainstem V2a Neurons. *Current Biology* 30, 4665-4681.e6.
- van Beest, E.H., Mukherjee, S., Kirchberger, L., Schnabel, U.H., van der Togt, C., Teeuwen, R.R.M.M., Barsegyan, A., Meyer, A.F., Poort, J., Roelfsema, P.R., Self, M.W., 2021. Mouse visual cortex contains a region of enhanced spatial resolution. *Nature Communications* 12, 1–17.
- Walls, G.L., 1962. The evolutionary history of eye movements. *Vision Research* 2, 69–80.

- Wang, L., Liu, M., Segraves, M.A., Cang, J., 2015. Visual experience is required for the development of eye movement maps in the mouse superior colliculus. *Journal of Neuroscience* 35, 12281–12286.
- Wang, X., Liu, Y., Li, X., Zhang, Z., Yang, H., Zhang, Yu, Williams, P.R., Alwahab, N.S.A., Kapur, K., Yu, B., Zhang, Yiming, Chen, M., Ding, H., Gerfen, C.R., Wang, K.H., He, Z., 2017. Deconstruction of corticospinal circuits for goal-directed motor skills. *Cell* 171, 440.
- Wolpert, D.M., Miall, R.C., Kawato, M., 1998. Internal models in the cerebellum. *Trends in Cognitive Sciences* 2, 338–347.
- Xie, Z., Li, D., Cheng, X., Pei, Q., Gu, H., Tao, T., Huang, M., Shang, C., Geng, D., Zhao, M., Liu, A., Zhang, C., Zhang, F., Ma, Y., Cao, P., 2022. A brain-to-spinal sensorimotor loop for repetitive self-grooming. *Neuron* 110, 874-890.e7.
- Yilmaz, M., Meister, M., 2013. Rapid innate defensive responses of mice to looming visual stimuli. *Current Biology* 23, 2011–2015.
- Zangemeister, W.H., Stark, L., 1982. Types of gaze movement: Variable interactions of eye and head movements. *Experimental Neurology* 77, 563–577.

Chapter 2: Superior colliculus drives stimulus-evoked directionally biased saccades and attempted head movements in mice

2.1 ABSTRACT

Animals investigate their environments by directing their gaze towards salient stimuli. In the prevailing view, mouse gaze shifts entail head rotations followed by brainstem-mediated eye movements, including saccades to reset the eyes. These “recentering” saccades are attributed to head movement-related vestibular cues. However, microstimulating mouse superior colliculus (SC) elicits directed head and eye movements resembling SC-dependent sensory-guided gaze shifts in other species, suggesting that mouse gaze shifts may be more flexible than has been recognized. We investigated this possibility by tracking eye and attempted head movements in a head-fixed preparation that eliminates head movement-related sensory cues. We found tactile stimuli evoke directionally biased saccades coincident with attempted head rotations. Differences in saccade endpoints across stimuli are associated with distinct stimulus-dependent relationships between initial eye position and saccade direction and amplitude. Optogenetic perturbations revealed SC drives these gaze shifts. Thus, head-fixed mice make sensory-guided, SC-dependent gaze shifts involving coincident, directionally biased saccades and attempted head movements. Our findings uncover flexibility in mouse gaze shifts and provide a foundation for studying head-eye coupling.

2.2 INTRODUCTION

Natural environments are complex and dynamic, and animals frequently redirect their gaze to scrutinize salient sensory stimuli. Gaze shifts employ head and eye movement coupling strategies that depend on context and can vary between species (Goldring et al., 1996; Land, 2019; Land and Nilsson, 2012; Populin, 2006; Populin and Rajala, 2011; Populin et al., 2004a; Ruhland et al., 2013; Tollin et al., 2005). Mice are an increasingly important model organism in vision research, yet the strategies they use to shift their gaze remain incompletely understood. Revealing these strategies is essential to understanding mouse visual ethology and the underlying neural mechanisms.

The prevailing view holds that species whose retinae lack high-acuity specializations (foveates) such as mice generate gaze shifts driven by head movements and followed by “recentering” saccades (Land and Nilsson, 2012). Indeed, recent studies tracking head and eye movements in freely moving mice found that spontaneous and visually evoked mouse gaze shifts matched this description (Meyer et al., 2018, 2020; Michaiel et al., 2020; Payne and Raymond, 2017). Specifically, during a gaze shift, slow eye movements stabilize the retinal image by countering the rotation of the head and are punctuated by fast saccadic eye movements to recenter the eyes in the orbits as they approach the end of their range of motion. These recentering saccades—also known as “compensatory” saccades or the quick phase of nystagmus—are centripetal, occur in the direction of the head movement, and are thought to be driven by vestibular or optokinetic signals acting on circuits in brainstem (Curthoys, 2002; Hepp et al., 1993; Kitama et al., 1995; Meyer et al., 2020; Michaiel et al., 2020;

Payne and Raymond, 2017). These recent observations have buttressed the view that gaze shifts in mice and other afoveates are led by head movements, with eye movements made only to compensate for the effects of head movements. In contrast, primates and other foveate species are capable of an additional form of gaze shift led by directed saccades, with or without directed head movements, to redirect their gaze towards salient stimuli (Bizzi et al., 1972; Freedman, 2008; Lee, 1999; Zangemeister and Stark, 1982). Directed saccades differ from recentering saccades in that they have endpoints specified by the location of the stimulus (and are therefore often centrifugally directed), typically occur simultaneously with head movements during gaze shifts, and are driven by midbrain circuits, particularly the superior colliculus (SC). To date, there is no behavioral evidence that mice or any afoveate species generate directed saccades or gaze shifts not initiated by head movements.

However, three observations are inconsistent with the model that all saccades in mice are exclusively recentering and made to compensate for head movements. First, mouse saccades are not only a product of vestibular or optokinetic cues, because head-fixed mice, in which these signals do not occur, generate saccades, albeit less frequently. Second, neuroanatomical and functional studies suggest that the circuits that underlie directed saccades are conserved in mice (May, 2006; Sparks, 1986, 2002). Specifically, microstimulation of the mouse superior colliculus (SC) showed that it contains a topographic map of saccade and head movement direction and amplitude (Masullo et al., 2019; Wang et al., 2015) roughly aligned with maps of visual, auditory, and somatosensory space (Drager and Hubel, 1975, 1976). These SC sensory and motor maps resemble those believed to underlie primates' and cats' ability to make

gaze shifts led by directed saccades towards stimuli of these modalities (Sparks, 1986, 2002). Third, saccade-like eye movements occurring in the absence of head movements have occasionally been observed in freely moving mice, albeit infrequently and usually in close proximity to head movements (Meyer et al., 2018, 2020; Michael et al., 2020).

We therefore hypothesized that mice innately generate gaze shifts that incorporate directionally biased saccades. We predicted that this ability was obscured in previous studies for several reasons. First, in freely moving mice it is difficult to uncouple the contributions of reafferent vestibular and optokinetic inputs from those of exafferent (extrinsic) sensory inputs to saccade generation. Second, previous analyses in mice were mostly confined to spontaneous or visually guided gaze shifts, and there is evidence in humans, non-human primates, and cats that gaze shifts in response to different sensory modalities can involve distinct head-eye coupling strategies (Goldring et al., 1996; Populin, 2006; Populin and Rajala, 2011; Populin et al., 2004a; Ruhland et al., 2013; Tollin et al., 2005). Third, in freely moving mice it is difficult to present stimuli in specific craniotopic locations. We therefore reasoned that by using a head-fixed preparation both to eliminate vestibular and optokinetic cues and to present stimuli of different modalities at precise craniotopic locations, we could systematically determine whether mice are capable of gaze shifts not initiated by head movements and involving saccades whose endpoints depend on stimulus location and show different coupling to head movements. We found that tactile stimuli evoke saccades whose endpoints depend on stimulus location, that these saccades are coincident with attempted head rotations, and that these touch-evoked gaze shifts are SC-dependent. Together, these

results resolve an apparent discrepancy between mouse neuroanatomy and behavior, demonstrating that head-fixed mice are capable of generating gaze shifts involving directionally biased saccades coincident with attempted head movements.

2.3 RESULTS

Stimulus-evoked gaze shifts in head-restrained mice

Previous studies established that SC microstimulation or optogenetic stimulation evoke both head and eye movements and that these movements roughly match the topographic map of sensory spatial receptive fields within SC, with each SC hemisphere driving contraversive movements whose amplitudes are larger for more posterior stimulation sites (Masullo et al., 2019; Wang et al., 2015). However, to our knowledge, a simultaneous measurement of eye and attempted head movements elicited by SC microstimulation had not been performed. To perform this comparison, we pursued an optogenetic approach. We stereotaxically injected adeno-associated virus (AAV) encoding the light-gated ion channel ChR2 under the control of a pan-neuronal promoter and implanted a fiber optic in right SC (Figure 2.1B). Several weeks later, we head-fixed mice and used infrared cameras to track both pupils and a strain gauge (also known as a load cell) to measure attempted head rotations (Figure 2.1A). Consonant with previous studies, SC optogenetic stimulation elicited contraversive eye and attempted head movements (Figure 2.1C, D). Strikingly, optogenetically evoked saccades and attempted head movements were roughly coincident, similar to what has been described for SC-dependent sensory-guided gaze shifts in other species and unlike the temporal relationship previously documented for mouse spontaneous and visually evoked gaze shifts (Figure 2.1C, E).

In light of this observation, we hypothesized that mice possess an innate ability to make sensory-evoked gaze shifts that incorporate directionally biased saccades coupled to head movements. To test this hypothesis, we head-fixed naïve, wild-type

adult animals and tracked eye and attempted head movements. Previous studies in head-fixed mice observed occasional undirected saccades in response to changes in the visual environment (Samonds et al., 2018) and visually guided saccades only after weeks of training and at long (~1 s) latencies (Itokazu et al., 2018). We therefore tested a panel of stimuli of different modalities to determine whether they could evoke saccades. We began by presenting the following stimuli from a constant azimuthal location: 1) a multisensory airpuff that provides tactile input to the ears and generates a loud, broadband sound; 2) an auditory stimulus consisting of the same airpuff moved away from the animal so as not to provide tactile input; 3) a tactile stimulus consisting of a bar that nearly silently taps the ear; and 4) a visual stimulus consisting of a bright LED. Stimuli were presented on either side of the animal every 7-12 s in a pseudorandom sequence (Figure 2.2A). The probability of horizontal eye movements increased sharply and significantly above the low baseline level ($1.3 \pm 0.2\%$, mean \pm s.d.) in the 100 ms period following delivery of multisensory airpuffs (ear airpuff: $29.0 \pm 7.5\%$, $p < 0.001$ paired Student's t-test; whisker airpuff: $12.5 \pm 2.3\%$, $p < 0.001$), auditory airpuffs ($3.5 \pm 1.2\%$, $p < 0.05$), and tactile stimuli ($4.5 \pm 0.5\%$, $p < 0.001$) and remained slightly elevated for at least 500 ms (Figure 2.2B-F, G-K; Figure S2.1; Figure S2.2). In contrast, the probability of saccade generation was not changed by visual stimuli (Figure 2.2F, K; $1.3 \pm 0.2\%$, $p = 0.61$). We consider these stimulus-evoked eye movements to be saccades because they reached velocities of several hundred degrees per second (Figure S2.1), displayed a main sequence, *i.e.*, peak velocity scaled linearly with amplitude (Figure S2.1) and were bilaterally conjugate (Figure S2.1) (Bahill et al., 1975). As in previous studies, saccade size for temporal-to-nasal

movements was slightly larger than for nasal-to-temporal movements (Meyer et al., 2018), but this asymmetry was eliminated by averaging the positions of both pupils (before averaging: temporal saccade amplitude = $10.9 \pm 0.8^\circ$ (mean \pm s.d.), nasal saccade amplitude = $8.4 \pm 1.1^\circ$, $p = 0.0009$; after averaging, leftward amplitude = $10.2 \pm 1.0^\circ$, rightward amplitude = $9.3 \pm 0.4^\circ$, $p = 0.0986$).

We next examined attempted head movements. The baseline frequency of attempted head movements was much higher than that of eye movements ($27.8 \pm 4.8\%$, mean \pm s.d.). Mirroring results for saccades, auditory, tactile, and audiotactile stimuli evoked attempted head movements but visual stimuli did not (Figure 2.2L-P; auditory: $53.2 \pm 21.9\%$, $p = 0.045$; tactile: $67.1 \pm 10\%$, $p < 0.01$; ear airpuff: $86.6 \pm 8.7\%$, $p < 10^{-5}$; whisker airpuff: $79.2 \pm 9.5\%$, $p < 0.001$; visual: $26.9 \pm 2.0\%$, $p = 0.0505$, paired Student's t-test). These data demonstrate that both auditory and tactile stimuli are sufficient to evoke gaze shifts in head-fixed mice, and that mice make sensory-evoked saccades in the absence of vestibular and optokinetic inputs.

Tactile stimuli evoke directionally biased eye and attempted head movements

To determine whether sensory-evoked saccades are directionally biased, we asked whether saccade endpoints are dependent on stimulus location. We began by examining the endpoints of saccades evoked by left and right ear airpuffs (Figure 2.3A; Figure S2.3). We found that left ear airpuffs evoked saccades with endpoints far left of center (with center defined as the mean eye position), whereas right ear airpuffs evoked saccades with endpoints far right of center (left: $-5.4 \pm 4.5^\circ$, right: $5.4 \pm 3.4^\circ$, mean \pm s.d., $p < 10^{-10}$ Welch's t-test, $n = 2155$ trials). To understand how this endpoint segregation arises, we examined the trajectories of individual saccades (Figure 2.3E).

We found that left ear airpuffs elicited nearly exclusively leftward saccades ($94.2 \pm 3.1\%$, mean \pm s.d., $n = 5$ mice), whereas right ear airpuffs elicited nearly exclusively rightward saccades ($96.0 \pm 2.1\%$)—often from the same eye positions. By definition, from any eye position, one of these directions must lead away from center and is thus centrifugal rather than centripetal. In addition, puff-evoked saccades that began towards the center often overshoot to reach endpoints at eccentricities of 5 to 10 degrees. To further test whether saccade endpoints are specified by stimulus location, we repositioned the airpuff nozzles to stimulate the whiskers and repeated the experiments. We reasoned that saccade endpoints should become less eccentric as stimulus eccentricity decreases. Indeed, airpuffs applied to the whiskers evoked saccades with endpoints central to those evoked by ear airpuff stimulation, such that the ordering of saccade endpoints mirrored that of stimulus locations (Mean endpoints: left ear, $-5.4 \pm 4.5^\circ$; left whiskers, $-0.4 \pm 3.8^\circ$; right whiskers, $0.8 \pm 3.9^\circ$; right ear, $5.4 \pm 3.4^\circ$; mean \pm s.d., $p < 0.05$ for all pairwise comparisons, paired two-tailed Student's t-test) (Figure 2.3A,B; Figure S2.3; Figure S2.4). In this cohort, the separation between whisker-evoked saccade endpoints, although significant, was small, but in other cohorts we observed larger separation (as well as higher auditory-evoked saccade probabilities) (Figure S2.5). Taken together, these data suggest that airpuff-evoked saccades are biased towards particular eye positions that are specified by stimulus location.

We next examined the endpoints of saccades evoked by tactile and auditory stimuli. Similar to the multisensory airpuff stimuli, tactile stimuli delivered to the left and right ears evoked saccades whose endpoints were significantly different ($-3.9 \pm 5.3^\circ$ (left) vs. $1.5 \pm 5.0^\circ$ (right); mean \pm s.d., $p < 10^{-10}$, Welch's t-test, $n = 452$ trials) and

whose directions were largely opposite from nearly all eye positions (Figure 2.3C, G; Figure S2.3) (left stimuli evoked $77.5 \pm 23.7\%$ leftward saccades, right stimuli evoked $78.3 \pm 11.6\%$ rightward saccades, $n = 5$ mice). This result suggests that tactile stimuli are sufficient to induce gaze shifts that involve directionally biased saccades. We next examined the endpoints and trajectories of saccades evoked by left and right auditory stimuli (Figure 2.3D, H; Figure S2.3). Strikingly, the endpoint locations did not differ significantly for saccades elicited by left and right auditory stimuli and were located centrally ($0.1 \pm 5.1^\circ$ (left) vs. $-0.1 \pm 5.1^\circ$ (right); mean \pm s.d., $p = 0.72$, Welch's t-test, $n = 298$ trials). Because we had fewer trials with sound-evoked gaze shifts overall, to confirm that this lack of significant endpoint separation was not a result of lower statistical power, we repeated our analyses on equal numbers of sound- and touch-evoked saccades sampled at random, once again observing that left and right ear airpuff-, whisker airpuff-, and ear tactile-evoked saccade endpoints were significantly different (ear airpuff, $p < 10^{-10}$; whisker airpuff, $p = 0.0039$; ear tactile, $p < 10^{-10}$; auditory airpuff, $p = 0.50$; Welch's t-test). The central endpoints of sound-evoked saccades arose because, in contrast to touch-evoked saccades, saccades evoked by both right and left stimuli traveled in the same, centripetal direction from all initial eye positions: rightward from eye positions to the left of center, and leftward from eye positions to the right of center (fraction centripetal: left airpuff for initial eye positions left of center, 0.89 ± 0.08 ; left airpuff for initial eye positions right of center, 0.90 ± 0.09 ; right airpuff for initial eye positions left of center, 0.87 ± 0.07 ; right airpuff with initial eye positions right of center, 0.76 ± 0.12). We compared the mean sound-evoked saccade endpoint location to the mean overall eye position and found no significant difference, suggesting that auditory

saccades function to center the eye ($p = 0.93$, one-sample Student's t-test) (Land and Nilsson, 2012; Meyer et al., 2018, 2020; Michaiel et al., 2020; Paré and Munoz, 2001; Tatler, 2007). These responses are unlikely to be due to an auditory startle response, which is elicited by stimuli louder than 80 dB, because the airpuffs were < 65 dB (Gómez-Nieto et al., 2020). Thus, both the auditory and tactile components of the airpuff stimuli are sufficient to evoke saccades but only tactile stimulation evokes directionally biased saccades whose endpoints are specified by the site of stimulation.

We next analyzed the relationship between stimuli and attempted head movements. The amplitude distributions for attempted head movements to left and right ear airpuff stimuli were well separated (left: -1.56 ± 1.25 Z, right: 1.29 ± 1.16 Z, mean \pm s.d., $p < 10^{-10}$ Welch's t-test, $n = 2155$ trials), mirroring the separation of the endpoints of saccades elicited by left and right stimuli (Figure 2.3I). Similarly, whisker and tactile stimuli elicited attempted head movements whose amplitude distributions were separated (left whiskers: -0.22 ± 1.58 Z, right whiskers: 0.20 ± 1.42 Z, $p < 10^{-4}$, $n = 1046$; left tactile: -1.45 ± 1.84 Z, right tactile: 0.55 ± 1.75 Z, $p < 10^{-10}$, $n = 319$; mean \pm s.d., Welch's t-test) but less so than those of ear airpuffs (Figure 2.3J, K). Left and right auditory airpuffs elicited attempted head movements whose distributions overlapped (left: -0.25 ± 2.04 Z, right: 0.07 ± 1.94 Z, mean \pm s.d., $p = 0.16$, Welch's t-test, $n = 298$ trials), similar to what was observed for saccades (Figure 2.3L). Thus, it appeared that the patterns of evoked eye and attempted head movements were similar for a given stimulus but different across stimuli, with tactile but not auditory stimuli able to evoke directionally biased movements.

Stimulus-evoked gaze shifts lack pre-saccadic head movements

Having observed that mice are able to make directionally biased gaze shifts, similar to what we had observed in SC optogenetic stimulation, we next compared the relationships between attempted head rotations and saccades during spontaneous and stimulus-evoked gaze shifts. We first analyzed the relative timing of eye and attempted head movements. Whereas our SC optogenetic stimulation evoked roughly coincident saccades and attempted head movements, previous studies found that on average, spontaneous and visually evoked saccades in freely moving mice are preceded by head rotations, and that spontaneous saccades in head-fixed mice are similarly preceded by slow attempted head rotations (Figure 2.1) (Meyer et al., 2018, 2020; Michael et al., 2020; Payne and Raymond, 2017). Consistent with these observations, we found that most spontaneous saccades were preceded by attempted head rotations in the same direction as the ensuing saccade (Figure 2.4B, D, E). Interestingly, attempted head rotations during spontaneous saccades appeared biphasic, with a slow phase starting 100-200 ms before saccade onset followed by a fast phase beginning roughly simultaneously with saccade onset (Figure 2.4B, D, E). This biphasic response closely resembles the eye-head coupling pattern reported in freely moving mice (Meyer et al., 2020).

We hypothesized that touch-evoked gaze shifts are mediated by SC and therefore that the relative timing of eye and attempted head movements would more closely resemble those observed in other species and in our SC optogenetic stimulation. Consistent with our prediction, ear airpuff-evoked saccades were typically not preceded by slow attempted head rotations but were accompanied by roughly

coincident fast attempted head rotations (Figure 2.4B, D, F). On average, these fast attempted head rotations had similar peak velocities and latencies relative to saccade onset to those observed from SC optogenetic stimulation as well as those made during the fast phase of head movements during spontaneous gaze shifts (Figure 2.4B, D). This pattern was mirrored in the average eye and attempted head movement traces for whisker airpuff-, auditory airpuff-, and ear tactile-evoked saccades (Figure S2.6A-D).

To better understand how these patterns arose, we examined eye and attempted head movement timing at the single-trial level. For spontaneous gaze shifts, attempted head movement onset fell along a continuum starting well before saccade onset, with attempted head displacement roughly 60% predictive of the direction of the ensuing saccade starting as early as 200 ms before saccade onset and approximately 80% predictive by 100 ms before saccade onset (Figure 2.4E,G). In contrast, for stimulus-evoked gaze shifts, the vast majority of attempted head movements began roughly coincidentally with saccade onset, and attempted head displacement was not predictive of head position before saccade onset (Figure 2.4F,G). Attempted head velocity showed similar trends (Figure 2.4I-K). Thus, these data suggest that spontaneous gaze shifts are typically preceded by attempted head movements in the direction of the ensuing saccade whereas stimulus-evoked gaze shifts are not.

We next examined the amplitudes of head and eye movements during spontaneous and stimulus-evoked gaze shifts. During spontaneous gaze shifts, both the slow and fast phases of attempted head rotations were in the same direction as the ensuing saccades and scaled with saccade amplitude (Figure 2.4A, B, E, H, I, K, L). These data are consistent with eye-head coupling patterns previously observed in both

head-fixed and freely moving conditions (Meyer et al., 2020). Similarly, stimulus-evoked gaze shifts involved attempted head rotations that were made in the same direction as saccades and scaled with saccade amplitude (Figure 2.4A, B, F, H, J, K, L).

Interestingly, stimulus-evoked saccades of a given amplitude were coupled to an average of 24% smaller attempted head movements than were spontaneous saccades (linear regression slopes 0.162 vs. 0.214, $p < 10^{-5}$, permutation test) (Figure 2.4H). This difference was due to the slow pre-saccadic attempted head movements observed during spontaneous gaze shifts, as the fast phase of both spontaneous and evoked gaze shifts was nearly identical (Figure 2.4L). To confirm that the differences in coupling we observed were not an artifact of differences in saccade size and starting position between saccade types, we performed an additional analysis using subsets of gaze shifts matched for saccade amplitude and initial eye position, observing the same effects (Figure S2.7; linear regression slopes 0.162 vs. 0.221, $p < 10^{-5}$, permutation test). To determine whether these differences could be attributed to experience, e.g., if animals learn that attempted head movements in response to sensory stimuli are futile, we compared evoked and spontaneous gaze shifts across 5 sessions and within sessions (Figure S2.8). Interestingly, the gain of head-eye coupling did appear significantly lower for evoked but not spontaneous gaze shifts by the fifth session, but at every time point analyzed, evoked gaze shifts involved smaller head movements than did spontaneous gaze shifts (Figure S2.8). These data indicate that mice may subtly and slowly change their strategies with experience but differences between spontaneous and evoked gaze shifts do not require learning.

Directionally biased saccades reflect different stimulus-dependent relationships between initial eye position and saccade direction and amplitude

We next sought to understand how different stimuli evoke saccades with distinct endpoints. Given the prevailing view that head movements drive saccades during mouse gaze shifts, one possibility was that directionally biased saccade endpoints are the result of larger or more directionally biased attempted head movements. Indeed, the distributions of attempted head displacements seemed similar to those of saccade endpoints, suggesting that this was possible, although there was not a clear relationship between average attempted head movement amplitude and saccade endpoint eccentricity (Figure 2.3A-D, I-L; Figure S2.6A-D). Therefore, to directly test whether different distributions of attempted head movement direction and amplitude across stimuli could explain the distinct saccade endpoints (e.g., with stimuli that evoke larger head movements causing saccades that overshoot to more directionally biased endpoints) we compared trials across stimuli with matched attempted head movement direction and amplitude (Figure 2.3A, B, I, J; Figure S2.9). If differences in attempted head movements underlie directionally biased saccade endpoints, then controlling for attempted head movement amplitude in this manner should cause whisker and ear airpuff-evoked saccade endpoints to be similar. Strikingly, however, endpoints for attempted head movement-matched whisker and ear airpuff trials remained well-separated, indicating that the more directionally biased endpoints of ear airpuff-evoked saccades are not simply due to larger or more directionally biased attempted head movements (Figure S2.9).

Because saccade endpoints are a function of both saccade amplitude and initial eye position, we next examined whether stimulus-dependent differences in the relationship between initial eye position and saccade direction and amplitude could contribute to resulting endpoint differences. Indeed, for all stimuli there was an inverse relationship between initial eye position and saccade amplitude but the slopes and intercepts of the lines of best fit describing these relationships differed depending on stimulus modality and location (Figure 2.5A-D; Figure S2.11). For example, stimuli with central saccade endpoints had lines of best fit passing through the origin, whereas stimuli with more leftward or rightward endpoints had lines of best fit that were shifted downward or upward, respectively. In other words, saccades of a given amplitude were usually elicited from distinct initial eye positions by different stimuli: for example, 5° leftward saccades were evoked by left ear airpuffs from central initial eye positions but by left auditory airpuffs from initial eye positions roughly 5° right of center (Figure 2.5A, D; Figure S2.11). In this way, otherwise identical 5° saccades have central endpoints in response to an auditory airpuff and leftward endpoints in response to a left ear airpuff. Thus, endpoint differences between stimuli arise at least in part from distinct stimulus-dependent relationships between initial eye position and saccade direction and amplitude.

Having observed that initial eye position and stimulus location jointly shape the direction and amplitude of stimulus-evoked saccades, we next examined whether they had any relationship with saccade probability. Indeed, initial eye position strongly influenced saccade probability, and the relationship between initial eye position and saccade probability differed across stimuli, with the lowest probability coinciding with the

mean endpoint of saccades evoked by that stimulus (Figure 2.5I-L; Figure S2.12). For all stimuli, leftward eye movements were more likely from initial eye positions to the right of the mean saccade endpoint for that stimulus, whereas rightward eye movements were more likely from initial eye positions to the left of the mean saccade endpoint for that stimulus. In contrast, saccade probability did not differ between trials with high (dilated pupils) or low (constricted pupils) arousal (Figure S2.13) (Reimer et al., 2014) and declined only slightly over successive sessions or within sessions.

Finally, because the preceding analyses found that saccade direction and amplitude depend on initial eye position and stimulus location (Figure 2.5A-D, I-L), and because head and eye movement direction and amplitude are highly correlated, we asked whether initial eye position and stimulus location shape the direction and amplitude of evoked head movements. We first analyzed whisker airpuff-evoked gaze shifts because these involved a mixture of saccade directions. Strikingly, attempted head movement direction and amplitude were dependent on initial eye position (Figure 2.5F; Figure S2.11). We then analyzed auditory airpuff-evoked gaze shifts, which also involved a mixture of saccade directions. As for whisker airpuffs, both attempted head movement direction and amplitude were dependent on initial eye position (Figure 2.5D; Figure S2.11). We next examined ear tactile stimuli, which elicited mostly contraversive movements but also some ipsiversive movements. Indeed, as for both whisker and auditory airpuffs, attempted head movement direction and amplitude depended on eye position, but the slope of this relationship was shallower (Figure 2.5G; Figure S2.11). We then examined ear airpuffs. These stimuli elicited nearly exclusively contraversive movements, such that no effect of eye position on direction could be observed, and

effects on amplitude were subtle, with shallower slopes, and significant for stimuli only on one side (Figure 2.5E, Figure S2.11). However, eye position strongly influenced the probability of attempted head movements evoked by all stimuli, including ear airpuffs (Figure 2.5M-P, Figure S2.11). As a control, we examined the relationship between the initial position of the head, as measured by the strain gauge, and saccade and attempted head movement direction and amplitude. For all stimuli, initial eye position was a much stronger predictor of saccade direction and amplitude than was initial position of the head (Figure S2.14). Likewise, for each of the stimuli for which attempted head movement direction and amplitude were well predicted by initial eye position—whisker airpuffs, ear tactile stimuli, and auditory airpuffs—initial head position was a weak predictor of attempted head movements (Figure S2.14). Taken together, these data indicate that starting eye position and stimulus location jointly shape attempted head and eye movement probability, direction, and amplitude.

The superior colliculus mediates airpuff-evoked gaze shifts

We next sought to identify the neural circuitry underlying airpuff-evoked gaze shifts. As discussed previously, in other species, stimulus-evoked gaze shifts involving directed head and eye movements are driven by SC (Freedman, 2008; Freedman et al., 1996; Guitton, 1992; Guitton et al., 1980; Paré et al., 1994). In contrast, it is widely believed that the recentering saccades observed in mice are driven by brainstem circuitry in response to head rotation (Curthoys, 2002; Hepp et al., 1993; Kitama et al., 1995; Meyer et al., 2020; Michael et al., 2020; Payne and Raymond, 2017). To determine whether SC is required to generate touch-evoked gaze shifts in mice, we pursued an optogenetic strategy to perturb SC activity in the period surrounding airpuff

onset. For inhibition experiments, we stereotaxically injected adeno-associated virus (AAV) encoding the light-gated chloride pump eNpHR3.0 under the control of a pan-neuronal promoter and implanted a fiber optic in right SC (Gradinaru et al., 2010). Consistent with data in foveate species (Hikosaka and Wurtz, 1985; Robinson, 1972; Schiller and Stryker, 1972), optically reducing right SC activity shifted airpuff-evoked saccade endpoints to the right (i.e., ipsilaterally) for both left ($-3.7 \pm 4.3^\circ$ (control) vs. $-2.3 \pm 4.7^\circ$ (LED on), $p < 0.001$, Welch's t-test) and right ear airpuffs ($4.5 \pm 4.1^\circ$ (control) vs. $5.4 \pm 4.7^\circ$ (LED on), $p = 0.011$, Welch's t-test) (Figure 2.6A-C). To control for potential mismatches in starting eye position between LED-off and LED-on trials, we performed additional analyses using matched trials and found that the endpoint and amplitude differences persisted (Figure S2.15). For stimulation experiments, we again stereotaxically injected AAV encoding the light-gated ion channel ChR2 under the control of a pan-neuronal promoter and implanted a fiber optic in right SC (Gradinaru et al., 2010). Because strong SC stimulation can evoke saccades, we used weak stimulation (50-120 μ W) in order to bias SC activity. This manipulation caused the reciprocal effect of right SC inhibition, biasing endpoints leftwards (i.e., contraversively) for both left ($-5.8 \pm 4.6^\circ$ (control) vs. $-8.0 \pm 6.1^\circ$ (LED on), $p = 0.0016$, Welch's t-test) and right ($5.6 \pm 3.5^\circ$ (control) vs. $1.9 \pm 6.1^\circ$ (LED on), $p < 10^{-5}$, Welch's t-test) airpuffs (Figure 2.6E-G). Once again, controlling for differences in starting eye position between conditions yielded similar results (Figure S2.15).

To understand how SC manipulations affect attempted head movements and head-eye coupling, we examined the distribution of head movements as a function of saccade amplitude. As expected, given the role of SC in generating both head and eye

movements, attempted head movements were shifted to the right (*i.e.*, ipsiversively) by SC inhibition (Figure 2.6D) and to the left (*i.e.*, contraversively) by SC excitation (Figure 2.6H). To examine the effects of SC manipulations on head-eye coupling, we identified trials with identical saccade trajectories in LED-on and LED-off conditions and examined the corresponding head movement amplitudes. Interestingly, SC manipulations had no effect on the relationship between saccade and head movement amplitudes, suggesting that SC manipulations do not change head-eye coupling during gaze shifts. Taken together, these bidirectional manipulations indicate that SC serves a conserved necessary and sufficient role in generating ear airpuff-evoked gaze shifts.

2.4 DISCUSSION

Here we investigated whether mouse gaze shifts are more flexible than had previously been appreciated. In the prevailing view, mouse gaze shifts are led by head rotations that trigger compensatory eye movements, including saccades that function to reset the eyes (Land, 2019; Land and Nilsson, 2012; Liversedge et al., 2011; Meyer et al., 2020; Michael et al., 2020; Payne and Raymond, 2017). These “recentering” saccades are attributed to head movement-related vestibular and optokinetic cues (Curthoys, 2002; Meyer et al., 2020; Michael et al., 2020; Payne and Raymond, 2017). Working in a head-fixed context to eliminate vestibular and optokinetic cues and to present stimuli of different modalities at precise craniotopic locations, we found that mouse gaze shifts are more flexible than previously thought. As discussed below, we identified unexpected flexibility in the endpoints of saccades, saccade timing and amplitude relative to attempted head movements, the eye positions from which gaze shifts are made, and the brain regions that drive them.

Touch-evoked saccades are directionally biased

The first indication that mouse gaze shifts are more flexible than previously appreciated was that an analysis of endpoints revealed that touch-evoked saccades are directionally biased rather than recentering. This conclusion is based on three lines of evidence. First, endpoints of saccades evoked by left and right ear airpuffs are near the left and right edges, respectively, of the range of eye positions observed and overlap minimally, despite trial-to-trial variability. In contrast, endpoints for saccades evoked by left and right auditory stimuli are indistinguishable and centrally located. Second, left and right ear airpuffs evoke saccades traveling in opposite directions from most eye

positions; by definition, one of these directions must lead away from center and is thus *centrifugal* rather than *centripetal*. In contrast, saccades evoked by both left and right auditory stimuli travel centripetally from all initial eye positions. Third, from many eye positions, touch-evoked saccades that begin towards the center pass through to reach endpoints at eccentricities between 5 to 10 degrees and cannot accurately be termed centripetal. For these reasons, we conclude that touch-evoked saccades are directionally biased and do not serve to recenter the eyes.

Our findings contrast with and complement previous studies contending that rodents, like other afoveates, use saccades to reset their eyes to more central locations (Meyer et al., 2018, 2020; Michael et al., 2020; Wallace et al., 2013). One recent analysis suggested that gaze shifts made during visually guided prey capture involve resetting centripetal saccades that “catch up” with the head (Michael et al., 2020). Another found that saccades away from the nose recenter the eye, whereas saccades toward the nose move the eye slightly beyond center (Meyer et al., 2020). Although we observed this as well, it does not contribute to our results because we averaged the positions of the left and right eyes, eliminating this asymmetry. Earlier studies in head-fixed mice observed occasional, undirected saccades in response to changes in the visual environment (Samonds et al., 2018) and found that mice could be trained to produce visually guided saccades only after weeks of training and at extremely long (~1 s) latencies (Itokazu et al., 2018). To our knowledge, ours is the first study demonstrating innate gaze shifts involving directionally biased saccades in mice (or any species lacking a fovea). An important caveat is that the present studies were

conducted in head-fixed animals, and mice may behave differently in a freely moving context due to head movement-related feedback mechanisms.

Touch-evoked saccades do not follow head movements

The prevailing view holds that head movements initiate and determine the amplitude of mouse gaze shifts, with eye movements compensatory by-products. In support of this model, one study found that spontaneous saccades in head-fixed mice are preceded by attempted head rotations. A careful comparison with gaze shifts occurring during visually guided object tracking and social interactions in freely moving mice led the authors to suggest that head-eye coupling is not disrupted during head-fixation, and that gaze shifts in both contexts are head-initiated (Meyer et al., 2020). Another study tracked the eyes and head during visually guided cricket hunting and found that gaze shifts are driven by the head, with the eyes following to stabilize and recenter gaze (Michaël et al., 2020). Together, these findings have bolstered the prevailing view that afoveates such as mice generate gaze shifts driven by head movements, with eye movements compensatory by-products (Land, 2019; Land and Nilsson, 2012; Liversedge et al., 2011). Consistent with published findings in both freely moving and head-fixed mice, we found that spontaneous saccades are preceded by slow attempted head movements in the direction of the ensuing saccade, typically beginning 100-200 ms before saccade onset (Meyer et al., 2020; Michaël et al., 2020). In contrast, we found that touch-evoked gaze shifts are not preceded by head movements, suggesting that mouse saccades are not always made in response to head movements. Additional support for this idea came from an analysis of head and eye movements as a function of eye position. If gaze shifts were determined solely by the

location of the stimulus relative to the head and saccades were a compensatory by-product of this calculation, eye position should have no effect on head movements. However, we found that the amplitudes, directions, and/or probabilities of stimulus-evoked saccades and attempted head movements vary with initial eye position. The influence of eye position on evoked eye *and* attempted head movements further suggests that saccades are not simply compensatory by-products of head movements. Instead, we contend, touch-evoked head movements and saccades are likely to be specified simultaneously as parts of a coordinated movement whose component movements take into account both stimulus location and initial eye position. Nevertheless, it is possible that the observed relationship between evoked saccades and attempted head movements is due to the lack of head movement-related feedback in head-fixed mice.

The relative timing of head and eye movements during touch-evoked gaze shifts in head-fixed mice resembles that observed during gaze shifts in cats and primates. For example, head-fixed cats and primates generate gaze shifts using directed saccades and then maintain their eyes in the new orbital position, similar to what we have observed in mice (Freedman, 2008; Guitton et al., 1980). In addition, saccades in head-fixed cats and primates are often accompanied by attempted head rotations, similar to those we observe during touch-evoked gaze shifts in head-fixed mice (Bizzi et al., 1971; Guitton et al., 1984; Paré et al., 1994). In primates and cats able to move their heads, gaze shifts are usually led by directed saccades (with some exceptions), likely because the eyes have lower rotational inertia and can move faster (Pelisson and Guillaume, 2009; Ruhland et al., 2013). These saccades tend to be followed by a head movement

in the same direction that creates vestibular signals that drive slow, centripetal counterrotation of the eyes to maintain fixation (Bizzi et al., 1972; Freedman, 2008; Freedman and Sparks, 1997; Guitton et al., 1984). In this way, the animal can rapidly shift its gaze with a directed saccade yet subsequently reset the eyes to a more central position. It is tempting to speculate that a similar coordinated sequence of head and eye movements occurs during touch-evoked gaze shifts in freely moving mice, enabling mice to rapidly shift gaze with their eyes while eventually resetting the eyes in a more central orbital position.

Head-eye amplitude coupling differs during spontaneous and evoked saccades

An additional feature that distinguishes spontaneous and touch-evoked gaze shifts is the relative contributions of head and eye movements. We found that spontaneous saccades of a given amplitude are coupled to larger head movements than are touch-evoked saccades. This difference arises largely from the absence of a pre-saccadic slow attempted head movement during touch-evoked gaze shifts, as the fast phases are similar. This differential pairing of head and eye movements is reminiscent of reports in primates and cats that the relative contributions of head and eye movements vary for gaze shifts evoked by different sensory modalities (Goldring et al., 1996; Populin, 2006; Populin and Rajala, 2011; Populin et al., 2004a; Ruhland et al., 2013; Tollin et al., 2005). However, in those species, vision typically elicits gaze shifts dominated by saccades while hearing typically evokes gaze shifts entailing larger contributions from head movements. In contrast, we observed that sound- and touch-evoked gaze shifts involve larger contributions from saccades than do spontaneous gaze shifts, whereas visual stimuli did not evoke gaze shifts at all. This indicates that

although there is general conservation of the involvement of SC in sensory-driven gaze shifts, modality-specific features are not conserved, which may reflect differences in sensory processing across species. We also observed limited variability across mice in the relative contributions of head and eye movements to gaze shifts, which contrasts with the observation that different human subjects are head “movers” and “non-movers” during gaze shifts (Figure S2.10) Thus, our results reveal that head-fixed mice are capable of using multiple strategies to shift their gaze but with key differences from other species.

Directionally biased saccade endpoints reflect different stimulus-dependent relationships between initial eye position and saccade direction and amplitude

Given the prevailing view that head movements drive saccades during mouse gaze shifts, we predicted that directionally biased saccades were the result of different head movements, e.g., stimuli that elicit saccades with more eccentric endpoints cause proportionally larger head attempted head movements. Indeed, distributions of attempted head displacements and saccade endpoints appeared similar for the stimuli tested. However, an analysis of trials matched for head movement direction and amplitude across stimuli yielded well-separated endpoints, suggesting that more eccentric saccade endpoints and the associated distributions of attempted head displacements are not simply due to differences in the directions and amplitudes of evoked head movements. Instead, we found that saccade endpoint differences across stimuli were associated with distinct stimulus-dependent relationships between initial eye position and saccade amplitude and direction. For example, 5° leftward saccades were evoked by left ear airpuffs from central initial eye positions but by left auditory

airpuffs from initial eye positions roughly 5° right of center. In this way, saccades with identical amplitudes, coupled to identical attempted head movements, yielded central endpoints in response to an auditory airpuff and eccentric endpoints in response to a left ear airpuff. In the future, it will be essential to determine the neural mechanisms that instantiate these strategies and to examine these strategies in freely moving mice.

The role of superior colliculus in sensory-evoked mouse gaze shifts

In other species, SC drives sensory-evoked gaze shifts, and microstimulation and optogenetic stimulation of mouse SC has been shown to elicit gaze shifts (Masullo et al., 2019; Wang et al., 2015). However, to our knowledge, no study had identified a causal involvement of SC in mouse gaze shifts. We found that optogenetic stimulation of SC elicits directionally biased saccades that coincide with attempted head movements and resembled those elicited by touch. We therefore performed bidirectional optogenetic manipulations that revealed that touch-evoked gaze shifts depend on SC, identifying a conserved, necessary and sufficient role for SC in directed gaze shifts. In addition, we found that SC manipulations did not alter head-eye amplitude coupling. This observation suggests that SC specifies the overall gaze shift amplitude rather than the individual eye or head movement components, consistent with observations in other species (Freedman et al., 1996; Paré et al., 1994).

Ethological significance

Prior to the present study, it was believed that species with high-acuity retinal specializations acquired the ability to make directed saccades to scrutinize salient environmental stimuli, because animals lacking such retinal specializations were thought incapable of gaze shifts led by directed saccades (Land, 2019; Land and

Nilsson, 2012; Liversedge et al., 2011; Walls, 1962). Our discovery that sensory-guided directionally biased saccades are present in head-fixed mice—albeit without the precise targeting of stimulus location seen in foveate species—raises the question of what fovea-independent functions these movements ordinarily serve. Although mice have lateral eyes and a large field of view, saccades that shift gaze in the direction of a stimulus, as seems to occur with both ear and whisker tactile stimuli, may facilitate keeping salient stimuli within the field of view. As natural stimuli are often multimodal, directing non-visual stimuli towards the center of view maximizes the likelihood of detecting the visual component of the stimulus. Alternatively, despite mouse retinae lacking discrete, anatomically defined specializations such as foveae or areas centralis, there are subtler nonuniformities in the distribution and density of photoreceptors and retinal ganglion cell subtypes, and magnification factor, receptive field sizes, and response tuning vary across the visual field in higher visual centers; it may be desirable to center a salient tactile stimulus on a particular retinal region (Ahmadlou and Heimel, 2015; Baden et al., 2013; van Beest et al., 2021; Bleckert et al., 2014; Drager and Hubel, 1976; Feinberg and Meister, 2015; Li et al., 2020; de Malmazet et al., 2018). Although touch-evoked saccades alone may be too small to center the stimulus location on any particular region of the retina, they may do so in concert with directed head movements. Experiments in freely moving mice will be essential to understanding the behavioral functions of these saccades.

Why tactile stimuli evoked directionally biased saccades in our preparation whereas auditory and visual stimuli do not is unclear. One possibility is the aforementioned speed of saccades relative to head movements may be especially

beneficial because tactile stimuli typically derive from proximal objects and as a result may demand rapid responses. Alternatively, the high spatial acuity of the tactile system may enable more precise localization (Allen and Ison, 2010; Diamond et al., 2008). Auditory stimuli, in contrast, may alert animals to the presence of a salient stimulus in their environments whose location is less precisely ascertained, and as a result drive gaze shifts whose goal is to reset the eyes to a central position that maximizes their chances of sensing and responding appropriately. Finally, our set of stimuli was not exhaustive, and it is possible that as yet unidentified visual or auditory stimuli could elicit gaze shifts with directionally biased saccades.

Future Directions

In this study we used a head-fixed preparation to eliminate the confound of head movement-related sensory cues and to present stimuli from defined locations. However, in the future, it will be critical to compare touch-evoked gaze shifts in head-fixed and freely moving animals. For example, as noted previously, whereas head-fixed primates and cats generate gaze shifts using directed saccades and then maintain their eyes in the new orbital position, similar to what we have observed, in freely moving primates and cats, gaze shifts are led by directed saccades but typically followed by head movements during which the eyes counterrotate centripetally in order to maintain gaze in the new direction. It will be interesting to know whether similar differences distinguish saccade-led touch-evoked gaze shifts in head-fixed and freely moving mice. By expanding on methods similar to those recently described by Meyer *et al.* and Michael *et al.*, it may be possible to investigate these and other questions (Meyer et al., 2018, 2020; Michael et al., 2020).

Furthermore, a practical implication of our identification of mouse SC-dependent gaze shifts is that this behavioral paradigm could be applied to the study of several outstanding questions. First, there are many unresolved problems regarding the circuitry and ensemble dynamics underlying target selection (Basso and May, 2017) and saccade generation (Gandhi and Katnani, 2011), and the mouse provides a genetically tractable platform with which to investigate these and other topics. Second, gaze shifts are aberrant in a host of conditions, such as Parkinson's and autism spectrum disorder (Liversedge et al., 2011). This paradigm could be a powerful tool for the study of mouse models of a variety of neuropsychiatric conditions. Third, directing saccades towards particular orbital positions during these gaze shifts requires an ability to account for the initial positions of the eyes relative to the target, a phenomenon also known as remapping from sensory to motor reference frames. Neural correlates of this process have been observed in primates (Groh and Sparks, 1996; Jay and Sparks, 1984) and cats (Populin et al., 2004b), but the underlying circuitry and computations remain obscure. This behavior may facilitate future studies of this problem. Fourth, the different types of gaze shifts that rely on distinct head-eye coupling we have identified may be useful for understanding mechanisms that control movement coordination. Thus, touch-evoked saccade behavior is likely to be a powerful tool for myriad lines of investigation.

Conclusions

We have found that mouse gaze shifts are unexpectedly flexible, with mice able to make both spontaneous gaze shifts led by the head and stimulus-evoked gaze shifts involving directionally biased saccades not preceded by slow head movements. Prior studies in species whose retinæ lack high-acuity specializations had never observed

gaze shifts with these properties, but our study used a broader range of stimuli than previously tested and a head-fixed preparation that allowed spatially precise delivery. Detailed perturbation experiments determined that the circuit mechanisms of sensory-evoked gaze shifts are conserved from mice to primates, suggesting that this behavior may have arisen in a common, afoveate ancestral species long ago. More broadly, our findings suggest that analyzing eye movements of other afoveate species thought not to make directed saccades—such as rabbits, toads, and goldfish—in response to a diverse range of multimodal stimuli may uncover similar flexibility.

2.5 METHODS

Mice

All experiments were performed according to Institutional Animal Care and Use Committee standard procedures. C57BL/6J wild-type (Jackson Laboratory, stock 000664) mice between 2 and 6 months of age were used. Mice were housed in a vivarium with a reversed 12:12 h light:dark cycle and tested during the dark phase. No statistical methods were used to predetermine sample size. Behavioral experiments were not performed blinded as the experimental setup and analyses are automated.

Surgical procedures

Mice were administered carprofen (5 mg/kg) 30 minutes prior to surgery. Anesthesia was induced with inhalation of 2.5% isoflurane and buprenorphine (1.5 mg/kg) was administered at the onset of the procedure. Isoflurane (0.5-2.5% in oxygen, 1 L/min) was used to maintain anesthesia and adjusted based on the mouse's breath and reflexes. For all surgical procedures, the skin was removed from the top of the head and a custom titanium headplate was cemented to the leveled skull (Metabond, Parkell) and further secured with dental cement (Ortho-Jet powder, Lang Dental). Craniotomies were made using a 0.5 mm burr and viral vectors were delivered using pulled glass pipettes coupled to a microsyringe pump (Micro4, World Precision Instruments) on a stereotaxic frame (Model 940, Kopf Instruments). Following surgery, mice were allowed to recover in their home cages for at least 1 week.

Viral injections and implants

Coordinates for SC injections were ML: 1.1 mm, AP: 0.6 mm (relative to lambda), DV: -1.9 and -2.1 mm (100 nL/depth). Coordinates for SC implants were ML: 1.1 mm, AP: 0.6 mm (relative to lambda), DV: -2.0 mm. Fiber optic cannulae were constructed from ceramic ferrules (CFLC440-10, Thorlabs) and optical fiber (400 μ m core, 0.39 NA, FT400UMT) using low-autofluorescence epoxy (F112, Eccobond).

Behavioral procedures

To characterize stimulus-evoked gaze shifts (figures 2.2, 2.3, 2.4, 5 and related supplements), data were collected from 5 mice over 53 days (maximum of 1 session/mouse/day). Session types were randomly interleaved to yield a total of 6 ear airpuff sessions, 6 ear tactile sessions, 6 whisker airpuff sessions, 10 auditory airpuff sessions, and 5 visual sessions. During experiments, headplated mice were secured in a custom 3D-printed mouse holder. Timing and synchronization of the behavior were controlled by a microcontroller (Arduino MEGA 2560 Rev3, Arduino) receiving serial commands from custom MATLAB scripts. All behavioral and data acquisition timing information was recorded by a NI DAQ (USB-6001) for post hoc alignment. All experiments were performed using awake mice. Left and right stimuli were randomly selected and presented at intervals drawn from a 7-12 s uniform distribution. Each session consisted of 350 stimulus presentations and lasted ~55 minutes. No training or habituation was necessary.

Stimuli

Airpuff stimuli were generated using custom 3D-printed airpuff nozzles (1.5 mm wide, 10 mm long) connected to compressed air that was gated by a solenoid. 3D-

printed nozzles were used to standardize stimulus alignment across experimental setups, but similar results were obtained in preliminary experiments using a diverse array of nozzle designs. For whisker airpuffs, the nozzles were spaced 24 mm apart and centered 10 mm beneath the mouse's left and right whiskers. For ear airpuffs, the nozzles were directed toward the ears while maintaining 10 mm of separation between the nozzles and the mouse. For auditory-only airpuffs, the nozzles were directed away from the mouse while maintaining the same azimuthal position as the ear airpuffs. Whisker, ear, and auditory airpuffs produced a 65dB noise measured at the mouse's head. For tactile-only stimulation, the ears were deflected using a thin metal bar coated in epoxy to soften its edges (7122A37, McMaster). A stepper motor (Trinamic, QSH2818-32-07-006 and TMC2208) was programmed to sweep the bar downward against the ear before sweeping back up. The stepper motor was sandwiched between rubber pads (8514K61, McMaster) and elevated on rubber pedestals (20125K73, McMaster) to reduce any sound or tactile stimulation due to vibration. For visual stimulation, white LEDs (COM-00531, Sparkfun) were mounted 6 inches from the mouse at the same azimuthal position as the airpuff nozzles.

Eye tracking

The movements of both left and right eyes were monitored at 100 Hz using two high-speed cameras (BFS-U3-28S5M-C, Flir) coupled to a 110 mm working distance 0.5X telecentric lens (#67- 303, Edmund Optics). A bandpass filter (FB850-40, Thorlabs) was attached to the lens to block visible illumination. Three IR LEDs (475-1200-ND, DigiKey) were used to illuminate the eye and one was aligned to the camera's vertical axis to generate a corneal reflection. Videos were processed post hoc using

DeepLabCut, a machine learning package for tracking pose with user-defined body parts (Mathis et al., 2018). Data in this paper were analyzed using a network trained on 1000 frames of recorded behavior from 8 mice (125 frames per mouse). The network was trained to detect the left and right edges of the pupil and the left and right edges of the corneal reflection. Frames with a DeepLabCut-calculated likelihood of $P < 0.90$ were discarded from analyses. Angular eye position (E) was determined using a previously described method developed for C57BL/6J mice (Sakatani and Isa, 2004).

Attempted head rotation tracking

Attempted head rotations were measured using a 3D-printed custom headplate holder coupled to a load cell force sensor (Sparkfun, SEN-14727). Load cell measurements (sampling frequency 80 Hz) were converted to analog signals and recorded using a NI DAQ (sampling frequency 2000 Hz). The data were then low-pass filtered at 80 Hz using a zero-phase second-order Butterworth filter and then upsampled to match the pupil sampling rate.

Optogenetics

Optogenetic experiments were performed using the ear airpuff nozzles. Fiber optic cables were coupled to implanted fibers and the junction was shielded with black heat shrink. A 470 nm fiber-coupled LED (M470F3, Thorlabs) was used to excite ChR2-expressing neurons, and a 545 nm fiber-coupled LED (UHP-T-SR, Prizmatix) was used to inhibit eNpHR3.0-expressing neurons. Optogenetic excitation was delivered on a random 50% of trials using 1 s of illumination centered around airpuff onset.

SC inhibition

For optogenetic inactivation of SC neurons, *AAV1.hSyn.eNpHR3.0* was injected into the right SC of 5 wild-type mice (0.6 AP, 1.1 ML, -2.1 and -1.9 DV; 100 nL per depth). Experiments were performed 35-40 days post injection. LED power was 12 mW. Mice underwent 5 sessions each.

SC stimulation

To examine optogenetically-evoked gaze shifts in Figure 2.1, *AAV1.CaMKIIa.hChR2(H134R)-EYFP* was injected into the right SC of 4 wild-type mice. Experiments were performed 60-65 days post injection. For each mouse, SC was stimulated (1mW) for 40-ms every 7-12s for 350 trials.

To examine subthreshold optogenetic stimulation of SC neurons in Figure 2.6, *AAV1.CaMKIIa.hChR2(H134R)-EYFP* was injected into the right SC of 4 wild-type mice. Experiments were performed 67-71 days post injection. LED power was individually set to an intensity that did not consistently evoke saccades upon LED onset (50-120uW). Mice underwent 5 sessions each.

Histology

For histological confirmation of fiber placement and injection site, mice were perfused with PBS followed by 4% PFA. Brains were removed and post-fixed overnight in 4% PFA and stored in 20% sucrose solution for at least 1 day. Brains were sectioned at 50 μ m thickness using a cryostat (NX70, Cryostar), every third section was mounted, and slides were cover-slipped using DAPI mounting medium (Southern Biotech). Tile

scans were acquired using a confocal microscope (LSM700, Zeiss) coupled to a 10X air objective.

Behavioral analysis

Eye position analyses were performed using the averaged left and right pupil positions, and the mean eye position was subtracted from each session prior to combining data across sessions and mice. Similarly, because mice generate different ranges of raw strain gauge measurements when making attempted head rotations, attempted head rotation data was Z-scored prior to combining data across sessions and mice. Saccades were defined as eye movements that exceeded $100^{\circ}/s$, were at least 3° in amplitude, and were not preceded by a saccade in the previous 100 ms. The initial positions and endpoints of saccades were defined as the first points at which saccade velocity rose above $30^{\circ}/s$ and fell below $20^{\circ}/s$, respectively. Analyses focused on horizontal saccades because saccades were strongly confined to the azimuthal axis (Figure S2.1). For all subsequent analyses, saccades were defined as being evoked by a sensory or optogenetic stimulus if they occurred within a 100 ms response window following stimulus delivery, selected due to the sharp increase in saccade probability during this period (Figure S2.1). Spontaneous saccades were a catch-all category defined as any saccades made outside of an experimental stimulus (i.e., no stimulus in the 500 ms periods preceding or following the saccade).

To examine stimulation-evoked gaze shifts (Figure 2.1), only trials in which the head and eyes were fixated in the 500ms period preceding LED-onset and in which the eyes began in a central orbital position (-2° to 0°) were used for analysis. Head movement amplitude during gaze shifts was defined as the head sensor reading 150ms

after saccade onset. Head movement onset was defined as the point relative to LED-onset at which head displacement exceeded 5 standard deviations from baseline.

To quantify stimulus-evoked saccade probability (Figure 2.2), we calculated the fraction of trials in which a saccade occurred in the 100 ms period following stimulus onset. To quantify stimulus-evoked attempted head movement probability, we calculated the fraction of trials in which the head sensor reading exceeded 0.25Z at the point 150 ms following stimulus onset. To determine the baseline head movement probability, we calculated the fraction of trials in which the head sensor reading exceeded 0.25Z between -500 ms and -350 ms relative to stimulus onset.

To examine saccade endpoints, we first identified trials in which mice maintained fixation in the 500 ms preceding saccade onset. We then considered stimulus-evoked saccades those occurring within 100 ms of stimulus onset. To examine the amplitudes of attempted head movements accompanying stimulus-evoked saccades, we used the head sensor reading 150ms following saccade onset.

Heatmaps of single-trial head movements (Figure 2.4, Figure S2.7) were sorted by head movement latency. To calculate attempted head movement latencies, we identified trials in which mice maintained head fixation from -1 to -0.5 s prior to saccade onset and used this period as the baseline. Latency was defined as the first frame between -0.5 and 0.5 s relative to saccade onset when the attempted head movement amplitude exceeded 5 standard deviations from that trial's baseline (~ 0.05 - $0.1Z$).

To examine the timing of attempted head movements relative to saccade onset (Figure 2.4), we first baseline subtracted attempted head movement traces 500 ms

before saccade onset for each trial. For each time point between -500 ms to 500 ms surrounding saccade onset, we calculated the fraction of trials with instantaneous attempted head movements that were ipsiversive to their accompanying saccades.

To examine head-eye amplitude coupling during spontaneous and stimulus-evoked gaze shifts, we defined attempted head rotation displacement as the load cell value 150 ms following saccade onset (the time point at which average load cell value plateaus during stimulus-evoked gaze shifts (Figure 2.4)). For certain analyses, we identified saccades matched (without replacement) for initial eye position and/or saccade amplitude using Euclidean distance as a metric and a 3° distance cutoff. For a subset of analyses, we used attempted head movement velocity which was measured 60 ms after saccade onset (the time point when average load cell velocity peaks).

To examine the relationship between initial eye position and stimulus-evoked saccade or head movement probability, we identified trials in which mice did not saccade in the 500 ms preceding stimulus onset. Left and right head movements were defined as those less than -0.25Z or greater than 0.25Z, respectively. Qualitatively similar results were obtained using thresholds ranging from 0.1Z to 2Z. To examine the relationship between initial eye position and spontaneous saccade or head movement probability, we identified 1 s long time periods in which no stimuli were delivered and in which mice did not saccade in the first 500 ms. We then determined the probability of a saccade between 500-600 ms, and the probability of a head movement using the head sensor value at 650ms.

Tests for statistical significance are described in the text and figure legends. Data were shuffled 10,000 times to generate a null distribution for permutation tests.

2.6 FIGURES

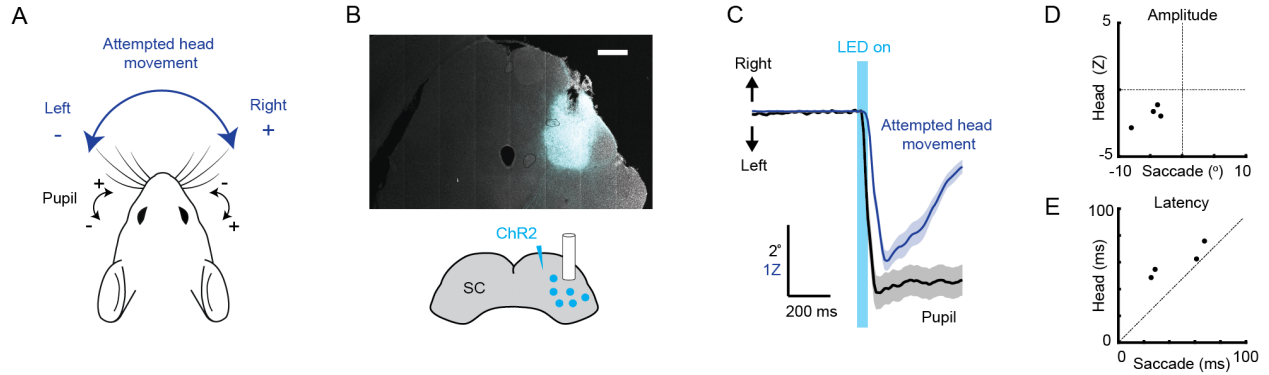


Figure 2.1: Optogenetic stimulation of the superior colliculus evokes coincident and directionally biased attempted head and eye movements

(A) Behavioral schematic. Naïve mice are head-fixed and both eyes are tracked using cameras and attempted head rotations are measured using a strain gauge (load cell). In subsequent quantification, eye positions to the right of center (nasal for left eye, temporal for right eye) are positive, and eye positions to the left of center (temporal for left eye, nasal for right eye) are negative, with zero defined as the mean eye position. Left and right eye positions are averaged together unless otherwise noted. Likewise, attempted rightward head movements are positive, and leftward head movements are negative. **(B)** Schematic of right SC optogenetic stimulation using ChR2 and example histology for representative mouse. Scale bar, 0.5 mm. **(C)** Mean attempted head (blue) and eye (black) movement traces ($n = 44$ trials, 4 mice) in the 1 s period surrounding optogenetic stimulation. Optogenetic illumination (1 mW) was delivered for 40ms. **(D)** Relationship between saccade amplitude and attempted head movement amplitude for individual mice. **(E)** Relationship between saccade latency and head movement latency for individual mice.

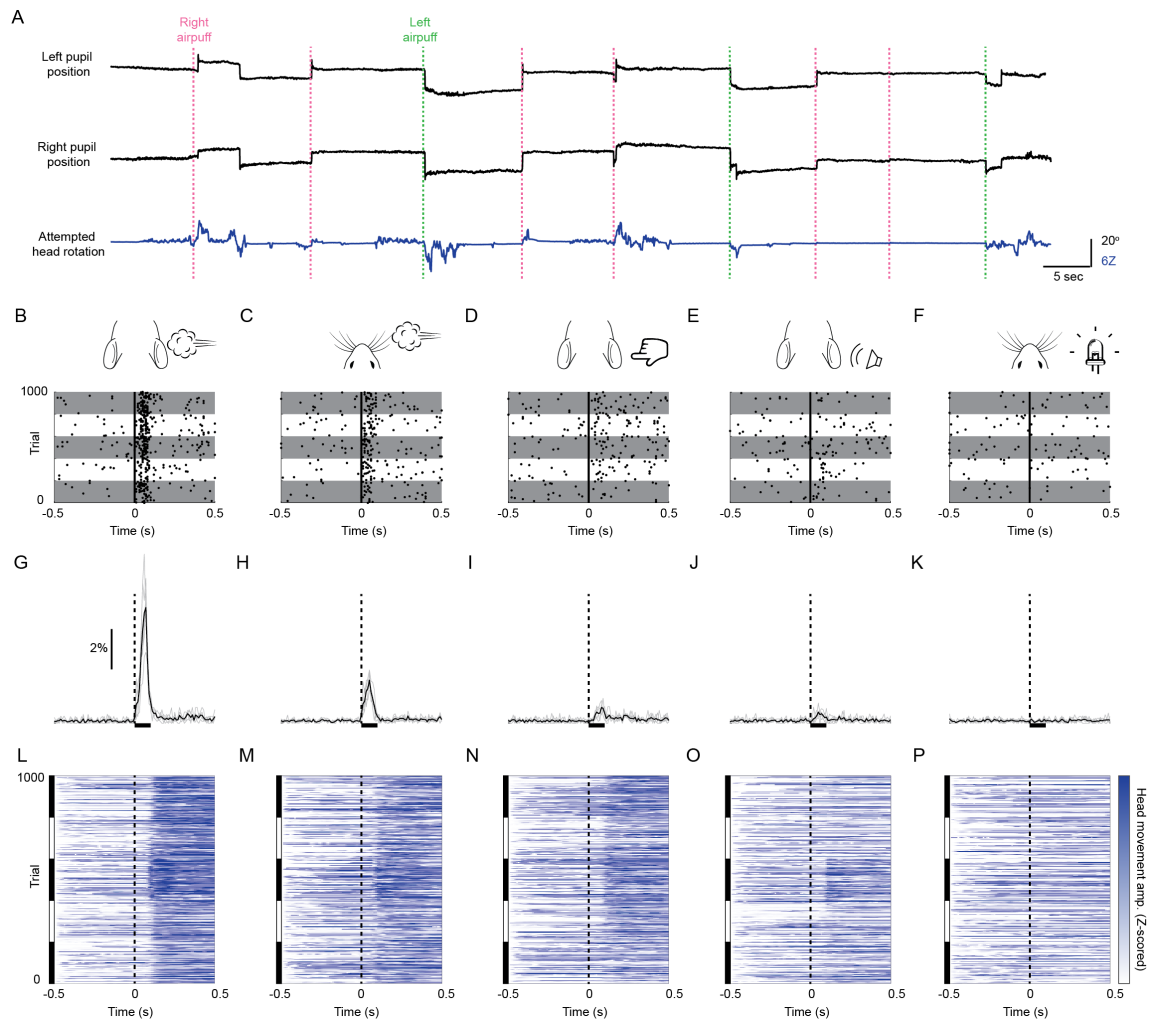


Figure 2.2: Mice innately make sound- and touch-evoked gaze shifts

(A) Sample eye and attempted head movement traces. Dashed vertical lines indicate right (green) and left (magenta) ear airpuff delivery. **(B-F)** Saccade rasters for 5 representative mice in response to (B) ear airpuffs, (C) whisker airpuffs, (D) ear tactile stimuli, (E) auditory airpuffs, and (F) visual stimuli. Each row corresponds to a trial. Each dot indicates onset of a saccade. Vertical black lines denote time of left or right stimulus delivery. Each gray or white horizontal stripe contains data for a different mouse. $n = 1000$ randomly selected trials (200/mouse). **(G-K)** Peri-stimulus time histograms showing instantaneous saccade probabilities in response to (G) ear airpuffs, (H) whisker airpuffs, (I) ear tactile stimuli, (J) auditory airpuffs, and (K) visual stimuli for mice from (B-F). Each light trace denotes a single animal; black traces denote population mean. Dashed lines denote time of stimulus delivery. Horizontal bar indicates the 100 ms response window used in subsequent analyses. **(L-P)** Heatmaps of attempted head movements in response to (L) ear airpuffs, (M) whisker airpuffs, (N) ear tactile stimuli, (O) auditory airpuffs, and (P) visual stimuli for mice from (B-K). Each row corresponds to an individual trial from B-F. Black and white bars at left indicate blocks of trials corresponding to each of 5 different mice. Dashed line denotes stimulus delivery time.

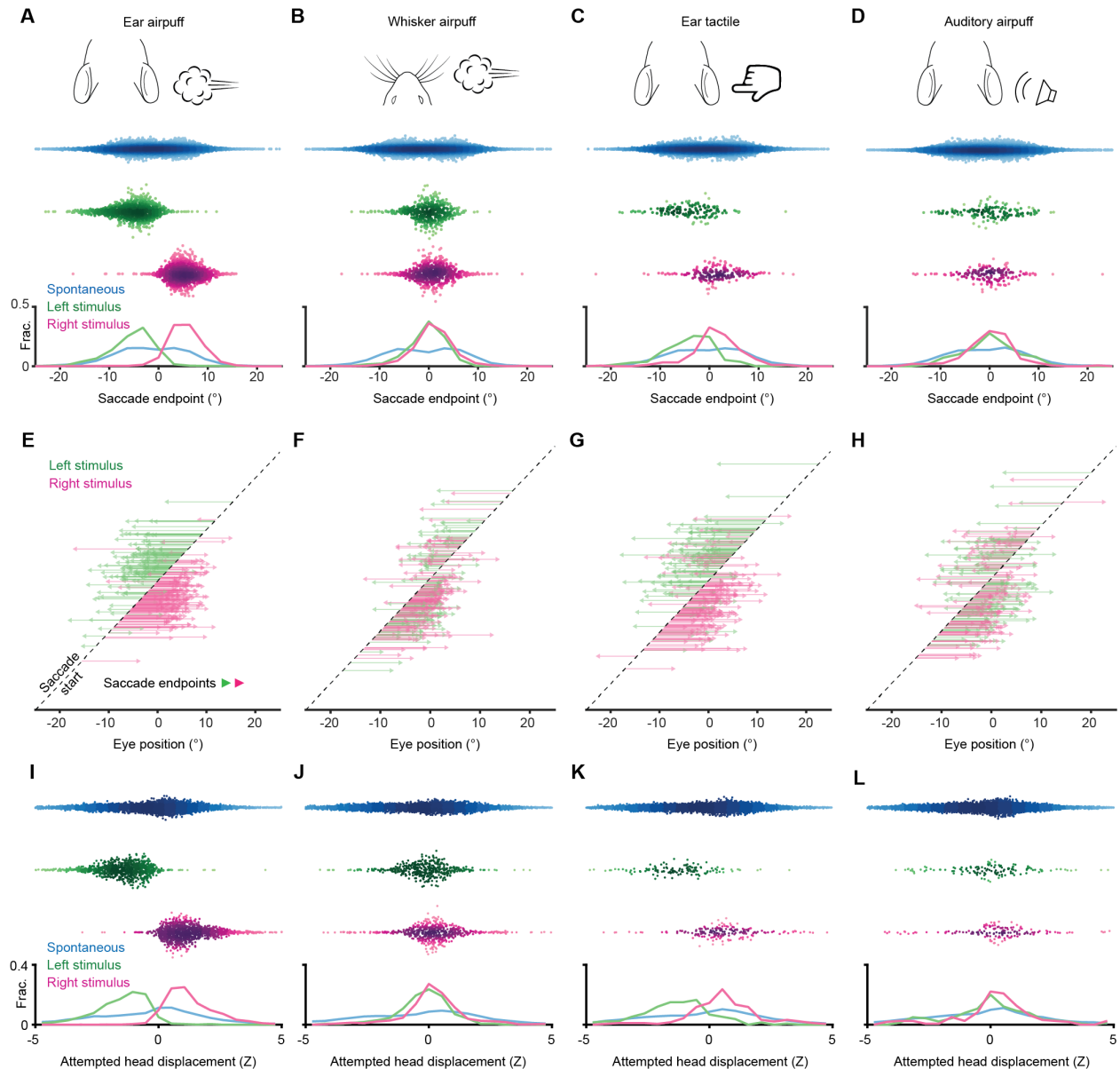


Figure 2.3: Sensory-evoked eye and attempted head movements

(A-D) Endpoints for ear airpuff-, whisker airpuff-, ear tactile-, and auditory airpuff-evoked saccades. Top, schematics of stimuli. Middle, scatter plots showing endpoints of all saccades for all animals ($n =$ see below, 5 animals) made spontaneously (blue) and in response to left (green) and right (magenta) stimuli. Darker shading indicates areas of higher density. Bottom, histograms of endpoint distributions for spontaneous and evoked saccades. (E-H) Trajectories of individual stimulus-evoked saccades. Each arrow denotes the trajectory of a single saccade. Saccades are sorted according to initial eye positions, which fall on the dashed diagonal line. Saccade endpoints are indicated by arrowheads. Because the probability of evoked gaze shifts differed across stimuli, data for ear and whisker airpuffs are randomly subsampled (15% and 30% of (legend continued on next page)

(legend continued from the previous page)

total trials, respectively) to show roughly equal numbers of trials for each condition. **(I-L)** Ear airpuff-, whisker airpuff-, ear tactile-, and auditory airpuff-evoked attempted head displacements associated with saccades in A-D. Top, scatter plots showing displacements of attempted head movements associated with saccades made spontaneously (blue) and in response to left (green) and right (magenta) stimuli (n = see below, 5 animals). Darker shading indicates areas of higher density. Bottom, histograms of attempted displacement distributions for spontaneous and evoked attempted head movements. Saccade numbers in A-L: ear airpuff sessions, spontaneous = 7146, left ear airpuff-evoked = 942 (141 in E), right ear airpuff-evoked = 1213 (182 in E); whisker airpuff sessions: spontaneous = 7790, left whisker airpuff-evoked = 440 (132 in F), right whisker airpuff-evoked = 606 (181 in F); ear tactile sessions, spontaneous = 6706, left ear tactile-evoked = 133, right ear tactile-evoked = 186; auditory sessions, spontaneous = 10240, left auditory-evoked = 140, right auditory-evoked = 158.

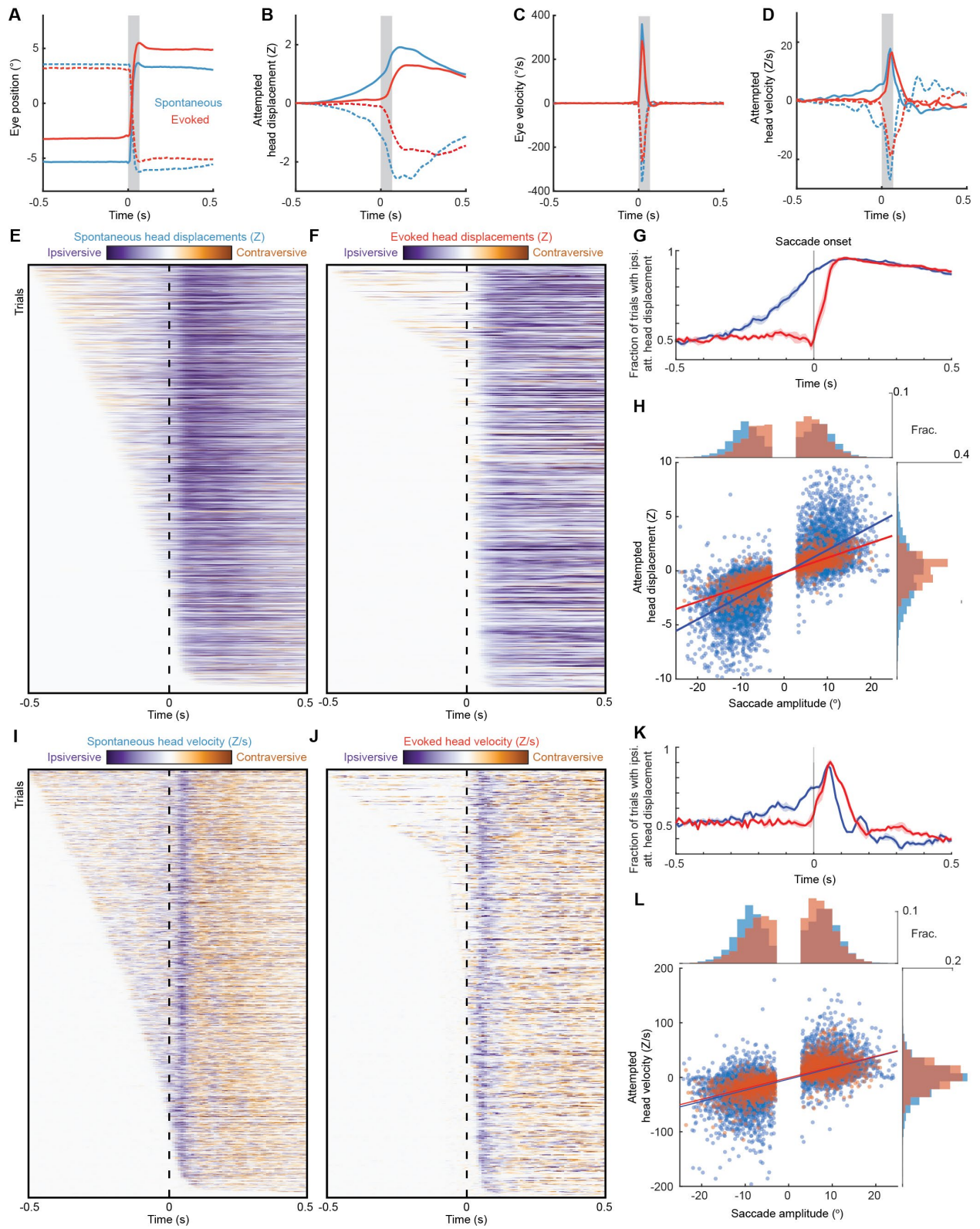


Figure 2.4: Head-eye coupling during spontaneous and touch-evoked gaze shifts

(A) Mean trajectories of all rightward (solid traces) and leftward (dashed traces) saccades during spontaneous (blue, $n = 7146$) and ear airpuff-evoked (red, $n = 1437$) gaze shifts. Means + s.e.m. (smaller than line width). Gray bar indicates average saccade duration. **(B)** Mean attempted head displacement accompanying rightward (solid traces) and leftward (dashed traces) saccades during spontaneous (blue) and ear airpuff-evoked (red) gaze shifts. **(C)** Mean velocities of all rightward (solid traces) and leftward (dashed traces) saccades during spontaneous (blue) and ear airpuff-evoked (red) gaze shifts. **(D)** Mean attempted head movement velocities accompanying rightward (solid traces) and leftward (dashed traces) saccades during spontaneous (blue) and ear airpuff-evoked (red) gaze shifts. **(E, F)** Timing of attempted head movements relative to saccades during all spontaneous (E) and ear airpuff-evoked (F) gaze shifts. Each row corresponds to a single gaze shift. Darker shades indicate larger attempted head displacement. Purple hues denote attempted displacement in the same direction as the saccade (ipsiversive), and orange hues denote displacement in the opposite direction of the saccade (contraversive). Dashed vertical line indicates time of saccade onset. Trials are sorted by latency of attempted head movements. **(G)** Fraction of trials with ipsiversive attempted head displacements at different timepoints relative to saccade onset for spontaneous (blue) and evoked (red) saccades. **(H)** Head-eye amplitude coupling of spontaneous (blue) and ear airpuff-evoked saccades (red). Each dot corresponds to a single gaze shift. Attempted head amplitude was measured 150 ms after saccade onset. Spontaneous: $R^2 = 0.58$, slope = 0.214, $p < 10^{-10}$. Evoked: $R^2 = 0.64$, slope = 0.162, $p < 10^{-10}$. Spontaneous and evoked regression slopes were significantly different ($p < 10^{-5}$, permutation test). Histograms above and beside scatter plot indicate distributions of saccade and attempted head movement amplitudes. Difference in means significant ($p < 10^{-5}$ for saccades, $p < 10^{-5}$ for head, permutation test). **(I-J)** As in (E-F), but for attempted head movement velocity. **(K)** As in (G), but for attempted head movement velocity. **(L)** As in (H), but for attempted head movement velocity. Peak attempted head velocity was measured 60 ms after saccade onset. Spontaneous: $R^2 = 0.40$, slope = 2.04, $p < 10^{-10}$. Evoked: $R^2 = 0.52$, slope = 1.98, $p < 10^{-10}$. Spontaneous and evoked regression slopes were not significantly different ($p = 0.08$, permutation test). Histograms above and beside scatter plot indicate distributions of saccade amplitudes and peak attempted head velocities. Difference in means was significant ($p < 10^{-5}$ for saccades, $p < 10^{-5}$ for head, permutation test).

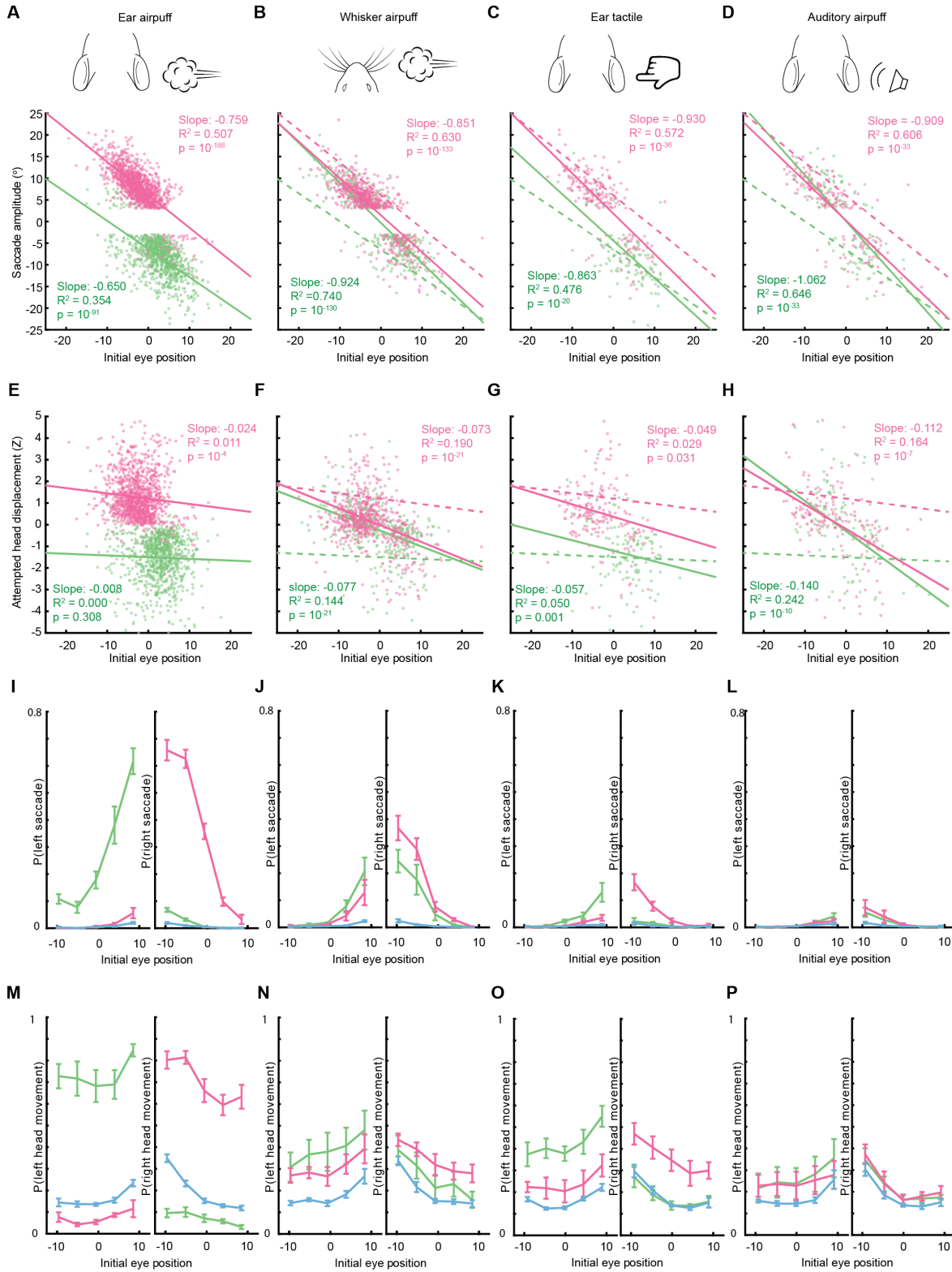


Figure 2.5: Saccade and head movement direction, amplitude, and probability depend on initial eye position

(A-D) Relationship between saccade amplitude and eye position for left ear airpuffs (A, slope = -0.650, $R^2 = 0.354$, $p = 10^{-91}$), right ear airpuffs (A, slope = -0.759, $R^2 = 0.507$, $p = 10^{-188}$), left whisker airpuffs (B, slope = -0.924, $R^2 = 0.740$, $p = 10^{-130}$), right whisker airpuffs (B, slope = -0.851, $R^2 = 0.630$, $p = 10^{-133}$), left ear tactile (C, slope = -0.863, $R^2 = 0.476$, $p = 10^{-20}$), right ear tactile (C, slope = -0.930, $R^2 = 0.572$, $p = 10^{-36}$), left auditory airpuffs (D, slope = -1.062, $R^2 = 0.646$, $p = 10^{-33}$), and right auditory airpuffs (D, slope = -0.909, $R^2 = 0.606$, $p = 10^{-33}$). Dotted lines in B-D are lines of best fit from A for comparison. **(E-H)** Relationship between attempted head displacement and eye position for left ear airpuffs (E, slope = -0.008, $R^2 = 0.000$, $p = 0.308$), right ear airpuffs (E, slope = -0.024, $R^2 = 0.011$, $p = 10^{-4}$), left whisker airpuffs (F, slope = -0.077, $R^2 = 0.144$, $p = 10^{-21}$), right whisker airpuffs (F, slope = -0.073, $R^2 = 0.190$, $p = 10^{-21}$), left ear tactile (G, slope = -0.057, $R^2 = 0.050$, $p = 0.001$), right ear tactile (G, slope = -0.049, $R^2 = 0.029$, $p = 0.031$), left auditory airpuffs (H, slope = -0.140, $R^2 = 0.242$, $p = 10^{-10}$), and right auditory airpuffs (H, slope = -0.112, $R^2 = 0.164$, $p = 10^{-7}$). Dotted lines in F-H are lines of best fit from E. The trials in A-H are the same as those in Figure 2.2. **(I-L)** Relationship between eye position and saccade probability for left and right saccades. **(M-P)** Relationship between eye position and attempted head movement probability for left and right attempted head movements. Green and magenta lines in I-P indicate population means for movements evoked by left and right stimuli, respectively. Blue lines indicate spontaneous saccades or head movements. Error bars indicate s.e.m. Total trial numbers for I-P: ear airpuff sessions, spontaneous = 13384, left ear airpuff = 3506, right ear airpuff = 3497; whisker airpuff sessions, spontaneous = 14511, left whisker airpuff = 3926, right whisker airpuff = 4026; tactile ear sessions, spontaneous = 13529, left tactile ear = 3646, right tactile ear = 3695; auditory airpuff, spontaneous = 13404, left auditory airpuff = 6362, right auditory airpuff = 6385.

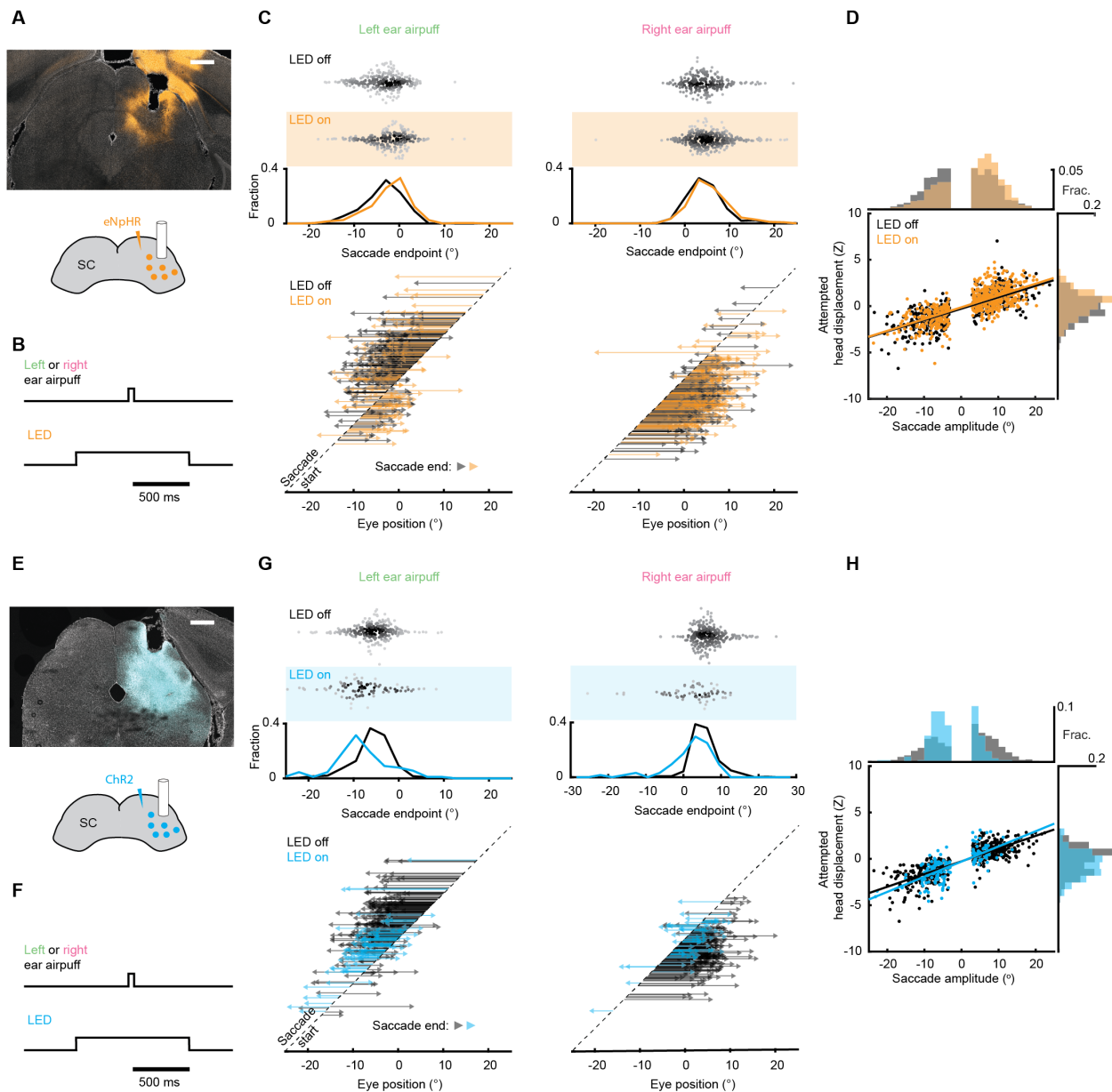


Figure 2.6: Superior colliculus controls touch-evoked gaze shifts

(A) Schematic of right SC optogenetic inhibition using eNpHR3.0 and example histology for representative mouse. Scale bar, 0.5 mm. The lack of fluorescence immediately surrounding fiber tip is due to photobleaching by high photostimulation intensity (12 mW, as opposed to 50-120 μ W for ChR2 experiments in (E-H)). (B) Trial structure. Optogenetic illumination is provided for a 1 s period centered around airpuff delivery. (C) Effects of SC optogenetic inhibition on saccade endpoints. Top, scatter plots and histograms of endpoints for control (white background, $n = 296$) and LED on (orange background, $n = 235$) trials. Middle, endpoint histograms for control (black) and LED on (orange) trials. Bottom, saccade vectors for control (black) and LED on (orange) trials. (D) Head-eye amplitude coupling during ear airpuff-evoked gaze shifts for control

(legend continued on next page)

(legend continued from the previous page)

(black) and LED on (orange) trials. Each dot represents an individual gaze shift. Control: $R^2 = 0.56$, slope = 0.123, $p < 10^{-10}$. LED on: $R^2 = 0.53$, slope = 0.127, $p < 10^{-10}$. Control and LED on regression slopes were significantly different ($p=0.01$, permutation test) due to differences in eye positions from which gaze shifts were generated, because controlling for initial eye position eliminated this difference (Figure S2.15). Histograms above and beside scatter plot show distributions of saccade amplitudes and attempted head displacements, respectively. Distribution means were significantly different ($p < 10^{-5}$, permutation test). **(E)** Schematic of right SC optogenetic subthreshold stimulation using ChR2 and example histology for representative mouse. Scale bar, 0.5 mm. **(F)** Trial structure. Optogenetic illumination is provided for a 1 s period centered around airpuff delivery. **(G)** Effects of weak SC optogenetic stimulation on saccade endpoints. Top, scatter plots and histograms of endpoints for control (white background, $n = 547$) and LED on (blue background, $n = 157$) trials. We observed fewer trials in the LED-on condition because SC stimulation increased the probability of spontaneous saccades prior to stimulus onset, and trials with saccades in the 500 ms before stimulus delivery were excluded from analysis. Middle, histograms of endpoints for control (black) and LED on (blue) trials. Bottom saccade vectors for control (black) and LED on (blue) trials. **(H)** Head-eye amplitude coupling during ear airpuff-evoked gaze shifts for control (black) and LED on (blue) trials. Each dot represents an individual gaze shift. Attempted head amplitude was measured 150 ms after saccade onset. Control: $R^2 = 0.69$, slope = 0.137, $p < 10^{-10}$. LED on: $R^2 = 0.52$, slope = 0.164, $p < 10^{-10}$. Control and LED-on regression slopes were significantly different ($p < 10^{-5}$, permutation test) due to difference in eye positions from which gaze shifts were generated, because controlling for initial eye position eliminated this difference (Figure S2.15). Histograms above and beside scatter plot show distributions of saccade amplitudes and attempted head displacements, respectively. Distribution means were significantly different ($p < 10^{-5}$, permutation test).

2.7 SUPPLEMENTAL FIGURES

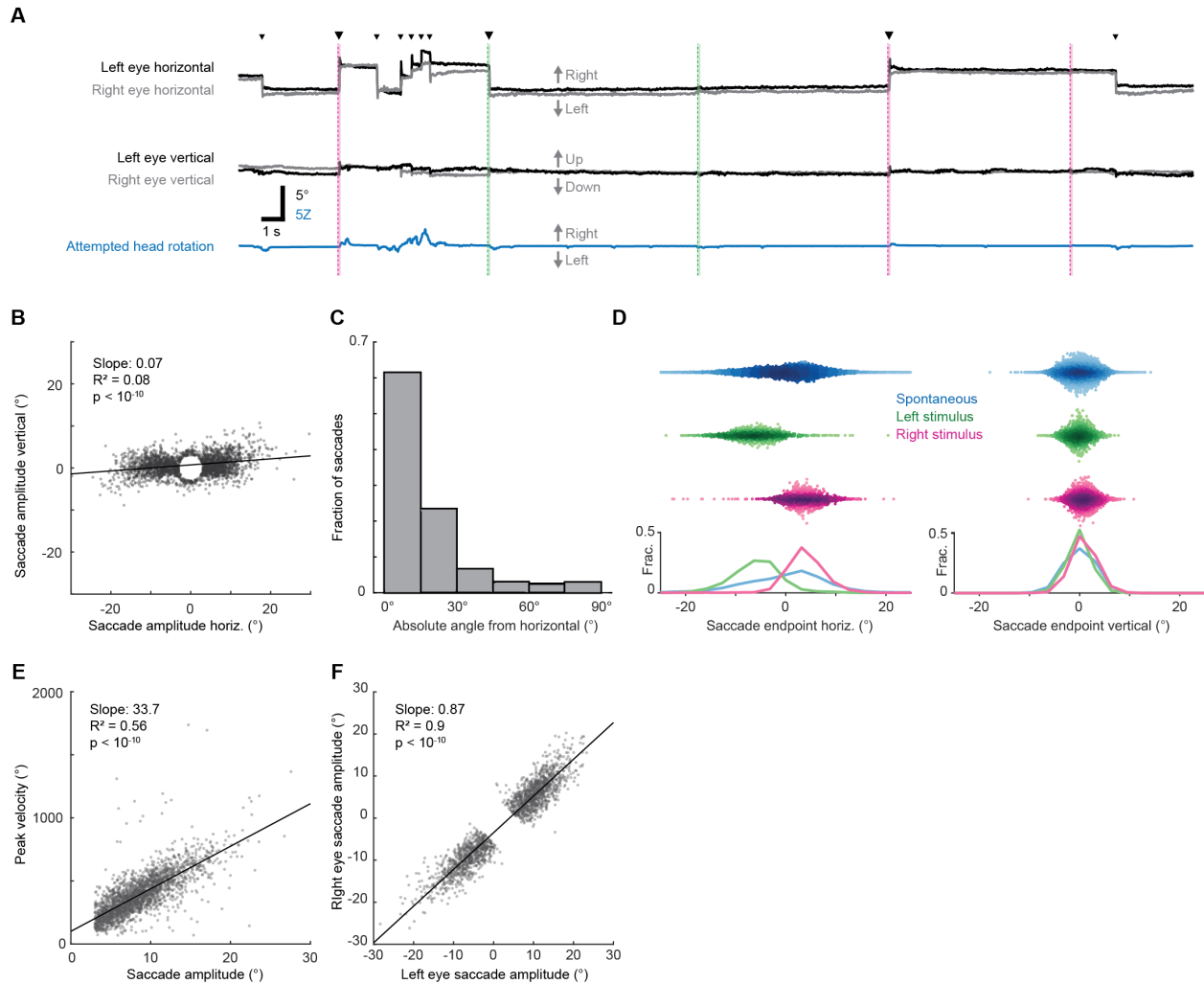


Figure S2.1: Airpuffs evoke horizontal saccades

(A) Sample traces showing pupil azimuth (top) and elevation (middle) and attempted head rotation (bottom). Black corresponds to left eye, gray corresponds to right eye. Small arrowheads indicate spontaneous saccades. Large arrowheads indicate stimulus-evoked directionally biased saccades. Green and magenta dashed vertical lines correspond to left and right ear airpuffs, respectively. **(B)** Ear airpuff-evoked saccade endpoints and linear fit. $n = 5$ mice, 2337 trials. **(C)** Distribution of angles between airpuff-evoked saccade vectors and horizontal axis. Gray bars indicate population means. $n = 5$ mice, 2337 trials **(D)** Distributions of saccade endpoints in horizontal and vertical axes. $n = 5$ mice; trials = 16291 (spontaneous), 1067 (left airpuff), 1270 (right airpuff). **(E)** Relationship between saccade amplitude and peak velocity. **(F)** Relationship between right and left eye saccade amplitudes. $n = 4$ mice, 1861 trials.

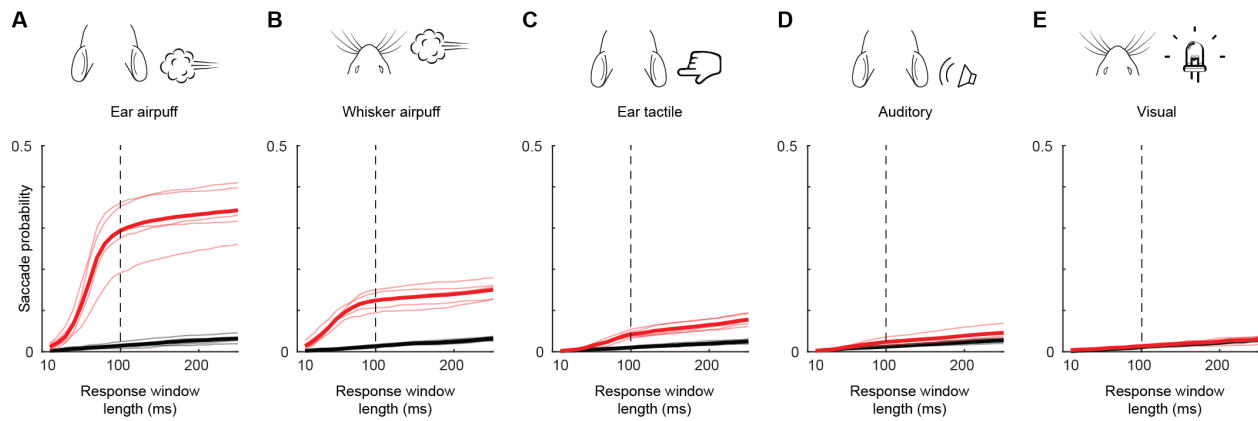


Figure S2.2: Evoked saccades occur within a narrow window after stimulus delivery

(A-E) Cumulative probabilities of detecting evoked (red) and spontaneous (black) saccades as a function of response window length for ear airpuffs (A), whisker airpuffs (B), ear tactile stimuli (C), auditory airpuffs (D), and visual stimuli (E). Thin lines denote values for individual mice, thick lines denote population mean. Dashed vertical line indicates end of window used for analyses of evoked saccades.

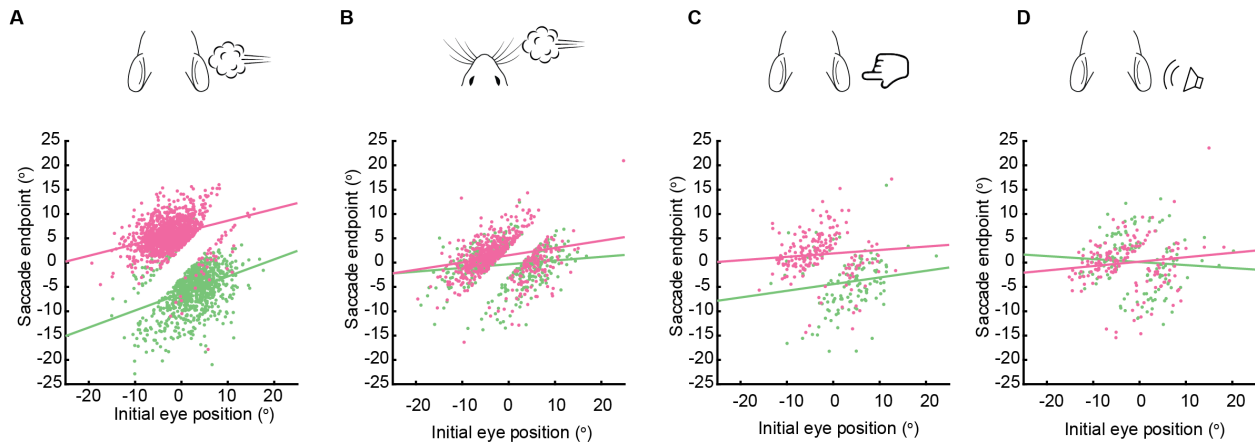


Figure S2.3: Saccade endpoints as a function of initial eye position

(A-D) Relationship between saccade endpoint and initial eye position for left ear airpuffs (A, slope = 0.350, $R^2 = 0.137$, $p = 10^{-32}$), right ear airpuffs (A, slope = 0.241, $R^2 = 0.093$, $p = 10^{-28}$), left whisker airpuffs (B, slope = 0.076, $R^2 = 0.017$, $p = 0.004$), right whisker airpuffs (B, slope = 0.149, $R^2 = 0.048$, $p = 10^{-8}$), left whisker tactile (C, slope = 0.134, $R^2 = 0.015$, $p = 0.084$), right whisker tactile (C, slope = 0.070, $R^2 = 0.002$, $p = 0.236$), left auditory airpuffs (D, slope = -0.062, $R^2 = 0.001$, $p = 0.356$), and right auditory airpuffs (D, slope = 0.070, $R^2 = 0.009$, $p = 0.122$). n = same as Figure 2.3.

A

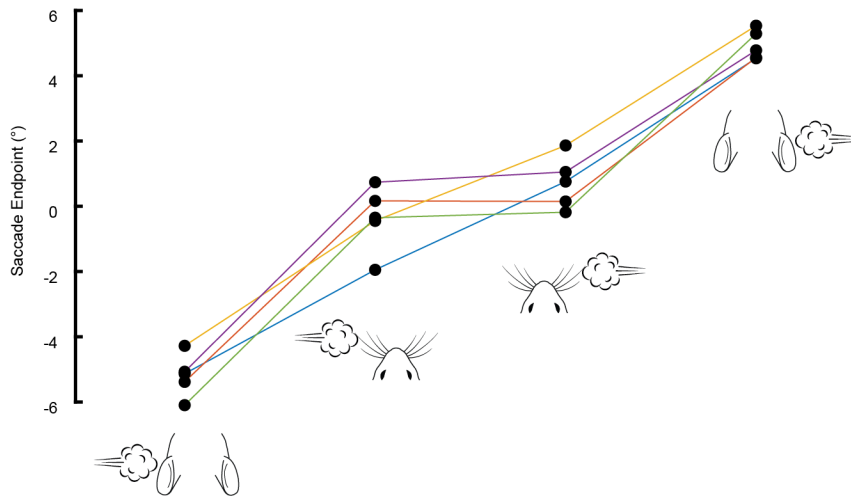


Figure S2.4: Endpoints of airpuff-evoked saccades are ordered according to site of stimulation

Each line corresponds to a single mouse and shows mean endpoint of saccades evoked by (in order, from left to right) left ear airpuffs, left whisker airpuffs, right whisker airpuffs, and right ear airpuffs).

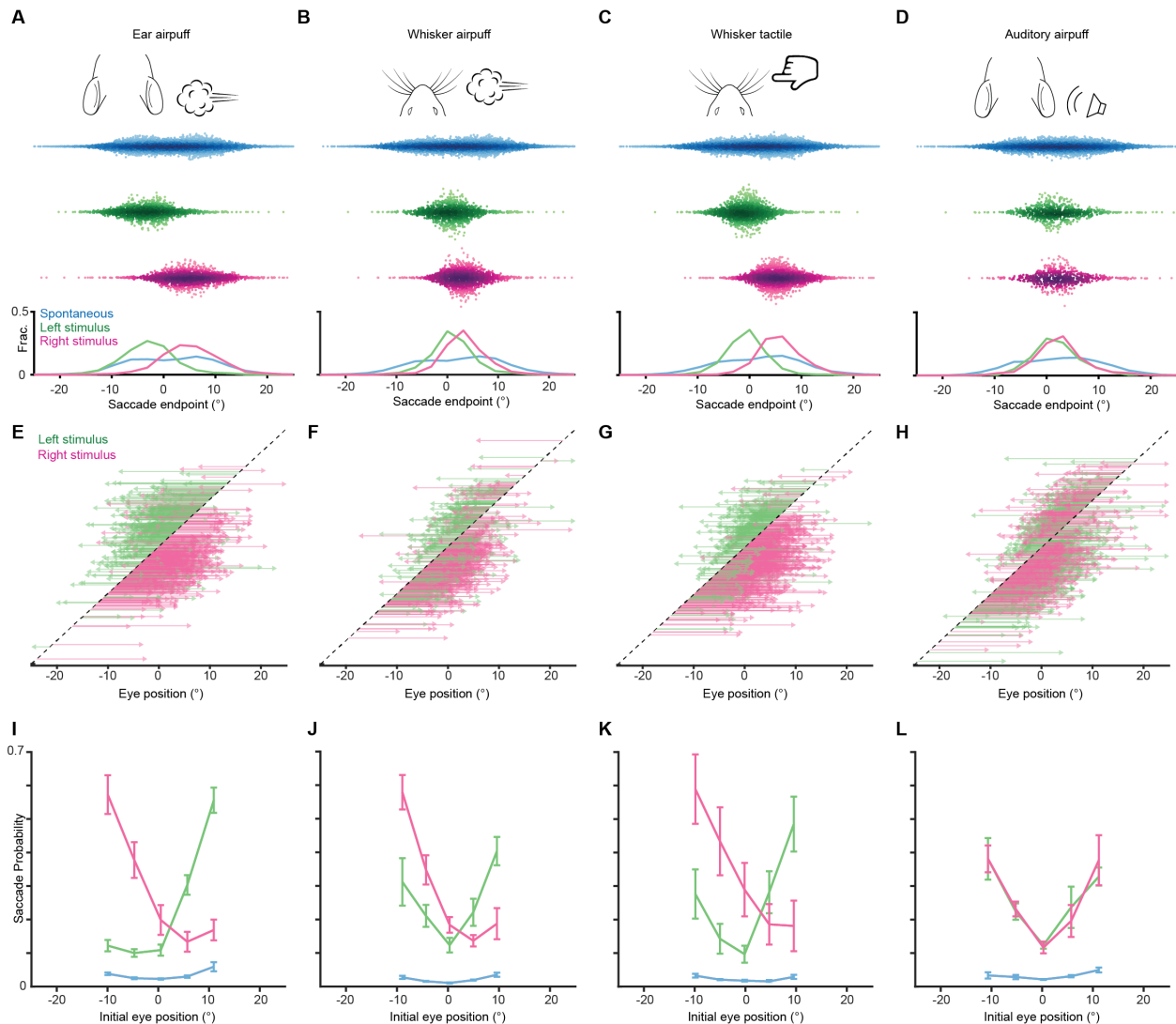


Figure S2.5: Endpoints and trajectories of sensory-evoked saccades for an additional cohort of mice

(A-D) Endpoints for ear airpuff-, whisker airpuff-, ear tactile-, and auditory airpuff-evoked saccades. Top, schematics of stimuli. Middle, scatter plots showing endpoints of all saccades for all animals made spontaneously (blue) and in response to left (green) and right (magenta) stimuli. Darker shading indicates areas of higher density. Bottom, endpoint distributions for spontaneous and evoked saccades. **(E-H)** Trajectories of individual stimulus-evoked saccades. Each arrow denotes the trajectory of a single saccade. Saccades are sorted according to initial eye positions, which fall on the dashed diagonal line. Saccade endpoints are indicated by arrowheads. Because the probability of evoked gaze shifts differed across stimuli, data are randomly subsampled to show roughly equal numbers of trials for each condition. **(I-L)** Relationship between eye position and saccade probability. Green and magenta lines indicate population means for saccades evoked by left and right stimuli, respectively. Blue lines indicate spontaneous saccades. Error bars indicate s.e.m Saccade numbers for A-L: ear airpuff (*legend continued on next page*)

(legend continued from previous page)

sessions, spontaneous = 14304, left ear airpuff-evoked = 1221 (244 in E), right ear airpuff-evoked = 1755 (351 in E); whisker airpuff sessions, spontaneous = 8971, left whisker airpuff-evoked = 1107 (221 in F), right whisker airpuff-evoked = 1482 (296 in F); whisker tactile sessions, spontaneous = 13242, left whisker-evoked = 1473 (294 in G), right whisker-evoked = 2408 (481 in G); auditory sessions, spontaneous = 8774, left auditory-evoked = 833 (333 in H), right auditory-evoked = 757 (302 in H).

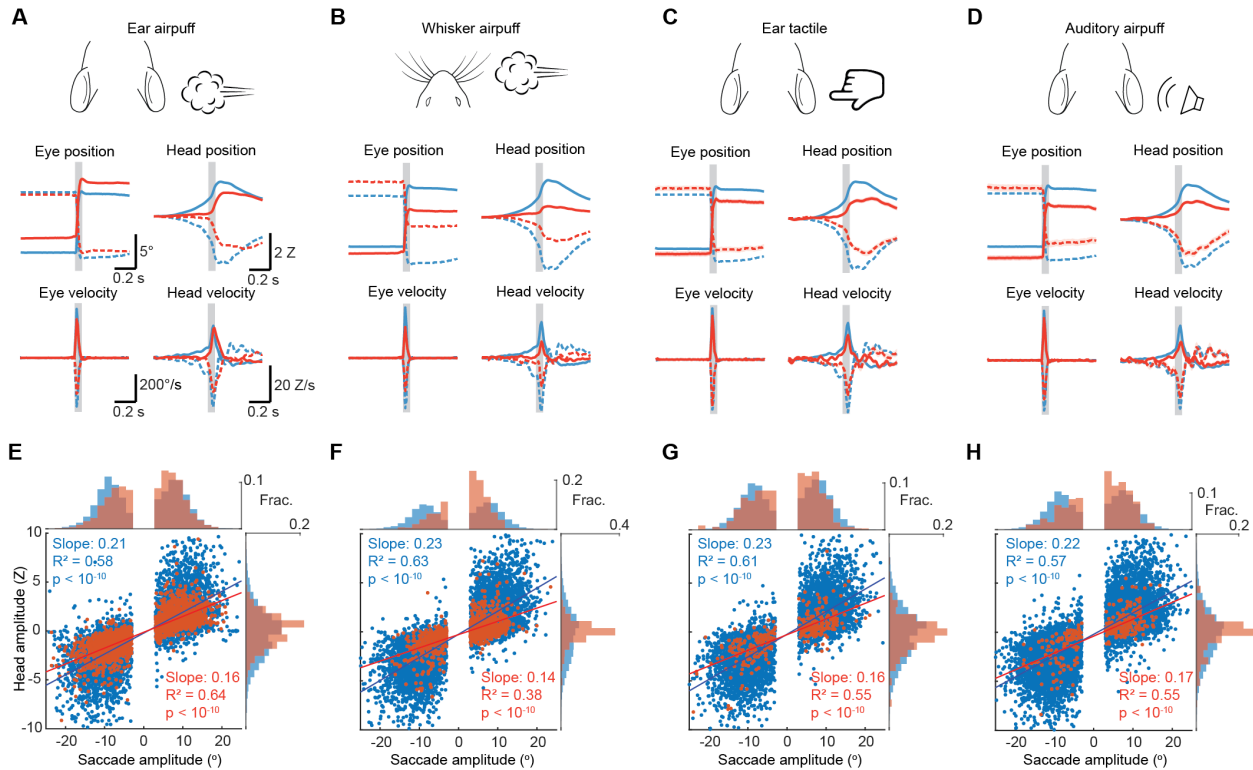


Figure S2.6: Head-eye coupling for different stimuli

(A) Top, stimulus schematics. Middle left, mean trajectories of rightward (solid traces) and leftward (dashed traces) saccades during spontaneous (blue, $n = 7146$) and ear airpuff-evoked (red, $n = 2151$) gaze shifts. Middle right, mean attempted head displacement accompanying rightward (solid traces) and leftward (dashed traces) saccades during spontaneous (blue) and ear airpuff-evoked (red) gaze shifts. Bottom left, mean velocities of all rightward (solid traces) and leftward (dashed traces) saccades during spontaneous (blue) and ear airpuff-evoked (red) gaze shifts. Bottom right, mean attempted head movement velocities accompanying rightward (solid traces) and leftward (dashed traces) saccades during spontaneous (blue) and ear airpuff-evoked (red) gaze shifts. (B-D) As in (A) for whisker airpuffs (B), ear tactile (C) and auditory airpuffs (D). $n = 5$ mice. Trial numbers: whisker airpuff sessions (spontaneous = 7790, evoked = 1057), ear tactile sessions (spontaneous = 6706, evoked = 322), auditory airpuff sessions (spontaneous = 10240, evoked = 301). (E-H). Head-eye amplitude coupling of spontaneous (blue) and evoked saccades (red). Each dot corresponds to a single gaze shift. Regression statistics in figure. For every stimulus type, spontaneous and evoked regression slopes were significantly different ($p < 10^{-5}$, permutation test). Histograms above and beside scatter plot indicate distributions of saccade and attempted head movement amplitudes, respectively. For each condition, distributions were significantly different between spontaneous and evoked ($p < 10^{-5}$, permutation test).

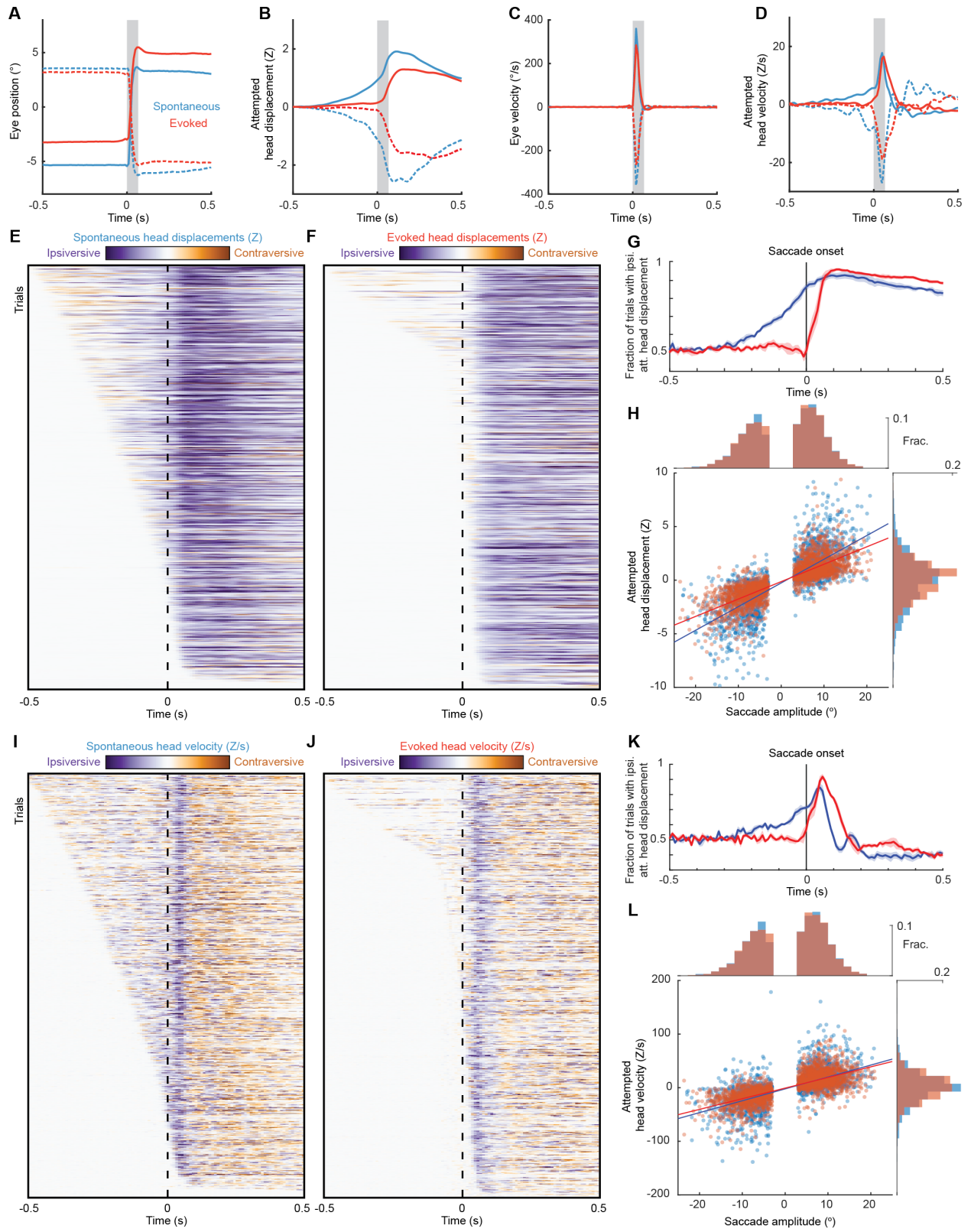


Figure S2.7: Different head-eye coupling during spontaneous and touch-evoked gaze shifts is not due to differences in saccade start and end points

As in Figure 2.4, but with spontaneous and touch-evoked trials matched for initial eye position and saccade amplitude. **(A)** Mean trajectories of rightward (solid traces) and leftward (dashed traces) saccades during spontaneous (blue, $n = 2149$, 5 mice) and ear airpuff-evoked (red, $n = 2149$) gaze shifts. **(B)** Mean attempted head movement amplitudes accompanying rightward (solid traces) and leftward (dashed traces) saccades during spontaneous (blue) and ear airpuff-evoked (red) gaze shifts. **(C)** Mean velocities of all rightward (solid traces) and leftward (dashed traces) saccades during spontaneous (blue) and ear airpuff-evoked (red) gaze shifts. **(D)** Mean head movement velocities accompanying rightward (solid traces) and leftward (dashed traces) saccades during spontaneous (blue) and ear airpuff-evoked (red) gaze shifts. **(E, F)** Timing of attempted head movements relative to saccades during all spontaneous (E) and ear airpuff-evoked (F) gaze shifts. Each row corresponds to a single gaze shift. Darker shades indicate larger attempted head displacement. Purple hues denote attempted displacement in the same direction as the saccade (ipsiversive), and orange hues denote displacement in the opposite direction of the saccade (contraversive). Dashed vertical line indicates time of saccade onset. Trials are sorted by latency of attempted head movements. **(G)** Fraction of trials with ipsiversive attempted head displacements at different time points relative to saccade onset for spontaneous (blue) and evoked (red) saccades. **(H)** Head-eye amplitude coupling of spontaneous (blue) and ear airpuff-evoked saccades (red). Each dot corresponds to a single gaze shift. Attempted head amplitude was measured 150 ms after saccade onset. Spontaneous: $R^2 = 0.60$, slope = 0.221, $p < 10^{-10}$. Evoked: $R^2 = 0.64$, slope = 0.162, $p < 10^{-10}$. Spontaneous and evoked regression slopes were significantly different ($p < 10^{-5}$, permutation test). Histograms above and beside scatter plot indicate distributions of saccade and attempted head movement amplitudes. Difference in means were not significant ($p = 0.46$ for saccades, $p = 0.19$ for head, permutation test). **(I-J)** As in (E-F), but for attempted head movement velocity. **(K)** As in (G), but for attempted head movement velocity. **(L)** As in (H), but for attempted head movement velocity. Peak attempted head velocity was measured 60 ms after saccade onset. Spontaneous: $R^2 = 0.42$, slope = 2.22, $p < 10^{-10}$. Evoked: $R^2 = 0.52$, slope = 1.98, $p < 10^{-10}$. Spontaneous and evoked regression slopes were significantly different ($p < 10^{-5}$, permutation test). Histograms above and beside scatter plot indicate distributions of saccade amplitudes and peak attempted head velocities. Difference in means were not significant ($p = 0.46$ for saccades, $p = 0.09$ for head, permutation test).

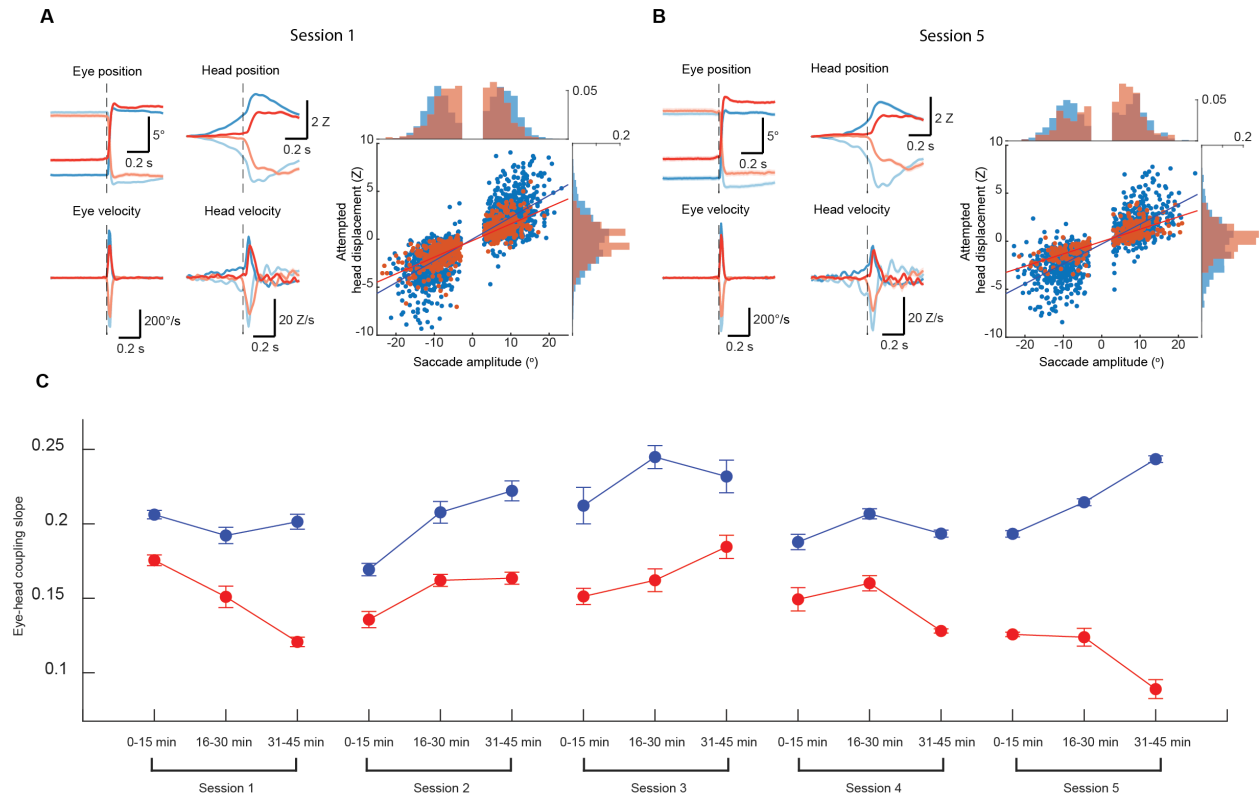


Figure S2.8: Head-eye coupling across and within sessions

(A) Top left, mean trajectories of rightward (solid traces) and leftward (dashed traces) saccades during spontaneous (blue, $n = 1631$) and ear airpuff-evoked (red, $n = 511$) gaze shifts for first session. Top middle, mean attempted head movement amplitudes accompanying rightward (solid traces) and leftward (dashed traces) saccades during spontaneous (blue) and ear airpuff-evoked (red) gaze shifts. Bottom left, mean velocities of all rightward (solid traces) and leftward (dashed traces) saccades during spontaneous (blue) and ear airpuff-evoked (red) gaze shifts for first session. Bottom middle, mean head movement velocities accompanying rightward (solid traces) and leftward (dashed traces) saccades during spontaneous (blue) and ear airpuff-evoked (red) gaze shifts for first session. Right, head-eye amplitude coupling of spontaneous (blue) and ear airpuff-evoked saccades (red) for first session. Each dot corresponds to a single gaze shift. Attempted head movement amplitude was measured 150 ms after saccade onset. Spontaneous: $R^2 = 0.67$, slope = 0.227, $p < 10^{-10}$. Evoked: $R^2 = 0.69$, slope = 0.174, $p < 10^{-10}$. Spontaneous and evoked regression slopes were significantly different ($p < 10^{-5}$, permutation test). Histograms above and beside scatter plot indicate distributions of saccade and attempted head movement amplitudes. Differences in means are significant ($p = 0.012$ for saccades, $p = 0.002$ for head, permutation test). **(B)** Left and middle, as in (A) for spontaneous (blue, $n = 884$) and ear airpuff-evoked (red, $n = 273$) trials from fifth session. Right, head-eye amplitude coupling. Spontaneous: $R^2 = 0.63$, slope = 0.207, $p < 10^{-10}$. Evoked: $R^2 = 0.66$, slope = 0.129, $p < 10^{-10}$. Spontaneous and evoked regression slopes were significantly different ($p < 10^{-5}$, permutation test). **(C)** Eye-head coupling slopes for sessions 1-5 subdivided into three 15-minute epochs.

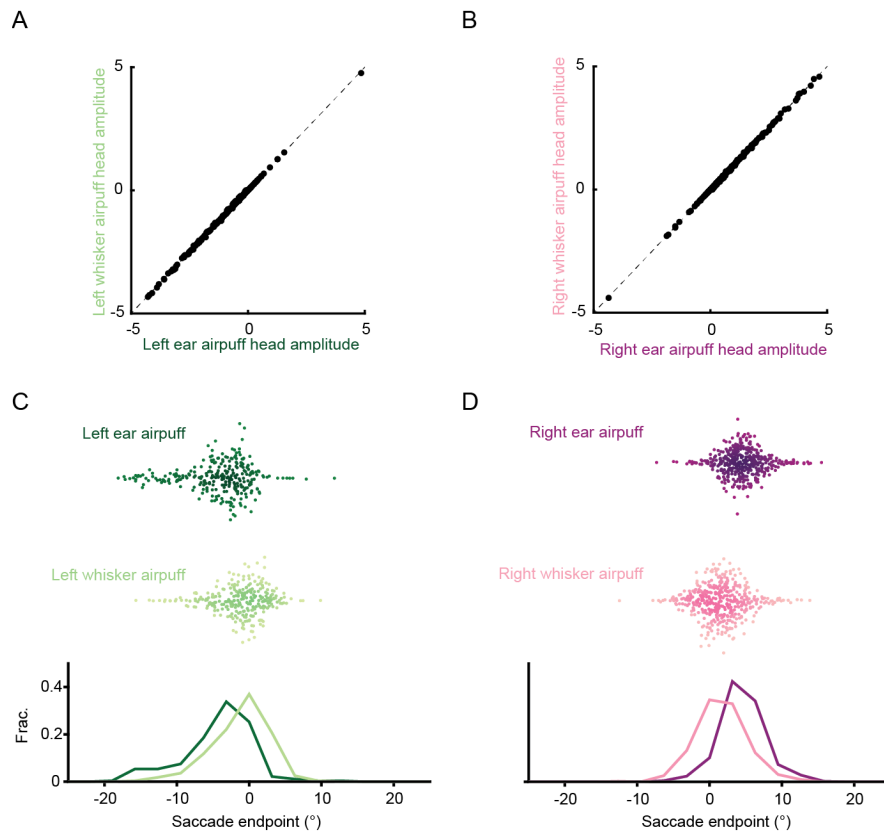


Figure S2.9: Ear- and whisker- airpuff trials matched for attempted head movement amplitude have different saccade endpoints

(A-B) Amplitudes of attempted head movements for matched trials. Left ear airpuff trials were matched with left whisker airpuff trials (A, $n = 281$ trials per stimulus condition), and right ear airpuff trials were matched with right whisker airpuff trials (B, $n = 424$ trials per stimulus condition). Each point denotes the attempted head movement amplitudes of an amplitude-matched pair of trials from the two datasets. Dashed line denotes unity line. (C-D) Distributions of saccade endpoints for matched trials shown in A and B.

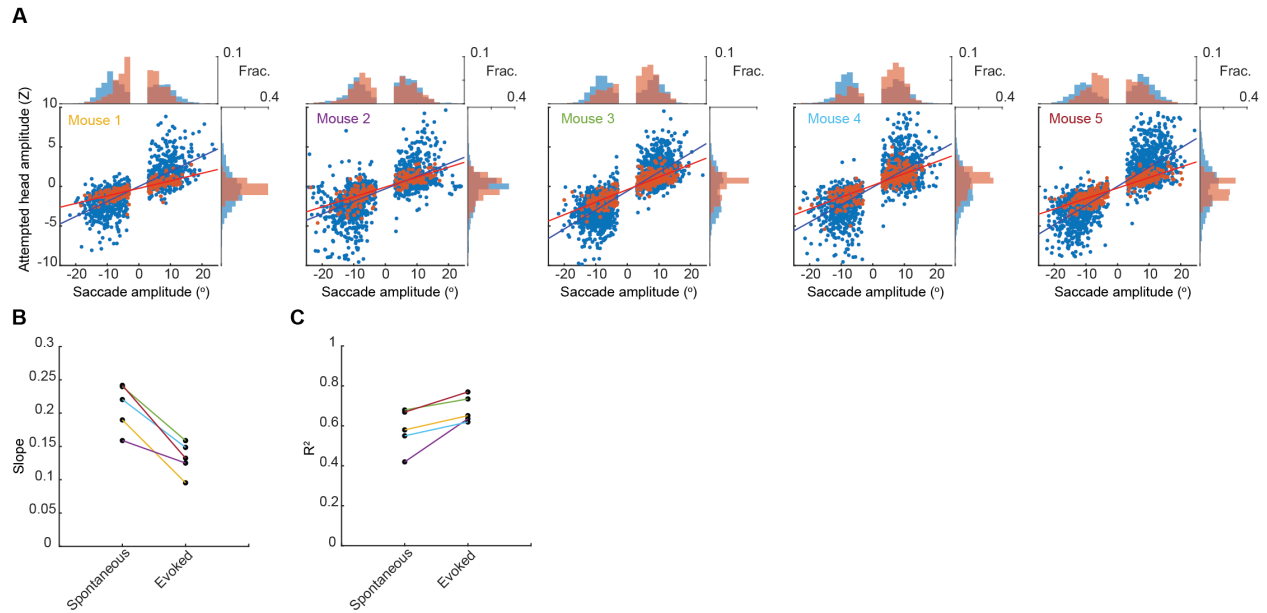


Figure S2.10: Gain of head-eye coupling variability across mice

(A) Head-eye amplitude coupling of spontaneous (blue) and ear airpuff-evoked saccades (red) for five individual mice. Each dot corresponds to a single gaze shift. The spontaneous and evoked regression slopes were significantly different for all mice ($p < 10^{-5}$, permutation test). Histograms above and beside scatter plot indicate distributions of saccade and attempted head movement amplitudes. (B, C) Slope and R^2 for linear fits to spontaneous and evoked gaze shifts for each mouse. Colored lines indicate values for the different mice in A.

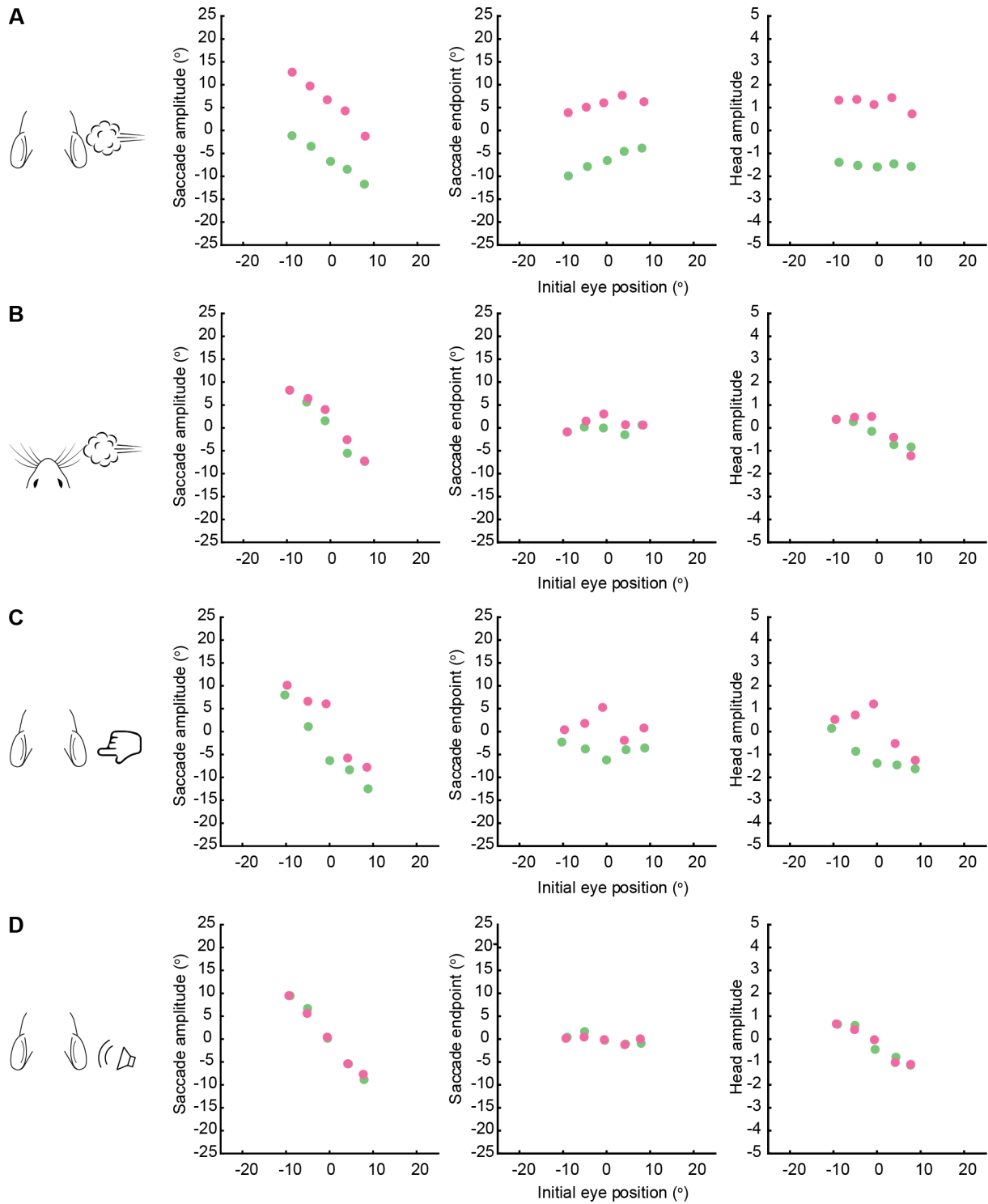


Figure S2.11: Saccade amplitude, saccade endpoint, and attempted head movement amplitude binned by initial eye position

(A) Left, mean saccade amplitudes binned by initial eye position for ear airpuff. Middle, mean saccade endpoints binned by initial eye position. Right, mean attempted head amplitude binned by initial eye position. (B) As in (A) for whisker airpuff. (C) As in (A) for ear tactile. (D) As in (A) for auditory airpuff.

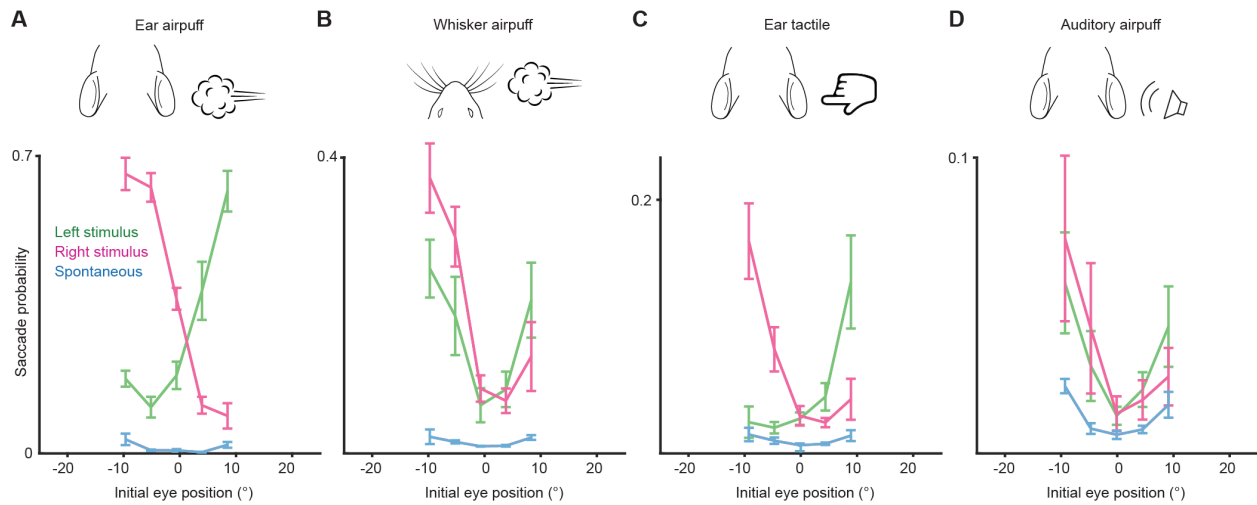


Figure S2.12: Relationship between initial eye position and saccade probability
 Green and magenta lines indicate population means ($n = 5$ mice) for saccades evoked by left and right stimuli, respectively. Blue lines indicate spontaneous saccades. Error bars indicate s.e.m. Saccade numbers: ear airpuff sessions, spontaneous = 7146, left ear airpuff-evoked = 942, right ear airpuff-evoked = 1213; whisker airpuff sessions: spontaneous = 7790, left whisker airpuff-evoked = 440, right whisker airpuff-evoked = 606; ear tactile sessions, spontaneous = 6706, left ear tactile-evoked = 133, right ear tactile-evoked = 186; auditory sessions, spontaneous = 10240, left auditory-evoked = 140, right auditory-evoked = 158.

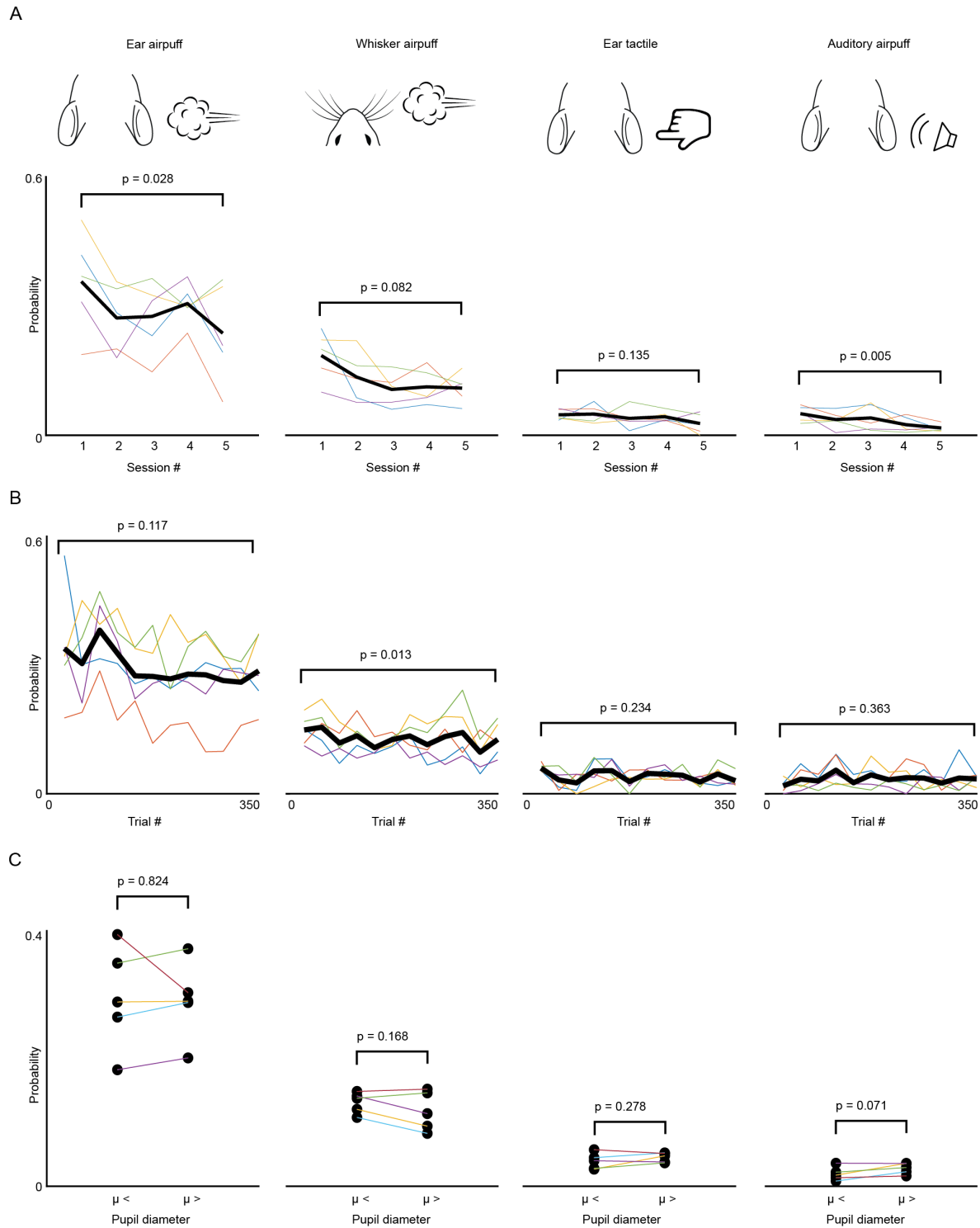


Figure S2.13: Effects of sensory history and arousal on saccade generation
(A) Overall gaze shift probability across 5 sessions for ear airpuffs, whisker airpuffs, ear tactile, and auditory airpuffs stimuli. Each thin colored line corresponds to an individual mouse. Black line corresponds to mean **(B)** As in (A) but for gaze shift probability within sessions. **(C)** Effects of arousal on saccade probability. μ denotes mean pupil diameter. Statistical significance assessed using paired Student's t-test.

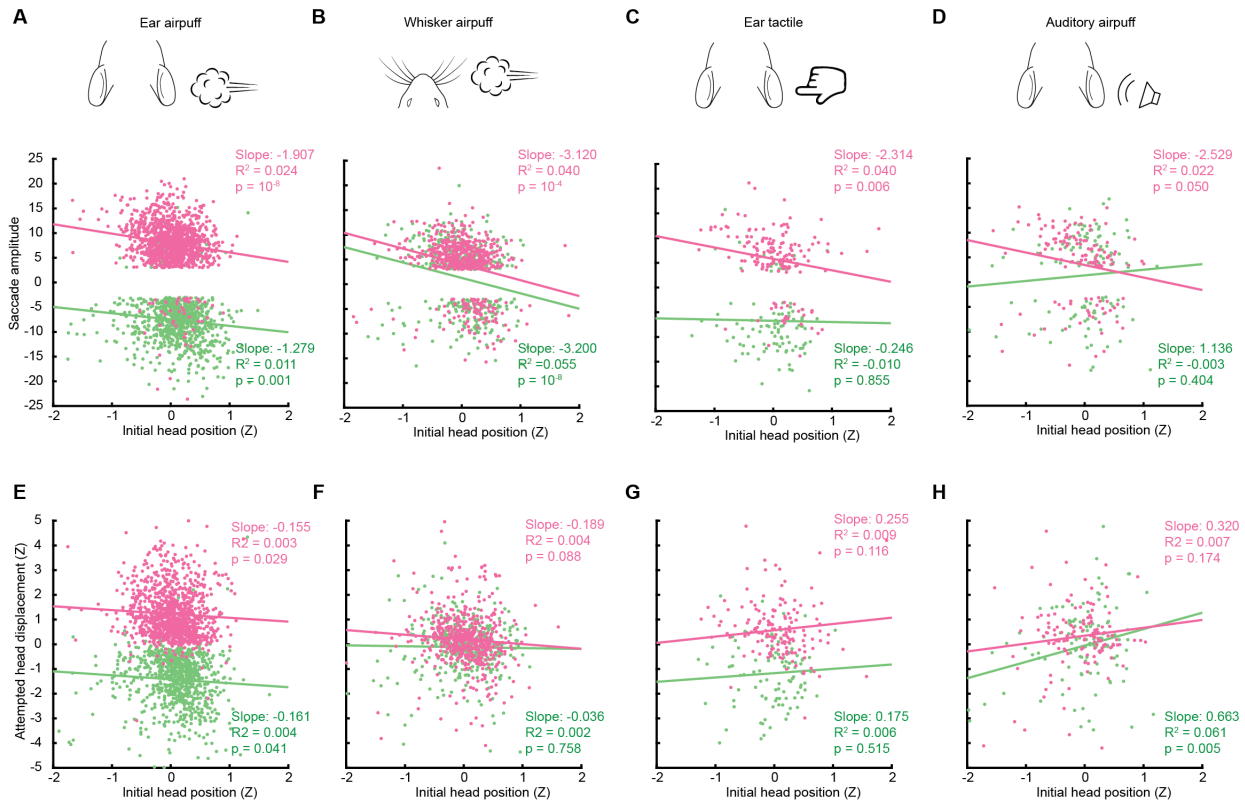


Figure S2.14: Relationship between initial head position and saccade and head movement amplitude

(A-D) Relationship between saccade amplitude and initial head position for ear airpuffs (A), whisker airpuffs (B), whisker tactile (C), and auditory airpuffs (D). (E-H) Relationship between saccade amplitude and initial head position for ear airpuffs (E), whisker airpuffs (F), whisker tactile (G), and auditory airpuffs (H). Only trials in which animals maintained a stable head position in the 500 ms preceding stimulus onset were analyzed. Total trial numbers for A-H: ear airpuff sessions, left ear airpuff = 862, right ear airpuff = 1140; whisker airpuff sessions, left whisker airpuff = 380, right whisker airpuff = 537; tactile ear sessions, left tactile ear = 103, right tactile ear; = 159; auditory airpuff, left auditory airpuff = 112, right auditory airpuff = 132. R^2 values for initial eye position vs. saccade amplitude and initial eye position vs. head movement amplitude for identical trials were similar to those listed in Figure 2.5A-H.

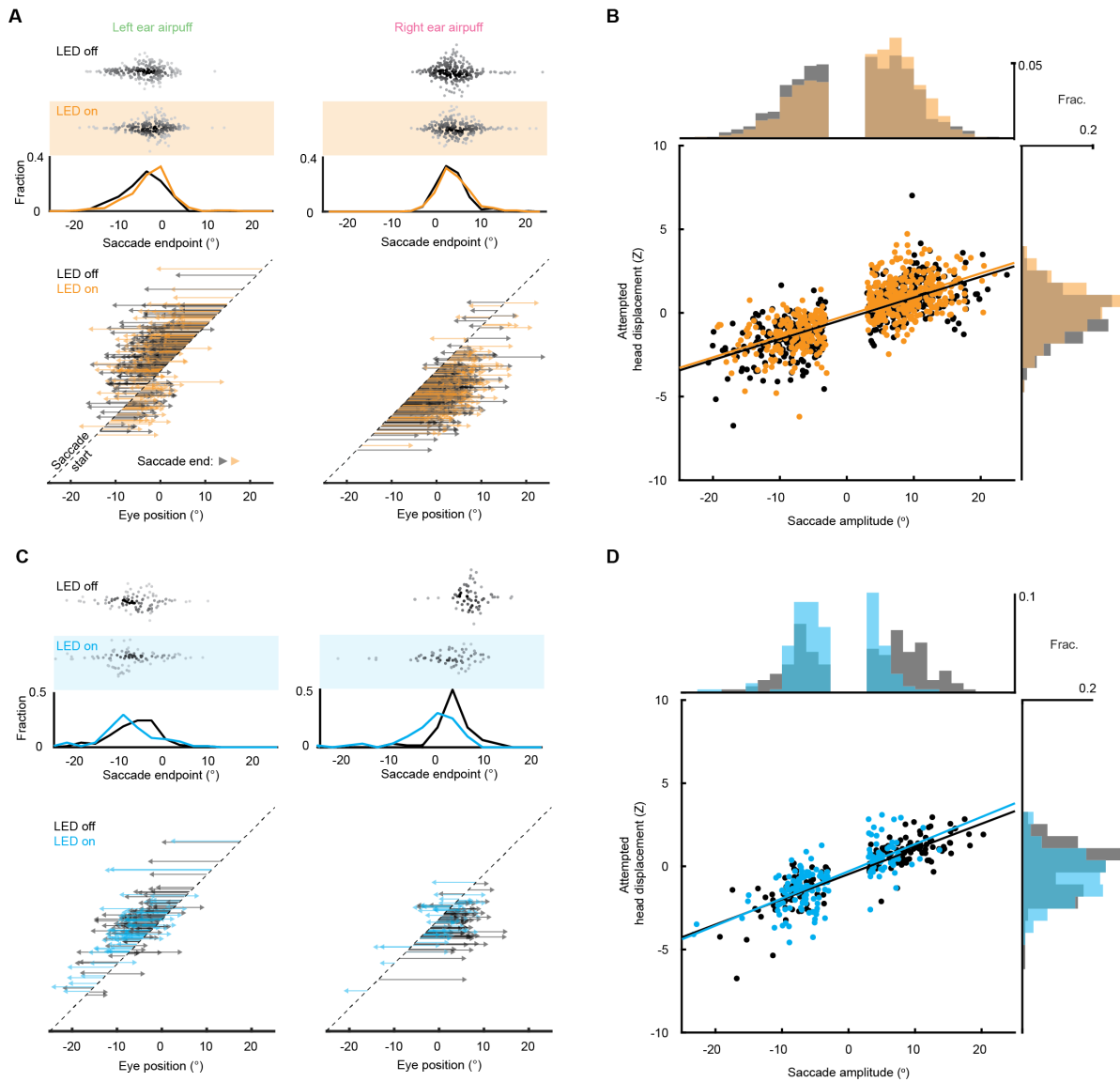


Figure S2.15: Controlling for the effects of initial eye position on superior colliculus manipulations

(A) Effects of SC optogenetic inhibition on saccade endpoints for trials matched for initial eye position. Top, scatter plots and histograms of endpoints for control (white background) and LED on (orange background) trials. Middle, endpoint histograms for control (black) and LED on (orange) trials. Bottom, saccade vectors for control (black) and LED on (orange) trials. **(B)** Head-eye amplitude coupling during ear airpuff-evoked gaze shifts for control (black) and LED on (orange) trials matched for initial eye position. Each dot represents an individual gaze shift. Control: $R^2 = 0.57$, slope = 0.124, $p < 10^{-10}$. LED on: $R^2 = 0.53$, slope = 0.125, $p < 10^{-10}$. Control and LED-on regression slopes were not significantly different ($p = 0.41$, permutation test). Histograms above and beside scatter plot show distributions of saccade amplitude and head displacement, respectively. Distribution means were significantly different ($p = 0.002$ for saccades, $p <$

(legend continued on next page)

(legend continued from previous page)

10^{-5} for attempted head movements, permutation test). **(C)** Effects of weak SC optogenetic stimulation on saccade endpoints for trials matched for initial eye position. Top, scatter plots and histograms of endpoints for control (white background) and LED on (blue background) trials. Middle, histograms of endpoints for control (black) and LED on (blue) trials. Bottom, saccade vectors for control (black) and LED on (blue) trials. **(D)** Head-eye amplitude coupling during ear airpuff-evoked gaze shifts for control (black) and LED on (blue) trials matched for initial eye position. Each dot represents an individual gaze shift. Control: $R^2 = 0.74$, slope = 0.15, $p < 10^{-10}$. LED on: $R^2 = 0.52$, slope = 0.164, $p < 10^{-10}$. Control and LED-on regression slopes were not significantly different ($p = 0.35$, permutation test) Histograms above and beside scatter plot show distributions of saccade amplitude and head displacement, respectively. Means were significantly different ($p < 10^{-5}$ for saccades, $p = 0.002$ for attempted head movements, permutation test).

2.8 REFERENCES

- Ahmadlou, M., and Heimel, J.A. (2015). Preference for concentric orientations in the mouse superior colliculus. *Nat. Commun.* 6, 1–11.
- Allen, P.D., and Ison, J.R. (2010). Sensitivity of the mouse to changes in azimuthal sound location: Angular separation, spectral composition, and sound level. *Behav. Neurosci.* 124, 265.
- Baden, T., Schubert, T., Chang, L., Wei, T., Zaichuk, M., Wissinger, B., and Euler, T. (2013). A tale of two retinal domains: Near-Optimal sampling of achromatic contrasts in natural scenes through asymmetric photoreceptor distribution. *Neuron* 80, 1206–1217.
- Bahill, A.T., Clark, M.R., and Stark, L. (1975). The main sequence, a tool for studying human eye movements. *Math. Biosci.* 24, 191–204.
- Basso, M.A., and May, P.J. (2017). *Circuits for Action and Cognition: A View from the Superior Colliculus.*
- van Beest, E.H., Mukherjee, S., Kirchberger, L., Schnabel, U.H., van der Togt, C., Teeuwen, R.R.M., Barsegyan, A., Meyer, A.F., Poort, J., Roelfsema, P.R., et al. (2021). Mouse visual cortex contains a region of enhanced spatial resolution. *Nat. Commun.* 2021 121 12, 1–17.
- Bizzi, E., Kalil, R., and Tagliasco, V. (1971). Eye-head coordination in monkeys: evidence for centrally patterned organization. *Science* 173, 452–454.

- Bizzi, E., Kalil, R.E., and Morasso, P. (1972). Two modes of active eye-head coordination in monkeys. *Brain Res.* 40, 45–48.
- Bleckert, A., Schwartz, G.W., Turner, M.H., Rieke, F., and Wong, R.O.L. (2014). Visual space is represented by nonmatching topographies of distinct mouse retinal ganglion cell types. *Curr. Biol.* 24, 310–315.
- Curthoys, I.S. (2002). Generation of the quick phase of horizontal vestibular nystagmus. *Exp. Brain Res.* 2002 1434 143, 397–405.
- Diamond, M.E., von Heimendahl, M., Knutsen, P.M., Kleinfeld, D., and Ahissar, E. (2008). “Where” and “what” in the whisker sensorimotor system. *Nat. Rev. Neurosci.* 2008 98 9, 601–612.
- Drager, U.C., and Hubel, D.H. (1975). Responses to visual stimulation and relationship between visual, auditory, and somatosensory inputs in mouse superior colliculus. *J. Neurophysiol.* 38, 690–713.
- Drager, U.C., and Hubel, D.H. (1976). Topography of visual and somatosensory projections to mouse superior colliculus. *J. Neurophysiol.* 39, 91-101.
- Feinberg, E.H., and Meister, M. (2015). Orientation columns in the mouse superior colliculus. *Nature* 519, 229–232.
- Freedman, E.G. (2008). Coordination of the Eyes and Head during Visual Orienting. *Exp. Brain Res.* 190, 369.
- Freedman, E., and Sparks, D. (1997). Eye-head coordination during head-unrestrained gaze shifts in rhesus monkeys. *J. Neurophysiol.* 77, 2328–2348.

- Freedman, E., Stanford, T., and Sparks, D. (1996). Combined eye-head gaze shifts produced by electrical stimulation of the superior colliculus in rhesus monkeys. *J. Neurophysiol.* 76, 927–952.
- Gandhi, N.J., and Katnani, H.A. (2011). Motor Functions of the Superior Colliculus. *Annu. Rev. Neurosci.* 34, 205–231.
- Goldring, J.E., Dorris, M.C., Corneil, B.D., Ballantyne, P., and Munoz, D. (1996). Combined eye-head gaze shifts to visual and auditory targets in humans (Springer-Verlag).
- Gómez-Nieto, R., Hormigo, S., and López, D.E. (2020). Prepulse Inhibition of the Auditory Startle Reflex Assessment as a Hallmark of Brainstem Sensorimotor Gating Mechanisms. *Brain Sci.* 10, 1–15.
- Gradinaru, V., Zhang, F., Ramakrishnan, C., Mattis, J., Prakash, R., Diester, I., Goshen, I., Thompson, K.R., and Deisseroth, K. (2010). Molecular and Cellular Approaches for Diversifying and Extending Optogenetics. *Cell* 141, 154–165.
- Groh, J.M., and Sparks, D.L. (1996). Saccades to somatosensory targets. III. eye-position-dependent somatosensory activity in primate superior colliculus. *J. Neurophysiol.* 75, 439–453.
- Gui-ton, D. (1992). Control of eye-head coordination during orienting gaze shifts. *Trends Neurosci.* 15, 174–179.

- Guittton, D., Crommelinck, M., and Roucoux, A. (1980). Stimulation of the superior colliculus in the alert cat. I. Eye movements and neck EMG activity evoked when the head is restrained. *Exp. Brain Res.* 39, 63–73.
- Guittton, D., Douglas, R.M., and Volle, M. (1984). Eye-Head Coordination in Cats. *J. Neurophysiol.* 52.
- Hepp, K., Opstal, A.J. Van, Straumann, D., Hess, B.J., and Henn, V. (1993). Monkey superior colliculus represents rapid eye movements in a two-dimensional motor map. <https://doi.org/10.1152/Jn.1993.69.3.965> 69, 965–979.
- Hikosaka, O., and Wurtz, R.H. (1985). Modification of saccadic eye movements by GABA-related substances. I. Effect of muscimol and bicuculline in monkey superior colliculus. *J. Neurophysiol.* 53, 266–291.
- Ito, T., Hasegawa, M., Kimura, R., Osaki, H., Albrecht, U.R., Sohya, K., Chakrabarti, S., Itoh, H., Ito, T., Sato, T.K., et al. (2018). Streamlined sensory motor communication through cortical reciprocal connectivity in a visually guided eye movement task. *Nat. Commun.* 9, 1–14.
- Jay, M.F., and Sparks, D.L. (1984). Auditory receptive fields in primate superior colliculus shift with changes in eye position. *Nature* 309, 345–347.
- Kitama, T., Ohki, Y., Shimazu, H., Tanaka, M., and Yoshida, K. (1995). Site of interaction between saccade signals and vestibular signals induced by head rotation in the alert cat: functional properties and afferent organization of burster-driving neurons. *J. Neurophysiol.* 74, 273–287.

- Land, M.F. (2019). The Evolution of Gaze Shifting Eye Movements. In *Current Topics in Behavioral Neurosciences*, (Springer), pp. 3–11.
- Land, M.F., and Nilsson, D.-E. (2012). *Animal Eyes* (Oxford University Press).
- Lee, C. (1999). Eye and head coordination in reading: roles of head movement and cognitive control. *Vision Res.* 39, 3761–3768.
- Li, Y. tang, Turan, Z., and Meister, M. (2020). Functional Architecture of Motion Direction in the Mouse Superior Colliculus. *Curr. Biol.* 30, 3304–3315.
- Liversedge, S.P., Gilchrist, I.D., and Everling, S. (2011). *The Oxford Handbook of Eye Movements* (Oxford University Press).
- de Malmazet, D., Kühn, N.K., and Farrow, K. (2018). Retinotopic Separation of Nasal and Temporal Motion Selectivity in the Mouse Superior Colliculus. *Curr. Biol.* 28, 2961-2969.e4.
- Masullo, L., Mariotti, L., Alexandre, N., Freire-Pritchett, P., Boulanger, J., and Tripodi, M. (2019). Genetically Defined Functional Modules for Spatial Orienting in the Mouse Superior Colliculus. *Curr. Biol.* 29.
- May, P.J. (2006). The mammalian superior colliculus: laminar structure and connections. *Prog. Brain Res.* 151.
- Meyer, A.F., Poort, J., O’Keefe, J., Sahani, M., and Linden, J.F. (2018). A Head-Mounted Camera System Integrates Detailed Behavioral Monitoring with Multichannel Electrophysiology in Freely Moving Mice. *Neuron* 100, 46-60.e7.

- Meyer, A.F., O'Keefe, J., and Poort, J. (2020). Two Distinct Types of Eye-Head Coupling in Freely Moving Mice. *Curr. Biol.* 30, 2116-2130.e6.
- Michaël, A.M., Abe, E.T.T., and Niell, C.M. (2020). Dynamics of gaze control during prey capture in freely moving mice. *Elife* 9, 1–27.
- Paré, M., and Munoz, D.P. (2001). Expression of a re-centering bias in saccade regulation by superior colliculus neurons. *Exp. Brain Res.*
- Paré, M., Crommelinck, M., and Guitton, D. (1994). Gaze shifts evoked by stimulation of the superior colliculus in the head-free cat conform to the motor map but also depend on stimulus strength and fixation activity. *Exp. Brain Res.* 101, 123–139.
- Payne, H.L., and Raymond, J.L. (2017). Magnetic eye tracking in mice. *Elife* 6.
- Pelisson, D., and Guillaume, A. (2009). Eye-Head Coordination. *Encycl. Neurosci.* 1545–1548.
- Populin, L.C. (2006). Monkey Sound Localization: Head-Restrained versus Head-Unrestrained Orienting. *J. Neurosci.* 26, 9820–9832.
- Populin, L.C., and Rajala, A.Z. (2011). Target modality determines eye-head coordination in nonhuman primates: Implications for gaze control. *J. Neurophysiol.* 106, 2000–2011.
- Populin, L.C., Tollin, D.J., and Yin, T.C.T. (2004a). Effect of Eye Position on Saccades and Neuronal Responses to Acoustic Stimuli in the Superior Colliculus of the Behaving Cat. *J. Neurophysiol.* 92, 2151–2167.

- Populin, L.C., Tollin, D.J., and Yin, T.C.T. (2004b). Effect of eye position on saccades and neuronal responses to acoustic stimuli in the superior colliculus of the behaving cat. *J. Neurophysiol.* 92, 2151–2167.
- Reimer, J., Froudarakis, E., Cadwell, C.R., Yatsenko, D., Denfield, G.H., and Tolias, A.S. (2014). Pupil Fluctuations Track Fast Switching of Cortical States during Quiet Wakefulness. *Neuron* 84, 355–362.
- Robinson, D.A. (1972). Eye movements evoked by collicular stimulation in the alert monkey. *Vision Res.* 12, 1795–1808.
- Ruhland, J.L., Yin, T.C.T., and Tollin, D.J. (2013). Gaze shifts to auditory and visual stimuli in cats. *JARO - J. Assoc. Res. Otolaryngol.* 14, 731–755.
- Samonds, J.M., Geisler, W.S., and Priebe, N.J. (2018). Natural image and receptive field statistics predict saccade sizes. *Nat. Neurosci.* 21, 1591–1599.
- Schiller, P.H., and Stryker, M. (1972). Single-unit recording and stimulation in superior colliculus of the alert rhesus monkey. *J. Neurophysiol.* 35, 915–924.
- Sparks, D.L. (1986). Translation of sensory signals into commands for control of saccadic eye movements: role of primate superior colliculus. *Physiol Rev.* 66, 118–171.
- Sparks, D.L. (2002). The brainstem control of saccadic eye movements. *Nat. Rev. Neurosci.* 3, 952–964.

- Tatler, B.W. (2007). The central fixation bias in scene viewing: Selecting an optimal viewing position independently of motor biases and image feature distributions. *J. Vis.* 7, 4.
- Tollin, D.J., Populin, L.C., Moore, J., Ruhland, J.L., and Yin, T.C.T. (2005). Sound-localization performance in the cat: the effect of restraining the head. *J. Neurophysiol.* 93, 1223–1234.
- Wallace, D.J., Greenberg, D.S., Sawinski, J., Rulla, S., Notaro, G., and Kerr, J.N.D. (2013). Rats maintain an overhead binocular field at the expense of constant fusion. *Nature* 498, 65–69.
- Walls, G.L. (1962). The evolutionary history of eye movements. *Vision Res.* 2, 69–80.
- Wang, L., Liu, M., Segraves, M.A., and Cang, J. (2015). Visual experience is required for the development of eye movement maps in the mouse superior colliculus. *J. Neurosci.* 35, 12281–12286.
- Zangemeister, W.H., and Stark, L. (1982). Types of gaze movement: Variable interactions of eye and head movements. *Exp. Neurol.* 77, 563–577.

Chapter 3: Hindbrain modules differentially transform activity of single collicular neurons to coordinate movements

3.1 ABSTRACT

Seemingly simple behaviors such as swatting a mosquito or glancing at a signpost involve the precise coordination of multiple body parts. Neural control of coordinated movements is widely thought to entail transforming a desired overall displacement into displacements for each body part. Here we reveal a different logic implemented in the mouse gaze system. Stimulating superior colliculus (SC) elicits head movements with stereotyped displacements but eye movements with stereotyped endpoints. This is achieved by individual SC neurons whose branched axons innervate modules in medulla and pons that drive head movements with stereotyped displacements and eye movements with stereotyped endpoints, respectively. Thus, single neurons specify a mixture of endpoints and displacements for different body parts, not overall displacement, with displacements for different body parts computed at distinct anatomical stages. Our study establishes an approach for unraveling motor hierarchies and identifies a logic for coordinating movements and the resulting pose.

3.2 INTRODUCTION

Most behaviors involve moving multiple body parts. For example, plucking a ripe berry from a bush involves shoulder, elbow, and finger movements, and turning to identify the friend calling your name involves head and eye movements. Each body part has its own range of motion and movement axes and can be positioned independently of the others. As a result, each body part may travel a different direction and distance (i.e., displacement) during a coordinated movement. How, then, does the brain determine the displacements for individual body parts to generate a coordinated movement?

It is widely believed that the brain achieves such coordination through a hierarchical series of computations implemented within an anatomical hierarchy. In this view, neurons atop the hierarchy (i.e., further removed from the motor command) specify higher-level parameters such as the overall desired displacement, whereas neurons at lower levels decompose these higher-level parameters into the necessary displacements for each body part (Kandel et al., 2013; Kawato, 1999; Miall and Wolpert, 1996; Wolpert et al., 1998), e.g., the shoulder, elbow, and finger displacements needed to pick a berry. Consistent with this model, stimulation of brain areas or genetically defined cell types atop the anatomical hierarchy can evoke coordinated movements wherein multiple body parts move different distances (e.g., grooming, rearing, or bringing the hand to the mouth as though eating), whereas stimulation of neurons at the bottom of the anatomical hierarchy can evoke stereotyped movement displacements of a particular body part (e.g., contraction of a muscle group by a defined amount) (Bizzi et al., 1995; D'Avella et al., 2003; Ferreira-Pinto et al., 2021; Graziano and Aflalo, 2007;

Graziano et al., 2002; Overduin et al., 2012; Ruder and Arber, 2019; Ruder et al., 2021; Wang et al., 2017). However, little is known about where, and how this hierarchical series of computations is instantiated within these anatomical hierarchies (Diedrichsen et al., 2010; Merel et al., 2019; Todorov and Jordan, 2002). In addition, these hierarchical frameworks have been studied primarily in the context of volitional behaviors such as trained reaching, but animals coordinate multiple body parts during innate, reflexive behaviors such as grooming, gaze shifts, avoidance, consummatory, and escape as well (Guo et al., 2015; Isa et al., 2021; Park et al., 2020; Ruder and Arber, 2019; Shang et al., 2019a; Shenoy et al., 2013; Xie et al., 2022). Whether the computations hypothesized to underlie volitional behaviors apply to all coordinated movements is unknown.

Resolving where and how motor hierarchies in the brain transform higher-order movement plans into specific commands for individual body parts will require a stepwise, systematic interrogation of these circuits. Many studies have postulated that upper motor neurons in regions such as motor cortex and superior colliculus (SC) are key players in this process. Upper motor neurons connect higher centers to controllers in brainstem and spinal cord, and the axons of single upper motor neurons often collateralize to innervate multiple target areas (Arber and Costa, 2022; Grantyn et al., 2004; Hooks et al., 2018; Isa et al., 2020, 2021; Keizer and Kuypers, 1989; Kita and Kita, 2012; Komiyama et al., 2010; Lemon, 2008; Masullo et al., 2019; Nelson et al., 2021; Takahashi et al., 2005; Ugolini and Kuypers, 1986; Wang et al., 2017). These anatomical data suggest a mechanism whereby individual upper motor neurons carry signals used to coordinate multiple body parts (Arber and Costa, 2022). For example, in

the gaze system, it is widely believed that the higher-order parameter specified by upper motor neurons in SC is overall gaze displacement (i.e., the sum of how far the head and eyes will move) (Bergeron et al., 2003; Freedman, 2008; Guitton, 1992; Sajad et al., 2020). It is debated, however, where and how the desired overall displacement is transformed into the component head and eye displacements (Bergeron et al., 2003; Freedman, 2008; Sajad et al., 2020).

Here, we use a suite of approaches to dissect the motor hierarchy controlling a complex reflexive behavior, gaze shifts, in the genetically tractable mouse. Our initial experiments unexpectedly revealed that single mouse SC upper motor neurons do not specify the overall gaze displacement. Instead, their activity specifies the displacement for the head but only the endpoint for the eyes. In this sense, SC neurons multiplex displacements and endpoints for different body parts. Subsequent analyses found that single SC upper motor neurons innervate two separate hindbrain populations that drive head movements with fixed displacements and eye movements with fixed endpoints, respectively. Neural recordings showed that head displacement information emerges in SC, whereas saccade information does not emerge until the hindbrain. Our study thus reveals that overall displacements are not computed at any single anatomical stage within the mouse gaze hierarchy, and that displacements for different body parts are computed independently and at distinct anatomical stages, thereby uncovering unexpected diversity in mechanisms of coordinated movements.

3.3 RESULTS

Mouse SC specifies head movement displacement and saccade endpoint but not overall gaze displacement

The gaze system is a popular paradigm for investigating movement coordination because it involves relatively few degrees of freedom and a compact neuroanatomical hierarchy (Bizzi et al., 1971; Freedman, 2008; Gandhi and Katnani, 2011; Guitton, 1992; Land, 2019; Paré et al., 1994; Sajad et al., 2020). In particular, superior colliculus (SC) controls orienting head and eye movements in a wide range of species, including mice, and stimulating SC elicits head and eye movements resembling those observed during sensory-guided gaze shifts (Bizzi et al., 1972; Isa et al., 2021; Masullo et al., 2019; Schiller and Stryker, 1972; Zahler et al., 2021). Therefore, we decided to investigate how mouse SC coordinates movements of the head and the eyes.

We investigated head and eye movements driven by optogenetic stimulation of right SC in freely moving animals, focusing on the horizontal axis, in which movements were largest (Figure 3.1A-C, Figure S3.1A-E) (Meyer et al., 2018, 2020; Michael et al., 2020; Wallace et al., 2013). In primates and cats, it is believed that SC issues a gaze displacement command because stimulation of a single site elicits the same overall gaze displacement (i.e., angular displacement) regardless of initial gaze direction (Sajad et al., 2020). To determine whether this is the case in mice, we examined the relationship between initial gaze direction and SC-evoked gaze displacement. In contrast to what was observed in cats and primates, SC stimulation in mice evoked gaze shifts whose displacements depended on initial gaze direction (Figure 3.1D, E, H, I). To further investigate this finding, we examined the dependence of SC-evoked gaze

shifts on initial eye and head position. Gaze displacement showed no dependence on initial head position but a strong dependence on initial eye position (Figure 3.1F-I). Together, these data suggest that mouse SC does not issue a fixed gaze displacement command.

We next examined the head and eye components of these SC-evoked movements separately to determine the basis for the eye position-dependence of overall gaze displacements (Figure 3.1J-U). Consistent with a previous report, SC-evoked head movements had stereotyped displacements, i.e. leftward (contraversive) head movements that showed little dependence on initial head-body angle (Figure 3.1J, L, N, O) (Masullo et al., 2019). Moreover, head displacements were nearly invariant with respect to the initial orbital positions of the eyes (Figure 3.1J-O, Figure S3.1J, K). We next examined the rapid eye movements (saccades) elicited by SC stimulation. Surprisingly, SC stimulation evoked saccades whose displacements were highly variable but whose endpoints were stereotyped (Figure 3.1P). This unexpected variability in saccade displacements was largely explained by initial eye position relative to the saccade endpoint (Figure 3.1S-U, Figure 3.1SJ, K). Interestingly, saccade probability showed a similar dependence on initial eye position such that saccades were likeliest when the eyes began far from the endpoint (Figure S3.1F, L, M). In contrast, initial head-body angle had little impact on saccade displacement (Figure 3.1R, T, U; Figure S3.1G). Thus, mouse SC drives head movements with stereotyped displacements and saccades with stereotyped endpoints, such that SC-evoked gaze displacement varies according to the initial position of the eyes.

To confirm that these differences in SC-evoked head and eye movements were not due to the mechanical properties of the mouse oculomotor system, e.g., the elasticity of the extraocular muscles, we optogenetically activated abducens motor neurons, which innervate the extraocular muscle (lateral rectus) that rotates the eye away from center, in *ChAT-Cre* transgenic mice (Figure S3.1N, O) (Rossi et al., 2011; Stahl et al., 2015). Abducens stimulation caused movements of the ipsilateral eye that were invariant to initial eye position, i.e., with stereotyped displacements, indicating that the effects of SC stimulation cannot be explained by the mechanical properties of the eye (Figure S3.1P-U).

Mouse SC comprises topographic maps of head movement displacement and saccade endpoint

Using single-site stimulation in freely moving mice, we found that mouse SC encodes head displacement and eye endpoint rather than overall gaze displacement. Previous studies in mice demonstrated that SC-evoked head and eye movements depend on the site of stimulation within SC (Masullo et al., 2019; Wang et al., 2015). However, these studies did not examine the effects of initial eye position and therefore could not determine what gaze parameters were represented topographically within this map. We therefore sought to better understand how head and eye movements depend on the site of SC stimulation. To facilitate comparisons with existing literature and to isolate SC-mediated eye movements from compensatory eye movements resulting from the vestibular ocular reflex (VOR), we performed electrical microstimulation at different sites within SC of head-fixed mice while monitoring the eyes and attempted head

rotations (Figure 3.2A, Figure S3.2A, B) (Meyer et al., 2020; Wang et al., 2015; Zahler et al., 2021).

Consistent with previous studies, we found that stimulating right SC evoked exclusively leftward (contraversive) attempted head movements that were larger for more posterior stimulation sites (Figure 3.2B, D, Figure S3.2G-H) (head displacement, shanks 1-4: -0.98 ± 0.42 Z, -1.42 ± 0.39 Z, -1.86 ± 0.39 Z, -2.20 ± 0.43 Z [mean \pm s.d.]; $R^2 = 0.56$, $p < 10^{-6}$, $n = 9$ mice, linear regression). In addition, attempted head displacements were invariant to initial eye position, consistent with our findings in freely moving animals (Figure 3.2G, Figure S3.2C, D). Next, we analyzed SC-evoked saccades (Figure 3.2C). In contrast to head movements, saccade displacements did not depend on the site of stimulation (Figure 3.2E) (saccade displacements, shanks 1-4: $-6.9 \pm 3.3^\circ$, $-7.1 \pm 2.1^\circ$, $-8.4 \pm 2.2^\circ$, $-8.2 \pm 2.3^\circ$ [mean \pm s.d.]; $R^2 = 0.05$, $p = 0.18$, $n = 9$ mice, linear regression). Strikingly, however, saccade endpoints depended on the site of stimulation, becoming more contralateral for more posterior stimulation sites (saccade endpoints, shanks 1-4: $-1.8 \pm 2.0^\circ$, $-3.1 \pm 2.0^\circ$, $-5.6 \pm 1.7^\circ$, $-6.0 \pm 2.7^\circ$ [mean \pm s.d.]; $R^2 = 0.37$, $p < 10^{-4}$, $n = 9$ mice, linear regression) (Figure 3.2C, F). As in freely moving mice, saccade endpoints were more stereotyped because of the strong dependence of saccade displacement and probability on initial eye position (Figure 3.2G, H, Figure S3.2E-J).

To more directly test the hypothesis that SC specifies saccade endpoints rather than displacements, we trained multinomial logistic regression classifiers to ask whether the site of stimulation in SC is better predicted by saccade displacements or endpoints (Figure 3.2I, J). Classifier performance using saccade endpoints was well above chance

(0.37 ± 0.08 vs. 0.25 ; $p = 0.005$, $n = 9$ mice, one-sample Student's t-test), whereas classifier performance using saccade displacements was not significantly better than chance (0.26 ± 0.03 vs. 0.25 ; $p = 0.09$, $n = 9$ mice, one-sample Student's t-test) and significantly worse than performance using saccade endpoint ($p = 0.004$, two-sample Student's t-test). Together, these data indicate that mouse SC contains superimposed maps of head movement displacements and saccade endpoints, not overall gaze displacement. In addition, these findings validated use of the head-fixed fictive preparation for subsequent experiments because of its ability to isolate SC-mediated saccadic eye movements from non-SC-mediated slow VOR eye movements (Figure 3.1P, Figure 3.2C) while preserving the relationship between SC-mediated head movements and saccades observed in freely moving mice.

Tectoreticular neurons specify head displacement and saccade endpoint

We next sought to identify the SC cells that drive these coordinated movements. Previous studies have implicated a population of SC upper motor neurons known as tectoreticular neurons in both head and saccadic eye movements (Isa et al., 2021; Masullo et al., 2019; Moschovakis et al., 1988a). In rodents, tectoreticular neurons are especially abundant in lateral deep SC, and bulk-labeled tectoreticular axons innervate multiple target sites in the contralateral ponto-medullary reticular formation (PMRF) (Isa et al., 2020; Masullo et al., 2019). To determine whether tectoreticular neurons drive coordinated head and eye movements in mice, we optogenetically stimulated SC axons in proximal contralateral PMRF of head-fixed mice, reasoning that because ChR2 can be used to drive both axon terminals and fibers of passage, this would excite axons arborizing within proximal PMRF as well as axons targeting more distal areas (Figure

3.3A) (Redgrave et al., 1987; Yizhar et al., 2011). Indeed, stimulation of tectoreticular axons in PMRF evoked head and eye movements resembling those evoked by pan-neuronal SC microstimulation (Figure 3.3B-G, Figure 3.2B, C). This suggested that tectoreticular populations drive head and eye movements with stereotyped displacements and endpoints, respectively.

To determine whether tectoreticular neurons are necessary for coordinated head and eye movements, we used an optogenetic approach to selectively inhibit these neurons during an innate behavior wherein tactile stimuli elicit coupled saccades and attempted head movements closely resembling those elicited by SC stimulation (Figure 3.3H-N, Figure 3.1, Figure 3.2, Figure 3.3A-G) (Zahler et al., 2021). We injected a retrogradely infecting virus encoding Cre recombinase (*HSV-Cre*) in left central PMRF, injected AAV encoding a Cre-dependent form of the inhibitory opsin eNpHR3.0 (*AAV1-DIO-eNpHR3.0-EYFP*) in right SC, and implanted an optic fiber over right SC (Figure 3.3O) (Gradinaru et al., 2010; Neve et al., 2018). Consistent with our prediction, inhibiting tectoreticular neurons shifted left whisker airpuff-evoked movements rightward (ipsiversively) for both saccades and attempted head movements (Figure 3.3P, Q). Together, these optogenetic gain- and loss-of-function experiments demonstrate that mouse tectoreticular neurons drive gaze shifts by specifying head movement displacements and saccade endpoints.

Tectoreticular neurons encode stimulus location and head displacement

Next, we sought to understand how tectoreticular neurons encode eye and head movement commands during touch-evoked eye and attempted head movements. We performed extracellular electrophysiology in the deep layers of right SC previously

injected with *AAV1-ChR2*, identifying (“optotagging”) tectoreticular neurons as those antidromically activated by photostimulating tectoreticular terminals in the left (contralateral) PMRF, which drove eye and attempted head movements (Figure 3.4A, B, Figure S3.3A, I-N) (Li et al., 2016; Lima et al., 2009). We began by examining responses to airpuff stimulation of the left or right whiskers (Figure 3.4C). We used whisker airpuffs because they enable uncoupling of head and eye movement directions (whisker airpuffs elicit attempted head movements predominantly towards the side of the stimulated whiskers but a nearly even mix of saccade directions) (Figure 3.3I-L). Tectoreticular responses to whisker airpuffs exhibited two distinct peaks resembling responses previously observed in mouse SC that are thought to reflect bottom-up input from trigeminal and top-down input from somatosensory cortex, respectively (Figure 3.4C, D Figure S3.3B) (Castro-Alamancos and Favero, 2016). In addition, most neurons were bilaterally responsive but nearly all preferred left (contralateral) whisker airpuffs (35/53) rather than right (ipsilateral) whisker airpuffs (1/53) (Figure 3.4D-E).

Next, we examined motor activity of tectoreticular neurons in SC. We first analyzed tuning for attempted head movements. Previous studies in mice identified SC neurons tuned for specific head displacements (Masullo et al., 2019). We therefore performed similar analyses and regressed attempted head displacement against spiking activity for each neuron (Figure 3.4G). Consistent with earlier studies, most right tectoreticular neurons preferred leftward (contraversive) attempted head movements (27/53), whereas no neurons preferred rightward (ipsiversive) attempted head movements (Figure 3.4H, Figure S3.3C) (Masullo et al., 2019). To control for the correlation between airpuff location and attempted head movement direction, we

examined attempted head movement tuning for a single airpuff location and observed similar results, albeit with fewer significantly tuned neurons because the decreased number of trials reduced the power of the statistical analyses (Figure S3.4A-C). Next, we examined tuning for saccade parameters. For each neuron, we regressed saccade displacement or endpoint location against neural activity (Figure 3.4J, K, M, N). Few tectoreticular neurons showed tuning for saccade displacement (4/53) or saccade endpoint (5/53), and this small population of tuned neurons showed no overall bias for leftward versus rightward saccade displacements ($p = 0.63$, binomial test) or saccade endpoints to the left or the right of the median ($p = 1$, binomial test) (Figure 3.3K, N; Figure S3.3D, E). Next, we tested whether there are laminar differences in motor parameter tuning within deep SC, which can be further stratified into intermediate (SCi) and deep (SCd) sublaminae, by comparing the distribution of head and saccade tuning parameters between SCi and SCd. These analyses revealed only subtle differences between layers (Figure S3.4F-J). Finally, we repeated these analyses when trial data were aligned to movement onset rather than stimulus onset and when analyzing non-optotagged SC units and observed similar results (Figure S3.3F-H, Figure S3.4D, E).

To examine neural population dynamics, we performed targeted dimensionality reduction on the trial-aligned tectoreticular responses pooled across experiments. For each sensory or motor variable, we estimated a coding dimension (CD) that best separated left and right trials and projected population activity onto these dimensions. Consistent with our tuning analyses, population activity was well-separated for whisker airpuffs and attempted head movements (Figure 3.4F, I). In contrast, there was no separation in population activity for saccade displacements or endpoints (Figure 3.4L,

O). Together, these data demonstrate that tectoreticular neurons encode stimulus location and attempted head displacement, but not saccade displacement or endpoint, suggesting that saccade tuning emerges downstream of SC.

Distinct brainstem modules drive head movements with stereotyped displacements and saccades with stereotyped endpoints

Activating tectoreticular neurons drives head movements with stereotyped displacements and saccades with stereotyped endpoints, yet we found no evidence that tectoreticular neurons encode saccade parameters. This suggested that SC specifies head displacement whereas saccade endpoint and displacement are computed downstream. To better understand the role of downstream neurons in transforming tectoreticular activity into head and eye movements, we focused on two structures within PMRF implicated in driving these respective movements: the gigantocellular nucleus (Gi) and the paramedian pontine reticular formation (PPRF) (Bouvier et al., 2015; Chimoto et al., 1996; Cregg et al., 2020; Gioia and Bianchi, 1992; Isa et al., 2021; Schwenkgrub et al., 2020; Sparks et al., 2002; Usseglio et al., 2020).

We began by asking whether Gi and PPRF are specialized for head and eye movements, as studies in cats and primates have yielded mixed effects, and this question has not been addressed in mice (Gandhi et al., 2008). We reasoned that conflicting earlier results may reflect the effects of electrical microstimulation on adjacent regions or fibers of passage. To achieve more selective stimulation, we pursued an anterograde viral approach to selectively stimulate Gi or PPRF neurons that receive input from SC (Figure 3.5A, B). We injected *AAV1-Cre* into right SC to be trafficked to SC-target neurons (Zingg et al., 2017, 2020). We then injected a mixture of

AAV1 encoding a Cre-dependent ChR2 and a Cre-dependent tdTomato in left (contralateral) Gi or PPRF and implanted an optic fiber (Figure 3.5A, B). No tdTomato-labeled cell bodies were observed in SC, indicating that SC tectoreticular neurons were not retrogradely infected (Figure 3.5A, B). We then measured attempted head movements and saccades evoked by optogenetically stimulating SC-recipient Gi and PPRF neurons. Activation of SC-recipient Gi neurons elicited attempted head movements but very few saccades, whereas activation of SC-recipient PPRF neurons elicited conjugate saccades but very few attempted head movements, indicating that Gi and PPRF represent separate, specialized modules for different body parts (Figure 3.5C, D).

Next, we characterized the displacements and endpoints of movements elicited by optogenetic stimulation of SC-recipient Gi and PPRF modules. Both Gi-evoked attempted head movements and PPRF-evoked saccades were exclusively leftward (ipsiversive), consistent with the stereotypical lateralization of brainstem motor pathways (Figure 3.5E, F, K, L). This was also consistent with the uniform directionality of SC-evoked head movements in freely moving and head-fixed mice, but marked a transition from the mixture of saccade directions elicited by SC stimulation (Figure 3.2B-C, Figure 3.3B-G). Strikingly, similar to SC-evoked head and eye movements, Gi-evoked attempted head displacements were nearly invariant to initial eye position, whereas PPRF-evoked saccade displacements were strongly dependent on initial eye position (variance explained by initial eye position: 0.02 ± 0.04 [head] vs. 0.34 ± 0.22 [saccade]; mean \pm S.D.; $p = 0.002$, $n = 9$ per region, Welch's t-test) (Figure 3.5E, F, K, L, M-P). Taken together, these results suggest that SC innervates independent modules

in Gi and PPRF that transform identical excitatory input into head movements with stereotyped displacements and saccades with stereotyped endpoints, respectively.

Individual tectoreticular neurons collateralizing to Gi and PPRF drive both head and eye movements

Although SC innervates both Gi and PPRF and drives both head and eye movements, previous experiments could not determine whether single tectoreticular axons collateralize to both structures or whether separate tectoreticular subpopulations innervate each. To distinguish between these possibilities, we asked whether neurons projecting to one structure innervate the other, using a retrograde labeling approach. To avoid labeling fibers of passage, we injected the more distal structure, Gi, with retrogradely infecting virus encoding Cre (*HSV-Cre*), and we injected SC with a virus encoding a Cre-dependent tdTomato (*AAV1-FLEX-tdTomato*) (Figure 3.6A, C, E). For comparison, in a separate cohort we injected SC with an AAV encoding a constitutively expressed tdTomato (*AAV1-tdTomato*) to provide pan-neuronal labeling (Figure 3.6B, D, F). In both cohorts, we observed tdTomato-labeled axon terminals in similar spatial distributions in PPRF and Gi, including in the areas targeted for optogenetic stimulation of SC-recipient neurons, indicating that individual tectoreticular axons collateralize to innervate both Gi and PPRF (Figure 3.6C-F, Figure 3.5A, B).

We next asked whether tectoreticular neurons that collateralize in PPRF and Gi can drive both head and eye movements, or whether separate tectoreticular populations are needed (Figure 3.6G). To distinguish between these possibilities, we optogenetically stimulated SC terminals in Gi while blocking antidromically evoked recurrent activity within SC, which could recruit non-Gi-projecting SC neurons, by injecting TTX in SC

(Figure 3.6H, I). In the control condition, stimulating SC terminals in Gi elicited robust antidromic spiking in SC (Figure 3.6J, P, Q) and both attempted head and eye movements similar to those elicited by SC stimulation (Figure 3.6K, L, R-T, Figure 3.1, Figure 3.2). After TTX injection, stimulating SC axon terminals did not elicit antidromic spikes in SC (Figure 3.6M, P, Q) but continued to evoke attempted head movements and saccades indistinguishable from those evoked in the control condition (Figure 3.6N, O, R-T). These data thus indicate that tectoreticular axons with collaterals in Gi and PPRF are able to evoke both head and eye movements in the absence of recurrent dynamics or recruitment of additional cells in SC. Taken together, these anatomical and functional data suggest that individual tectoreticular neurons are able to drive both head movements with stereotyped displacements and saccades with stereotyped endpoints by collateralizing to distinct, computationally specialized target populations in Gi and PPRF.

Gi and PPRF modules execute different computations

Based on the preceding recording, tracing, and stimulation experiments, we hypothesized that Gi and PPRF execute distinct transformations of tectoreticular activity to determine head movement displacements and to compute saccade endpoints and displacements. To test this hypothesis, we performed extracellular recordings in each structure and compared neural responses to those of tectoreticular neurons (Figure 3.7A, B). Similar to tectoreticular neurons, Gi and PPRF neurons displayed biphasic responses to whisker stimulation (Figure 3.7D, Fig 3.4C). However, whereas tectoreticular and Gi populations showed similar tuning preferences for airpuff location (Figure 3.7E), PPRF neurons as a population were less biased in their preference for

left whisker airpuffs (tectoreticular: 0.66; 35/53; Gi: 0.50; 90/179; PPRF: 0.41; 120/292; $p = 0.001$ [PPRF vs. tectoreticular]; $p = 0.06$ [PPRF vs. Gi]; Fisher's exact test) (Figure 3.7E). This was consistent with the behavioral observation that airpuffs drive attempted head movements almost exclusively toward the side of the stimulated whiskers ($96 \pm 5\%$ toward, mean \pm S.D., $n = 9$ mice) but bidirectional saccades ($54 \pm 12\%$ toward, mean \pm S.D., $n = 9$ mice).

To compare movement-related activity in Gi and PPRF, we regressed attempted head movement displacement, saccade displacement, and saccade endpoint against firing rate for each neuron (Figure 3.7G, I, K). As with stimulus side, the population tuning preferences of Gi neurons resembled those of tectoreticular neurons (Figure 3.7G, I, K). In contrast, tuning in PPRF differed significantly from tectoreticular and Gi tuning for head displacement and saccade displacement, and differed significantly from Gi tuning for saccade endpoint (Figure 3.7G, I, K). Consistent with the observation that stimulating left PPRF drives leftward saccades, the difference in saccade displacement tuning was due to an increase in the proportion of PPRF neurons tuned for leftward saccades (PPRF: 0.19; 55/292; tectoreticular: 0.02; 1/53; Gi: 0.08; 15/179; $p = 0.001$ [PPRF vs. tectoreticular]; $p = 0.002$ [PPRF vs. Gi]; Fisher's exact test). In addition, tuned neurons appeared to be enriched in a particular region of the recorded area in PPRF whereas tuned neurons were more uniformly distributed throughout the recorded area in Gi (Figure S3.5).

To determine whether saccade tuning was an emergent property of SC-recipient PPRF neurons, we performed additional recordings in which anterograde AAV labeling was used to optotag PPRF neurons that receive input from SC (Figure 3.7C). We

observed different tuning in SC-recipient PPRF neurons compared to tectoreticular neurons for stimulus location, head displacement, saccade displacement, and saccade endpoint (Figure 3.7D-K). The difference in saccade tuning was due to an increase in the proportion of neurons tuned for saccade endpoints left of center (tectoreticular: 0.06; 3/53; tagged PPRF: 0.23; 8/35; $p = 0.023$ [tectoreticular vs. tagged PPRF]; Fisher's exact test) and leftward saccade displacements (tectoreticular: 0.02; 1/53; tagged PPRF: 0.20; 7/35; $p = 0.006$ [tectoreticular vs. tagged PPRF]; Fisher's exact test), consistent with a model wherein PPRF neurons transform SC input to compute saccade parameters. Taken together, these data suggest that Gi and PPRF are independent, dedicated subcircuits that differentially process SC activity to drive head movements with stereotyped displacements and saccades with stereotyped endpoints, respectively. Whereas Gi appears to function largely as a relay for head displacement signals received from SC, PPRF transforms SC activity into saccade endpoints and displacements.

3.4 DISCUSSION

Here we investigated the neural mechanisms that underlie coordinated movements. In particular, we sought to understand the circuit architecture and computations that transform a desired overall displacement into movement commands for individual body parts. To address this question, we pursued a systematic approach to interrogate the neural coordination of mouse gaze. By stimulating and recording in multiple connected nodes at different levels in the mouse gaze motor hierarchy, we unexpectedly revealed that no individual stage in this anatomical hierarchy computes the desired overall displacement. Instead, single upper motor neurons in SC specify a mixture of head displacements and eye endpoints, with displacements for different body parts computed independently and at distinct anatomical stages. As such, the computations within this anatomical hierarchy do not follow a straightforward progression from higher-order parameters down to the level of individual body parts. The multiplexing of movement displacements and endpoints for different body parts by single upper motor neurons in SC is made possible by dedicated hindbrain modules for each body part. These modules in Gi and PPRF differentially process SC input, transforming identical excitatory drive into head movements with stereotyped displacements and saccades with stereotyped endpoints, respectively. These findings thus broaden the space of conceptual models of movement coordination, revealing a non-hierarchical computational logic implemented within an anatomical hierarchy.

In primates and cats, several studies have shown that SC neurons encode the overall gaze displacement but not necessarily the individual eye and head displacements (Bergeron et al., 2003; Freedman, 2008; Freedman et al., 1996b; Paré et

al., 1994; Sajad et al., 2020). Although analogous stimulation studies in mice had found that mouse SC harbors topographic head and eye motor maps, it was not determined what movement parameters (e.g., overall gaze displacement or individual head and eye displacements) were encoded (Masullo et al., 2019; Wang et al., 2015). In particular, one study reported the puzzling observation that sustained (> 250 ms) optogenetic stimulation of tectoreticular neurons in freely moving mice evoked a series of step-wise head movements, reminiscent of the saccade “staircase” evoked by sustained SC microstimulation in head-fixed primates, but sustained optogenetic stimulation of the same tectoreticular neurons in head-fixed mice evoked a single saccade (Masullo et al., 2019; Schiller and Stryker, 1972). By accounting for initial head and eye position, we determined that the topographic motor maps in mouse SC correspond to head displacements and saccade endpoints. This result may explain why sustained mouse tectoreticular stimulation did not elicit saccade “staircases”—after the eyes made a single saccade, they reached the endpoint specified by that ensemble of SC neurons, and no additional saccades were needed (Masullo et al., 2019). Most importantly, because the saccade displacement needed to reach a given endpoint varies with initial eye position, our results indicate that mouse SC does not specify overall gaze displacements (Figure 3.1).

A potential benefit of stereotyping saccade endpoints is that it ensures the eyes return to the center by anticipating head movements and their associated image-stabilizing VOR eye movements (Land, 2019). Such a coding strategy may underlie the widespread yet unexplained observation in most vertebrate species (i.e., those lacking a high-acuity retinal specialization such as a fovea, including birds, frogs, mice, and

rabbits) that the eyes tend to return to the centers of the orbits after gaze shifts, a phenomenon known as recentering (Land, 2019; Land and Nilsson, 2012; Meyer et al., 2020; Michael et al., 2020). In this model, saccades themselves do not recenter the eyes, but instead anticipate and offset the subsequent head movement-evoked slow VOR eye movement, thereby ensuring the eyes settle in a central final position. This may explain why saccade endpoint eccentricity scales with anteroposterior location in SC, paralleling head displacement amplitude: larger head movements elicit larger slow VOR movements that must be offset by more eccentric saccade endpoints. Together, these results provide a candidate mechanism to explain how mice primarily use head movements to shift gaze and saccades to ensure the eyes end in a central orbital position.

Gaze shifts belong to a large and varied group of complex, reflexive behaviors that involve coordinated movements of multiple body parts and end in a stereotyped pose, e.g., the hand or forepaw at the mouth during consummatory behaviors. Other examples include escape, approach, predation, grooming, courtship, and aggressive behaviors (Arber and Costa, 2022; Evans et al., 2018; Ferreira-Pinto et al., 2021; Hoy et al., 2019; Lin et al., 2011; Ruder and Arber, 2019; Ruder et al., 2021; Shang et al., 2019b; Xie et al., 2022). Interestingly, many of these behaviors can also be triggered by activating specific subcortical regions and cell types in areas such as SC, hypothalamus, periaqueductal gray, and hindbrain (Evans et al., 2018; Ferreira-Pinto et al., 2021; Hoy et al., 2019; Lin et al., 2011; Ruder et al., 2021; Xie et al., 2022). In the future, it will be important to investigate whether neurons in these regions coordinate these movements using a strategy similar to that of mouse SC tectoreticular neurons,

i.e., simultaneously specifying a mixture of displacements and endpoints for different body parts.

We found that individual SC neurons are able to simultaneously specify head displacements and saccade endpoints because they engage dedicated, computationally specialized brainstem modules for different body parts. Beyond ensuring coordinated movements end in a stereotyped pose, this generalizable modular architecture may offer additional benefits to the organism. First, a modular architecture may facilitate the evolution of the neural control of movements tailored to the anatomy and ethology of different species. For example, whereas mouse SC drives head movements with stereotyped displacements and saccades with stereotyped endpoints, the mechanics of gaze shifts differ in owls, which do not move their eyes, and mammalian species with high-acuity retinal specializations (e.g., foveae) such as cats and primates, where SC is believed to encode overall gaze displacement but not the individual displacements or endpoints for the head and eyes (Bergeron et al., 2003; Freedman, 2008; Freedman and Sparks, 1997; Freedman et al., 1996a; Knudsen, 1989; Sajad et al., 2020). A similar diversification is observed for other body parts, e.g., the forelimb takes the form of an arm in a human, a flipper in a whale, and a wing in a bat, with each used for different movements (Krubitzer and Prescott, 2018). Second, modules encoding movement endpoints for certain body parts may facilitate feedback control and course correction (Merel et al., 2019; Todorov, 2004).

Limitations of the study

Our study found that individual tectoreticular neurons collateralize to both PPRF and Gi to drive both head and eye movements. These collaterals may explain why

saccades in rodents (and other afoveates) have not been observed in the absence of head movements, whereas primates can generate saccades independently of head movements to direct their foveae towards salient stimuli (Land, 2019). Nevertheless, it remains possible that subpopulations of mouse SC neurons innervate only PPRF or Gi, as has been observed in primates and is presumed to underlie their ability to saccade absent head movements (Moschovakis et al., 1988b; Scudder et al., 2002). Such populations would be difficult to detect using the approaches in this study. Instead, an approach involving sparse labeling and reconstruction of the axonal arbors of SC neurons would be needed. Such an endeavor has been undertaken for other brain areas under the auspices of the Janelia MouseLight project, but this effort has not, to our knowledge, examined SC projection neurons (Winnubst et al., 2019).

We examined how mouse SC specifies the horizontal component of gaze shifts, finding that SC neurons engage distinct modules of neurons in Gi and PPRF that transform identical exogenous excitation into movements with fixed displacements and endpoints, respectively. Our findings suggest that the internal computations within Gi and PPRF differ but do not reveal how these computations are implemented. SC-recipient Gi neurons appear to be a relay for head displacement signals from SC. Relays elsewhere in the brain, e.g., primary sensory thalamus, were subsequently shown to perform more sophisticated processes, including attentional gating and surround modulation (Sherman, 2007). Whether Gi functions similarly, and what afferents may provide gating or other modulatory cues to Gi, will be important to investigate in the future. In contrast, our data suggest that neurons within or downstream of PPRF transform SC signals carrying information about stimulus location

and head displacement into the desired saccade endpoint and subsequently the displacement needed to reach that endpoint from the initial position of the eyes, possibly performing these transformations across multiple cell types. Consistent with this idea, PPRF is believed to comprise at least two cell types, long-latency burst neurons (LLBNs) and excitatory burst neurons (EBNs), that form a putative network topology of SC→LLBN→EBN→abducens motor neurons (Keller et al., 2000). In the future, it will be important to identify the cell types within this circuit that compute saccade endpoint and displacement and the source of the eye position information that enables the transformation from endpoint to displacement.

In addition to further unraveling how SC, Gi, and PPRF control the horizontal component of gaze shifts, future work should determine whether the logic we have identified applies to SC control of mouse gaze movements in other axes, which are thought to be controlled by distinct downstream circuitry (Isa et al., 2021). There are additional key differences between gaze movements in these axes worth investigating, e.g., whereas the eye movements that accompany head yaw are conjugate, it has been reported that changes in head pitch are accompanied by non-conjugate changes in eye position, with lower head pitch associated with more converged eye position (Meyer et al., 2018; Michaiel et al., 2020; Wallace et al., 2013). These vergence eye movements are believed to be driven by otolith-mediated sensing of head pitch, analogous to the slow counter-rotational horizontal VOR eye movements driven by vestibular sensing of head rotation (Figure 3.1), but the underlying circuitry is not understood (Khan et al., 2019; Oommen and Stahl, 2008). In the future, an approach similar to that in the

present study may enable deconstruction of the circuit logic controlling gaze in other axes.

The gaze shifts we have studied are a reflexive, unlearned form of coordinated movement, but many coordinated movements are skills honed through repetition and are generated volitionally. These behaviors, such as playing the piano or hitting a tennis serve, are thought to involve distinct neural hierarchies that include forebrain areas such as cortex and basal ganglia. It is unclear whether the computational logic identified in this study will be relevant to those circuits (Dudman and Krakauer, 2016; Guo et al., 2015; Peters et al., 2017; Shenoy et al., 2013; Strick et al., 2021). Nevertheless, the approach we have applied to systematically deconstruct transformations at downstream structures may be useful for investigating these pathways. Moreover, although differences between systems are likely, our model may provide a useful point of comparison in efforts to unravel computations within other motor hierarchies.

3.5 METHODS

Surgical procedures

Mice were administered meloxicam (5 mg/kg) 30 min prior to surgery. Anesthesia was induced with inhalation of 2.5% isoflurane and buprenorphine (1.5 mg/kg) was administered at the onset of the procedure. Isoflurane (0.5-2.5% in oxygen, 1 L/min) was used to maintain anesthesia and adjusted based on the mouse's breath and reflexes. Ocular gel was used to protect the eyes from dehydration. Once anesthetized, Nair was used to remove hair from the scalp and the surgical area was disinfected using alcohol and iodine wipes. Following surgery, mice were allowed to recover in their home cages for at least 1 week.

The skull was exposed by removing a 5 mm diameter circle of skin using spring scissors. Prior to viral injections, a small hole was drilled in the skull using a 0.5 mm burr dental drill. Viruses were delivered to the target brain regions using pulled glass pipettes coupled to a microsyringe pump (UMP3T-1, World Precision Instruments) controlled by a stereotaxic frame (Model 940, Kopf Instruments). A titanium headplate was cemented to the leveled skull (Metabond, Parkell).

For optogenetic manipulations, fiber optic cannulae were constructed from ceramic ferrules (CFLC440-10, Thorlabs) and optical fiber (400 μm core, 0.39 NA, FT400UMT) using low-autofluorescence epoxy (F112, Eccobond). Cannulae were targeted using a cannula holder (Thorlabs, XCL) coupled to a stereotaxic frame.

To prepare animals for freely moving recordings, the female end of a Mill-Max connector (Mill-Max Manufacturing Corp. 853-93-100-10-001000) was cut to 5 mm (2

rows of 4 columns) and cemented to the rostral end of the mouse's headplate. Camera assemblies were reversibly attached via this connector during recording sessions.

For electrical microstimulation and electrode recordings, a 1 mm craniotomy was performed with a 0.5 mm burr dental drill over right SC (centered around ML: 1.1 mm, AP: 0.6 mm relative to lambda), left PPRF (centered around ML: 0.5 mm, AP: -0.5 mm relative to lambda), or left Gi (centered around ML: 0.4 mm, AP: -1.4 mm relative to lambda). A ~2 mm high Metabond well was constructed around the craniotomy to retain saline during recording sessions. Craniotomies were performed 18-24 hours in advance of recordings and filled with removable silicone sealant (Kwik-Cast). In addition, a screw was inserted into the skull rostral to bregma and attached to a ground wire.

Freely moving behavior

Timing and synchronization of the freely moving behavior were controlled by a microcontroller (Arduino MEGA, 2560 Rev3, Arduino) receiving serial commands from MATLAB. All behavioral and data acquisition timing information was recorded by a NI DAQ (USB-6001) for post hoc alignment. Mice were allowed to move freely on a custom transparent platform measuring 8" x 8". Body tracking was accomplished using a camera (Flir, BFS-U3-28S5M-C) recording at 100 Hz from below the animal. The mouse was illuminated from two sides with visible light, and a black backdrop was placed above the platform to provide contrast. The platform was mounted on a turntable (18635A54, McMaster-Carr) that was periodically rotated to avoid tangling of the wires. To measure eye movements, two miniature cameras (1937, Adafruit) were used. Each camera was fitted with a miniature bandpass filter (Filter Opt Cast IR 5 mm, Edmund Optics) and both were mounted on the head using a 3D-printed camera holder. One IR

LED was used to illuminate each eye and generate a corneal reflection for computing angular eye position. Videos of both the left and right eyes were recorded at 90 Hz. To measure head movements, a 9-axis inertial measurement unit (IMU) (HMT-00203, Rosco Technologies) recording at 100 Hz was mounted to the camera holder.

Head-fixed behavior

During experiments, headplated mice were secured in a 3D-printed mouse holder. Timing and synchronization of the behavior were controlled by a microcontroller (Arduino MEGA 2560 Rev3, Arduino) receiving serial commands from MATLAB. All behavioral and data acquisition timing information was recorded by a NI DAQ (USB-6001) for post hoc alignment. The movements of both left and right eyes were monitored at 100 Hz using two cameras (BFS-U3-28S5M-C, Flir) coupled to 110 mm working distance 0.5 X telecentric lenses (#67-303, Edmund Optics). A bandpass filter (FB850-40, Thorlabs) was attached to the lens to block visible illumination. Three IR LEDs (475-1200-ND, DigiKey) were used to illuminate the eye and a fourth LED was aligned to the camera's vertical axis to generate a corneal reflection. Attempted head rotations were measured using a 3D-printed headplate holder coupled to a load cell force sensor (Sparkfun, SEN-14727). Load cell measurements (sampling frequency 80 Hz) were converted to analog signals and recorded using a NI DAQ (sampling frequency 2000 Hz).

Electrical microstimulation

Electrical stimulation experiments were performed in head-fixed mice using a 16-channel Neuronexus probe (A4x4-4mm-200-200-1250-A16) arranged as a linear array of four shanks spaced by 200 μm . Each shank housed four linearly arranged electrodes

separated by 200 μm . Electrodes had large surface areas (1250 μm^2) capable of delivering large currents. Prior to insertion, probe shanks were coated with Dil (1 mM, Thermo Fisher Scientific) to permit histological reconstruction of the probe track. The probe's ground wire was attached to a cortical skull screw and the craniotomy was filled with saline. The probe was oriented along the anterior-posterior axis and lowered into SC through intact dura using a micromanipulator (Sensapex, uMp-4) at a speed of 5 $\mu\text{m}/\text{s}$ to the desired depth. We focused on the anterior-posterior axis in SC because head-fixed mice make predominantly horizontal eye movements and earlier studies suggested that horizontal saccade displacements are represented along this SC axis (Meyer et al., 2018, 2020; Michael et al., 2020; Payne and Raymond, 2017; Wallace et al., 2013). Probes were allowed to settle for 15 minutes before a stimulation session. Microstimulation was achieved using an Intan RHS stimulation-recording system and Intan software. Stimuli consisted of biphasic pulses (0.2 ms per phase) delivered for 10 ms with amplitudes of 30-60 μA . The electrode array was lowered to 1.5 mm below dura and then incrementally advanced while the distal electrodes were tested. Depths and stimulation currents were selected as the shallowest and lowest values, respectively, that regularly evoked saccades using each shank. Experiments consisted of 400-480 pseudorandomly interleaved stimulation trials (100-120 per shank) separated by inter-trial intervals drawn from a 5-10 s uniform distribution. SC electrical microstimulation data were obtained from nine mice and mice underwent one session each.

Whisker airpuff behavior

Airpuffs were applied to the whiskers of head-fixed mice to evoke directionally biased attempted head and eye movements. Airpuff stimuli were generated using 3D-

printed airpuff nozzles (1.5 mm wide, 10 mm long), spaced 24 mm apart, and centered 10 mm beneath the mouse's left and right whiskers. Airpuff nozzles were connected to compressed air (5 psi) that was gated by a solenoid. For tectoreticular loss-of-function experiments, left and right stimuli were randomly selected and presented at intervals drawn from a 7-12 s uniform distribution. Each session consisted of 350 stimulus presentations and lasted ~55 minutes. For SC, PPRF, and Gi electrophysiological recordings, left and right stimuli were randomly selected and presented at intervals drawn from a 3-7 s uniform distribution. Each session consisted of 700 stimulus presentations and lasted ~60 minutes. For electrophysiological recordings, only mice with a high probability of generating touch-evoked saccades (>50 saccades/session) were used. Besides this screening process, no training or habituation was necessary.

Optogenetic stimulation and inhibition

Fiber optic cables were coupled to implanted fibers and the junction was shielded with black heat shrink. A 470 nm fiber-coupled LED (M470F3, Thorlabs) was used to excite ChR2-expressing neurons, and a 554 nm fiber-coupled LED (MINTF4, Thorlabs) was used to inhibit eNpHR3.0-expressing neurons.

For optogenetic activation of SC neurons in freely-moving mice, a 1:1 mixture of *AAV1.hSyn.ChR2(H134R)-eYFP* and *AAV1-CAG.tdTomato* was injected in right SC (0.6 AP, 1.1 ML, -2.1 and -1.9 DV; 100 nL per depth), and a fiber was implanted over the injection site (0.6 AP, 1.1 ML, -2.0 DV). Experiments were performed between 14-24 days post-injection. LED intensity was individually set to evoke an orienting movement without a flinching response (0.5-1.5 mW). Each session consisted of 700 stimulation

trials (100 ms duration, 2-5 s interval) and lasted ~40 minutes. Mice underwent three sessions each.

For optogenetic activation of SC-recipient Gi or PPRF neurons in head-fixed mice, *AAV1.hSyn.Cre* was injected into right SC (0.6 AP, 1.1 ML, -1.9 and -2.1 DV; 100 nL per depth), a 1:1 mixture of *AAV1.EF1a.DIO.hChR2(H134R)-eYFP* and *AAV1.CAG-FLEX-tdTomato* was injected into left PPRF (-0.5 AP, 0.5 ML, -4.7 and -4.9 DV; 100 nL per depth) or left Gi (-1.4 AP, 0.4 ML, -5.25, -5.5, -5.75, and -6.0 DV; 100 nL per depth), and an optic fiber was implanted over left PPRF (-0.5 AP, 0.5 ML, -4.7 DV) or left Gi (-1.4 AP, 0.4 ML, -5.3 DV). Experiments were performed between 14-31 days post-injection. Each session consisted of 350 stimulation trials (40 ms duration, 8.5 mW intensity, 7-12 s interval) and lasted ~55 minutes. Mice underwent one session each.

For optogenetic activation of abducens motor neurons, *Chat-Cre* mice (Jackson Laboratory strain 108957) were injected with a 1:1 mixture of *AAV1.EF1a.DIO.hChR2(H134R)-eYFP* and *AAV1.CAG-FLEX-tdTomato* in left abducens (-1.1 AP, 0.4 ML, -4.6, and -4.8 DV; 50 nL per depth), and an optic fiber was implanted over abducens (-1.1 AP, 0.4 ML, -4.55 DV). Experiments were performed 14 days post-injection. LED intensity was individually set to evoke a ~5° eye movement (0.037-1.75 mW). Each session consisted of 350 stimulation trials (500 ms, 7-12 s interval). Mice underwent one session each.

For optogenetic inhibition of tectoreticular neurons during the whisker airpuff behavior, mice were injected with *HSV-hEF1α-cre* in left PMRF (-0.8 AP, 0.4 ML, -4.7, -4.9, -5.1 DV; 100 nL per depth) and a 1:1 mixture of *AAV1.EF1a.DIO.eNpHR3.0-eYFP* and *AAV1.CAG-FLEX-tdTomato* in right SC (0.6 AP, 1.1 ML, -2.1 and -1.9 DV; 100 nL

per depth), and an optic fiber was implanted over right SC (0.6 AP, 1.1 ML, -2.0 DV). Experiments were performed between 21-50 days post-injection. Each session consisted of 350 whisker airpuff trials, and light (8.5 mW) was delivered to SC for 1 s centered around airpuff onset on a random 50% of trials. Mice underwent 6 whisker airpuff sessions each.

Pharmacological silencing of SC

For optogenetic activation of SC axon terminals in head-fixed mice, a 1:1 mixture of *AAV1.hSyn.ChR2(H134R)-eYFP* and *AAV1-CAG.tdTomato* was injected in right SC (0.6 AP, 1.1 ML, -2.1 and -1.9 DV; 100 nL per depth), and an optic fiber was implanted over left Gi (-1.4 AP, 0.4 ML, -5.3 DV). Experiments were performed between 10-20 days post-injection. Each mouse underwent an initial control session before undergoing an experimental session (+TTX) session the following day. Each session consisted of 350 stimulation trials and identical light intensities were used for each mouse across days (40 ms duration, 1-2 mW intensity, 7-12 s interval). One hour before the experimental session, 100 nL of either saline or tetrodotoxin-citrate (Alomone Labs, T-550; 40 μ m) was injected in right SC (0.6 AP, 1.1 ML, -2.0 DV). All mice displayed prominent ipsiversive circling behavior following TTX injection, consistent with SC silencing. During both the control and TTX sessions, an electrode was inserted in SC (see Single-unit recordings) to detect the presence or absence of neural activity. In two of the animals, additional electrode recordings were performed to confirm TTX-mediated silencing at least 2 mm ventral and 1 mm anterior of the injection site, suggesting that all of SC was silenced.

Single-unit recordings

Acute recordings were performed in head-fixed mice using either a 128-channel Neuronexus probe (A4x32-Poly2-5mm-23s-200-177) or a 64-channel Cambridge NeuroTech optrode (ASSY-77 H6, 100 μm core lambda-b fiber with 300 μm horizontal separation between the probe and fiber). Prior to insertion, probe shanks were coated with Dil (1 mM, Thermo Fisher Scientific) to allow post hoc histological reconstruction of the probe track, the probe's ground wire was attached to the skull screw, and the craniotomy was covered in saline. The probe was lowered using a micromanipulator (Sensapex) through intact dura at a speed of 5 $\mu\text{m}/\text{s}$ to 100 μm below the desired depth, and then raised at a speed of 2 $\mu\text{m}/\text{s}$ to the desired depth. The probe was allowed to settle for at least 25 minutes before recording began. Mice underwent multiple recording sessions on successive days unless their craniotomies showed signs of decay (e.g., dura no longer intact, signs of bleeding, or scar tissue formation). Craniotomies were covered with silicone (Kwik-Cast) between sessions. Extracellular potentials were acquired using an Intan RHS recording system and Intan RHX software.

Optotagging

Tectoreticular neurons were identified using antidromic optotagging. A 1:1 mixture of *AAV1.hSyn.ChR2(H134R)-eYFP* and *AAV1-CAG.tdtomato* was injected in right SC (0.6 AP, 1.1 ML, -2.1 and -1.9 DV; 100 nL per depth), and a 400 μm fiber was implanted in left contralateral medial PMRF (-0.8 AP, -0.4 ML, -4.7 DV). After ten days, animals were screened for ChR2 expression by determining whether head and eye movements were evoked by light pulses (470 nm, 40 ms, 1 mW) delivered to PMRF. Single unit recordings were performed in the 10-30 days post-injection. Tectoreticular

neurons were identified as those antidromically activated by photostimulating axon terminals in the contralateral medial PMRF. At the beginning and end of each recording session, 20 pulses of 470 nm light (5 ms pulse duration, separated by 100 ms, 1 mW intensity) were delivered through an optical fiber implanted over PMRF. Neurons were classified as tectoreticular (10-38% of neurons recorded in a given session) if they reliably responded to photostimulation (>80% response rate) with short latency (<5 ms), low temporal jitter (<2 ms), and with similar waveforms as spontaneous action potentials (correlation coefficient > 0.90).

We used an optrode to identify SC-recipient PPRF neurons. First, *AAV1.hSyn.Cre* was injected into right SC (0.6 AP, 1.1 ML, -2.0 DV; 150 nL), and a 1:1 mixture of *AAV1.EF1a.DIO.hChR2(H134R)-eYFP* and *AAV1.CAG-FLEX-tdTomato* was injected into left PPRF (-0.5 AP, 0.5 ML, -4.7 and -4.9 DV; 100 nL per depth). Optagging experiments were performed in the 10-20 days post-injection. SC-recipient PPRF neurons were then identified as those activated by photostimulating PPRF soma using a 473 nm fiber-coupled laser (Shanghai Laser & Optics Century). At the beginning and end of each recording session, 20 pulses of 470 nm light (10 ms pulse duration, separated by 100 ms, 10 mW intensity) were delivered through a 100 μ m diameter optical fiber attached to the probe. Neurons were classified as SC-recipient (4-44% of neurons recorded in a given session) if they reliably responded to photostimulation (>80% response rate) with short latency (<10 ms), low temporal jitter (<2 ms), and with similar waveforms as spontaneous action potentials (correlation coefficient > 0.90).

Tracing

To examine axon collaterals of Gi-projecting SC neurons, mice were injected with *HSV-hEF1 α -Cre* in left Gi (-1.4 AP, 0.4 ML, -5.5 and -5.75 DV; 100 nL per depth), and *AAV1.CAG-FLEX-tdTomato* in right SC (0.6 AP, 1.1 ML, -2.0 DV; 150 nL). To examine the axon collaterals of pan-neuronal SC neurons, a separate cohort of mice were injected with a 1:1 mixture of *AAV1-hSyn.HI.eGFP-Cre* and *AAV1.CAG-FLEX-tdTomato* in right SC (0.6 AP, 1.1 ML, -2.0 DV; 100 nL). Mice were euthanized 14 days post-injection and their brains were histologically processed and imaged.

Histology

For histological confirmation of electrode placements, fiber placements, injection sites, and for tracing experiments, mice were perfused with PBS followed by 4% paraformaldehyde (PFA). Brains were removed and fixed overnight in 4% PFA and stored in 20% sucrose solution for at least 1 day. Brains were sectioned at 50 μ m thickness using a cryostat (NX70, Cryostar), mounted, and coverslipped using DAPI mounting medium (Southern Biotech). For histological confirmation of electrode placements, fiber placements, and injection sites, tile scans were acquired using a confocal microscope (LSM700, Zeiss) coupled to a 10X air objective. For quantifying SC tectoreticular axonal projections, z-stack tile scans (10 μ m spacing) were acquired using a confocal microscope coupled to a 10X air objective.

Anatomical reconstructions and analysis

Confocal tile scans of coronal brain sections were manually registered to the Allen Mouse Common Coordinate Framework, Version 3 (Allen CCF) and anatomical points of interest (e.g., the tips of electrode and fiber tracks) were manually identified

using a MATLAB-based GUI (Shamash et al., 2018). Briefly, each brain section image was matched to a 2D slice through the Allen CCF reference volume, common landmarks were identified between the brain section and reference image, and the section image was warped to align with the reference image using affine transformations. For visualization, reconstructed anatomical features were projected onto 2D coronal slices through the Allen CCF reference volume. AP and DV coordinates were reported relative to the origin of the Allen CCF volume (the anterior, superior, right corner) and ML coordinates were reported relative to the midline (5700 μm from the right edge of the volume).

To quantify SC projections, coronal brain section images were registered to Allen CCF and a rolling-ball background subtraction was performed to level variance in background autofluorescence. Images were binarized at a threshold determined to isolate axonal and terminal processes. Expression was quantified by binning pixels into 50 μm blocks (heatmaps) or averaging a 300 μm thick horizontal stripe (line profiles). Data from sections were normalized to peak (heatmaps) or area under curve (line profiles) before averaging to show proportional expression within each structure.

Allen CCF unit coordinates from single unit recordings were reconstructed by identifying the electrical channel with the largest amplitude spike waveform and using the probe's geometry and insertion angle of incidence to estimate coordinates relative to the tip. Probe insertion relative to the Allen CCF was determined to be angled slightly posterior (-7°). Random jitter ($\pm 10 \mu\text{m}$) was added to unit coordinates to prevent eclipsing in scatter plots. Unit tunings were identified using methods described below ("Electrophysiological Analysis"). Two-dimensional density plots were generated using

Gaussian kernel-density estimates and plotting six equally spaced density lines from 30-100% of the of highest density.

Freely moving behavior analysis

Body camera videos were processed post hoc using DeepLabCut (Mathis et al., 2018). The network was trained to detect six features on the mouse: nose, chest, abdomen, tail base, and the two camera LEDs. Frames were excluded if the platform was moving or if any of the tracked points had a DeepLabCut-calculated likelihood of $p < 0.99$. Eye camera videos were processed post hoc using DeepLabCut. The network was trained to detect the top, bottom, left and right edges of the pupil and the left and right edges of the corneal reflection. Frames with a DeepLabCut-calculated likelihood of $p < 0.99$ were excluded from analysis. The pupil data were interpolated to match the body camera sampling rate (100 Hz), and angular eye position was determined using a previously described method developed for C57BL/6J (Sakatani and Isa, 2007).

Head yaw position was determined by integrating the IMU yaw velocity. To obtain the angle of the head relative to the body (used to determine starting head-body posture), the instantaneous yaw angle of the head relative to the body was calculated using the nose, chest, and abdomen features extracted using DeepLabCut. For each timepoint, the direction of the head was found as the vector \mathbf{h} between the chest and nose, and the direction of the body was the vector \mathbf{b} between the abdomen and chest. The angle between these vectors was found using the dot product: $\theta = \cos^{-1} [(\mathbf{h} \cdot \mathbf{b}) / (|\mathbf{h}| |\mathbf{b}|)]$, and the sign was determined using the cross product. To organize head movement traces by starting head-body angle, the IMU-derived head positions for each trial were aligned according to the video-derived head-body angle. Head movement

detection was adapted from (Masullo et al., 2019). We focused on yaw head rotations because SC stimulation-evoked movements were primarily along the yaw axis (Figure S3.1B). Head movements were identified when angular velocity exceeded $140^{\circ}/s$ in the same direction for at least 30 ms. Head movement onset and offset were found by moving backward or forward, respectively, in time from the seed location until velocity fell below $28^{\circ}/s$ or velocity direction changed. Total head movement amplitude was the difference between the head positions at offset and onset (Figure S3.1B).

We observed two distinct phases of eye motion: a fast saccadic phase coinciding with head movement onset followed by a slow phase whose magnitude was roughly equal and opposite to the ongoing head rotation (Figure 3.1C). This slow phase resembled a gaze-stabilizing reflex driven by vestibular feedback (vestibulo ocular reflex, VOR) (Meyer et al., 2020; Michaiel et al., 2020; Payne and Raymond, 2017). We focused our analyses on the horizontal component of the fast saccadic phase because evoked saccades were primarily confined to the horizontal axis (Figure S3.1A). Saccades were identified separately for left and right pupils. Seed positions for tentative saccades were identified as timepoints where pupil velocity exceeded $550^{\circ}/s$ in the horizontal axis. To ensure that saccades were not counted more than once, a seed time point was only considered if it was the local maximum velocity within a ± 50 ms time window. To identify the saccade onset and offset, a ± 50 ms window around each seed was oversampled by a factor of two (5 ms resolution). Saccade onset and offset were defined as the first time point where velocity fell below $70^{\circ}/s$ or changed direction. If neither of those criteria were met, onset or offset was set at ± 35 ms. Saccade amplitude was the difference between the pupil positions at offset and onset. For putative

saccades to be included in analysis, both pupils needed to make saccade-like movements in the same direction within 30 ms of each other. Saccades displayed a main sequence, i.e., peak velocity scaled linearly with amplitude, and saccade amplitude was highly correlated between eyes (Figure S3.1C-E).

Stimulus-evoked movements were defined as saccades or head movements occurring in the 100 ms period following optogenetic stimulation onset. To distinguish stimulation-evoked saccades from spontaneously occurring saccades, we only considered trials in which the eyes and head were stationary in the 50 ms and 100 ms, respectively, preceding stimulation onset. Furthermore, to exclude VOR-induced saccades, we only examined saccades in which the eyes remained stationary between stimulation onset and saccade onset. The head and eye components of stimulation-evoked gaze shifts were defined as the amplitude of the saccadic phase of eye motion and the distance traveled by the head between head movement onset and saccade offset, respectively. Eye or head position dependence was quantified using linear regression (Figure 3.1).

Head-fixed behavior analysis

Eye camera videos were processed post hoc using DeepLabCut. The network was trained to detect the left and right edges of the pupil and the left and right edges of the corneal reflection. Frames with a DeepLabCut-calculated likelihood of $p < 0.99$ were discarded from analysis. Eye position was defined as the average of the left and right pupil positions minus the mean. Saccades were defined as eye movements that exceeded $100^\circ/\text{s}$, were at least 3° in amplitude, and were not preceded by a saccade in the previous 100 ms. The initial positions and endpoints of saccades were defined as

the first points at which saccade velocity rose above $30^\circ/\text{s}$ and fell below $20^\circ/\text{s}$, respectively. Analyses focused on horizontal saccades because saccades in head-fixed mice are strongly confined to the azimuth. Raw attempted head rotation data were low-pass filtered at 80 Hz using a zero-phase second-order Butterworth filter, interpolated to match the pupil sampling rate (100Hz), and Z-scored. For some experiments, behavioral sessions for individual mice were combined across days.

Stimulus-evoked saccades were defined as saccades occurring in the 100 ms period following stimulus onset (i.e., microstimulation, optogenetic excitation, or airpuff delivery), and stimulus-evoked head movements were defined as the head-sensor reading 80 ms post-stimulus onset. A stimulus was deemed to have evoked a head movement if the magnitude of the head movement exceeded 0.2 Z. To examine the eye position-dependence of stimulus-evoked saccades, only trials in which the eyes were stationary in the 500 ms period preceding stimulus onset were used. To examine the eye position-dependence of stimulus-evoked head movements, only trials in which the head was stationary in the 500 ms period preceding stimulus onset were used. Eye position-dependence was quantified using linear regression with Z-scored standardized variables.

Classifying electrical stimulation site was performed on data from individual mice using multinomial logistic regression. Predictors (saccade amplitude and saccade endpoint) were Z-scored standardized. Data were randomly subsampled to include an equal number of values per class (shank). Cross validation was used to train multinomial logistic regression models and test fold predictions were used to compute accuracy. This process was repeated 100 times and the mean accuracy was used as

the measure of predictor performance. Randomly shuffling shank labels for saccade amplitude or saccade endpoint before cross validation resulted in accuracies of ~ 0.25 , consistent with chance.

Electrophysiological analysis

Spike sorting was performed using KiloSort2.5 software (Pachitariu et al., 2023; Steinmetz et al., 2021) followed by manual curation using Phy2 (<https://github.com/cortex-lab/phy>). Units with an average firing rate below 0.2 Hz, more than 1% of detected events with an absolute refractory period < 1 ms, significant amplitude drift across the recording session, or atypical waveforms were excluded.

All units were pooled for analysis. Firing rate traces were smoothed with a 10 ms Gaussian window for display purposes. For each unit, tuning for puff side was determined by comparing spike counts in the 50 ms following puff onset in left versus right puff trials (two-tailed t-test, $p < 0.05$). To identify motor-tuned units, spike counts in the 50 ms following puff onset were regressed against head displacement, saccade displacement, or saccade endpoint. Tuned units were defined as those with a linear regression P-value below 0.05, and preference for left versus right movements was determined using the sign of the regression slope. For head movement tuning analyses, only trials in which mice did not move their head in the 100 ms prior to stimulus onset were used. For saccade tuning analyses, only trials in which mice did not saccade in the 100 ms prior to stimulus onset were used. A Chi-squared test was used to compare the proportions of left-preferring, right-preferring, and untuned units across brain regions. A binomial test was used to determine tuning preference within each brain region.

Targeted dimensionality reduction was used to examine the population dynamics of SC activity during touch-evoked gaze shifts. We pooled all n units from different sessions and mice for analysis. Our goal was to identify $n \times 1$ vectors that maximally accounted for response variance due to each behavioral variable. We then sought to visualize population dynamics in this subspace. We refer to these vectors as the coding dimension (**CD**), and computed **CD** for left vs. right stimulus locations, head displacements, saccade displacements, and saccade endpoints. **CD** was computed by subtracting the average spike count during the 50 ms window following airpuff onset for left - right trials, and dividing this $n \times 1$ vector by its length. We then projected population activity aligned to stimulus onset in left trials ($x(t)_{\text{left}}$) and right trials ($x(t)_{\text{right}}$) along **CD** ($\text{CD}^T x$). This allowed us to visualize population dynamics in a behaviorally relevant subspace. Selectivity was defined as the difference between left and right projections ($\text{CD}^T x_{\text{left}} - \text{CD}^T x_{\text{right}}$). To visualize projections and determine significance, we used bootstrapping across units. Each bootstrap consisted of resampling units with replacement and computing **CDs** de novo. Traces show bootstrapped median values and shading indicates 1-99% confidence intervals.

3.6 FIGURES

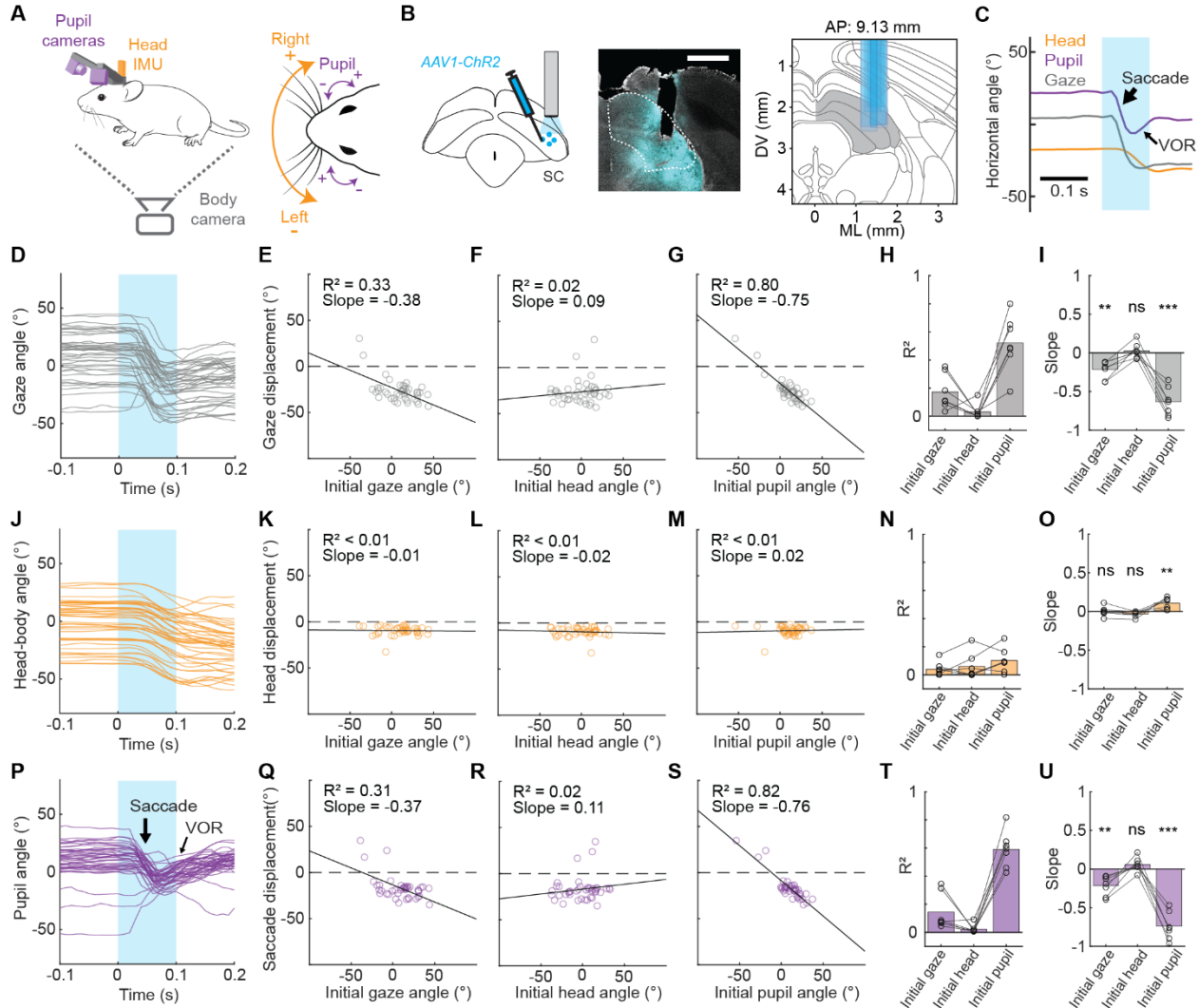


Figure 3.1: Superior colliculus specifies head displacement and saccade endpoint but not overall gaze displacement in freely moving mice

A, Left, schematic. Head-mounted cameras and inertial measurement unit (IMU) track eyes and head, respectively. Initial head-eye angle is determined using camera below transparent platform. Right, eye and head sign conventions adopted throughout this paper. **B**, Optogenetic strategy. Left, schematic. Center, sample histology. Scale bar, 1 mm. Right, fiber placements for all mice ($n = 7$) in Allen common coordinate framework (CCF). **C**, Example head, pupil, and gaze traces illustrating stimulation-evoked gaze shift. Blue bar indicates LED stimulation period. Note two distinct phases of eye motion: a fast saccadic phase coinciding with head movement onset followed by a slow phase with magnitude roughly equal and opposite to the ongoing head rotation, resembling a gaze-stabilizing reflex (vestibular ocular reflex, VOR). **D-G, J-M, P-S**, Data for example (legend continued on next page)

(legend continued from previous page)

mouse. **D**, Gaze traces aligned to LED onset. **E**, Relationship between initial gaze angle and gaze displacement. **F**, Relationship between initial head angle and gaze displacement. **G**, Relationship between initial pupil angle and gaze displacement. **H**, Population summary of R^2 values for optogenetically evoked gaze displacement linearly regressed against initial gaze, head, or pupil angles ($n = 7$ mice). **I**, As in **H** but for regression slope values. **J**, Head movement traces aligned to LED onset. **K**, Relationship between initial gaze angle and head displacement. **L**, Relationship between initial head angle and head displacement. **M**, Relationship between initial pupil angle and head displacement. **N**, Population summary of R^2 values for optogenetically evoked head displacement linearly regressed against initial gaze, head, or pupil angles ($n = 7$ mice). **O**, As in **N** but for regression slope values. **P**, Pupil traces aligned to LED onset. **Q**, Relationship between initial gaze angle and pupil displacement. **R**, Relationship between initial head angle and pupil displacement. **S**, Relationship between initial pupil angle and pupil displacement. **T**, Population summary of R^2 values for optogenetically evoked pupil displacement linearly regressed against initial gaze, head, or pupil angles ($n = 7$ mice). **U**, As in **T** but for regression slope values.

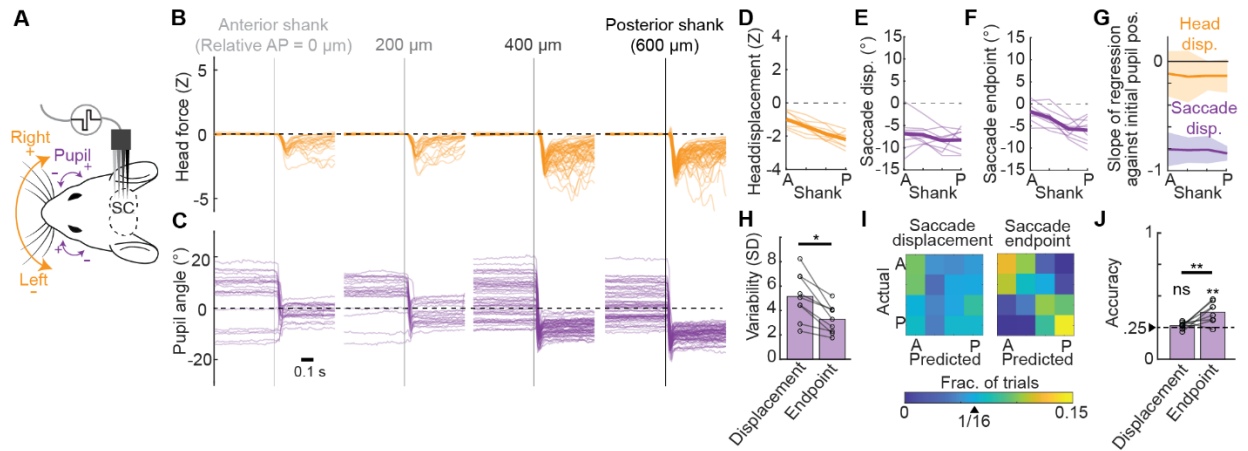


Figure 3.2: Mouse superior colliculus comprises topographic maps of head displacement and saccade endpoint

A, Schematic of electrical microstimulation in a head-fixed mouse. **B**, Attempted head movement traces aligned to stimulation onset (gray shading) for each electrode for an example animal. **C**, Pupil position traces aligned to stimulation onset for the same animal as in **B**. **D**, Population summary of attempted head displacements as a function of microstimulation site. Thin lines are data from individual animals ($n = 9$). Thick line is population mean. **E**, As in **D**, but for saccade displacements. **F**, As in **D**, **E**, but for saccade endpoint. **G**, Fraction of saccade displacement or attempted head displacement variance (R^2 , linear regression) explained by initial pupil position across animals (mean \pm SD). **H**, Variability of saccade displacements and endpoints. Each point is the mean shank-wise variance. Lines denote individual mice, bars denote population means. **I**, Confusion matrices of predicted versus actual microstimulation shank for example animal. The matrix cell values indicate the fraction of trials with that result. Chance level indicated with triangle. A, anterior. P, posterior. **J**, Summary of classifier accuracies predicting microstimulation shank using saccade displacement or endpoint. Chance level indicated with triangle and dashed line. Confusion matrix and accuracy scores are from test folds of cross-validated multinomial logistic regressions. Lines connect values for individual mice, bars are population means. Orange denotes head data and purple denotes eye data. Statistics performed using one- or two-sample Student's t-test (* $p < 0.05$; ** $p < 0.01$; *** $p < 0.001$; ns, not significant).

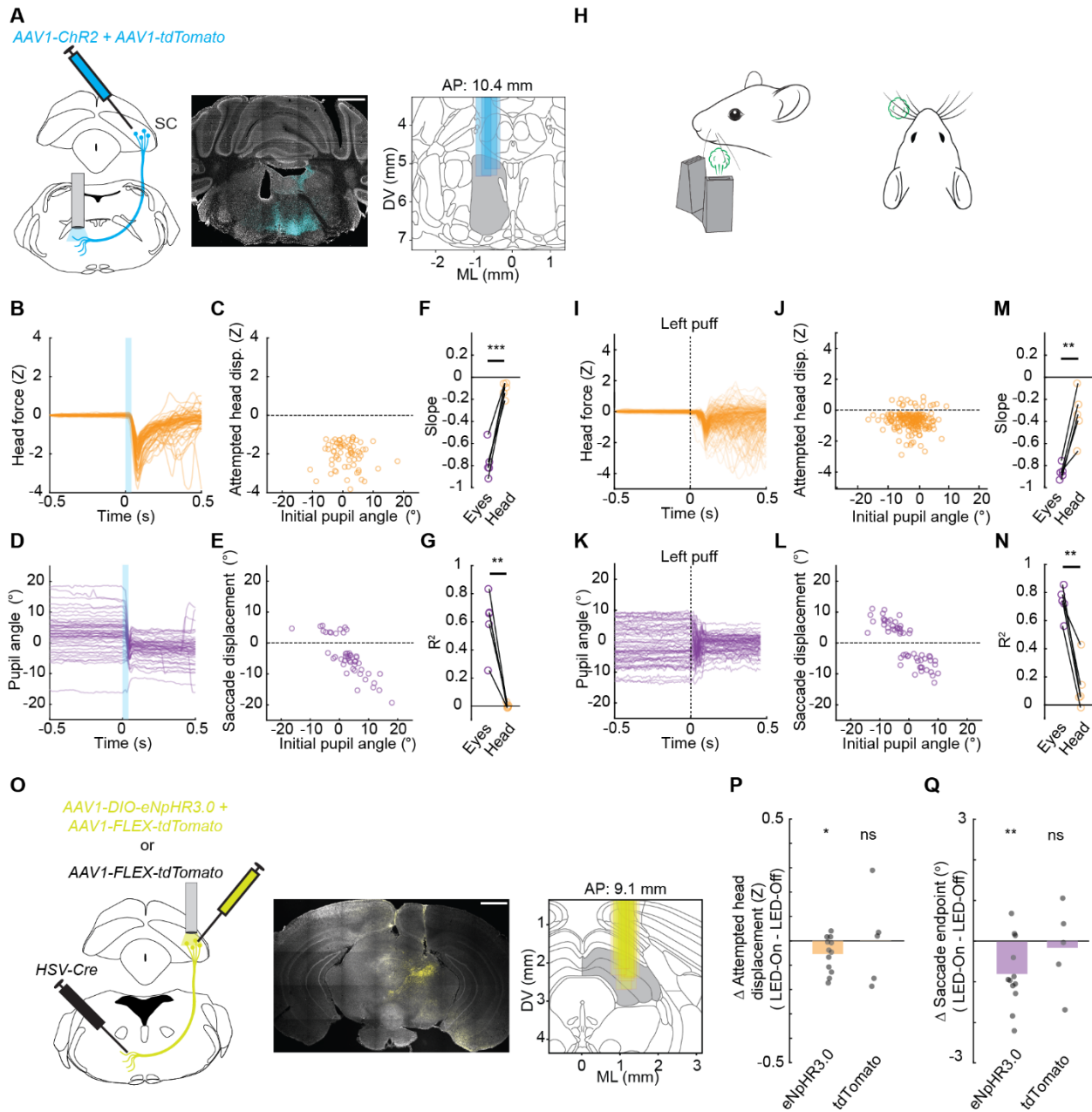


Figure 3.3: Tectoreticular neurons drive sensory-guided eye and head movements with stereotyped endpoints and displacements, respectively

A, Left, schematic illustrating strategy to selectively stimulate tectoreticular neurons in head-fixed animals ($n = 5$). Middle, sample histology in PMRF. Scale bar, 1 mm. Right, fiber placements in Allen CCF. **B**, Attempted head movement traces aligned to LED onset (blue shading) for an example animal. **C**, Relationship between initial pupil angle and attempted head displacement for traces in **B**. **D**, Pupil position traces aligned to LED onset (blue shading). **E**, Relationship between initial pupil angle and saccade displacement for traces in **D**. Data in **B-D** were derived from the same animal. **F**, (legend continued on next page)

(legend continued from previous page)

Population summary of slopes of lines of best fit for regression of head displacements and saccade displacements against initial pupil angle. **G**, As in **F** but for R^2 values. Markers in **F-G** show individual animals. **H**, Schematics illustrating airpuff stimulation of the left whisker bundle. **I**, Attempted head movement traces aligned to left whisker airpuff onset (vertical dashed line) for an example animal. **J**, Relationship between initial pupil angle and attempted head displacement for traces in **I**. **K**, Pupil position traces aligned to whisker airpuff onset (vertical dashed line). **L**, Relationship between initial pupil angle and saccade displacement for traces in **K**. Data in **I-L** were derived from the same animal. **M**, Population summary of slopes of lines of best fit for regression of airpuff-evoked head displacements and saccade displacements against initial pupil angle. **N**, As in **M** but for R^2 values. Markers in **M-N** show individual animals. **O**, Left, schematic illustrating strategy to selectively inhibit tectoreticular neurons during left whisker airpuffs. A retrogradely infecting virus encoding Cre recombinase was injected in left PMRF and Cre-dependent eNpHR3.0 was injected in right SC (n = 12 mice). An optic fiber was implanted over right SC and tectoreticular activity was suppressed in the period surrounding whisker airpuff onset on a subset of trials. To control for the effects of light, an additional group of animals was subjected to the same experimental conditions except with Cre-dependent tdTomato used in place of Cre-dependent eNpHR3.0 (n = 5 mice). Middle, sample SC histology. Scale bar, 1 mm. Right, fiber placements in Allen CCF. **P**, Change in mean attempted head displacement between LED-On and LED-Off whisker airpuff trials. **Q**, As in **P** for saccade endpoint. Orange denotes head data and purple denotes eye data. Statistics performed using Student's t-test (*p < 0.05; **p < 0.01; ***p < 0.001; ns, not significant).

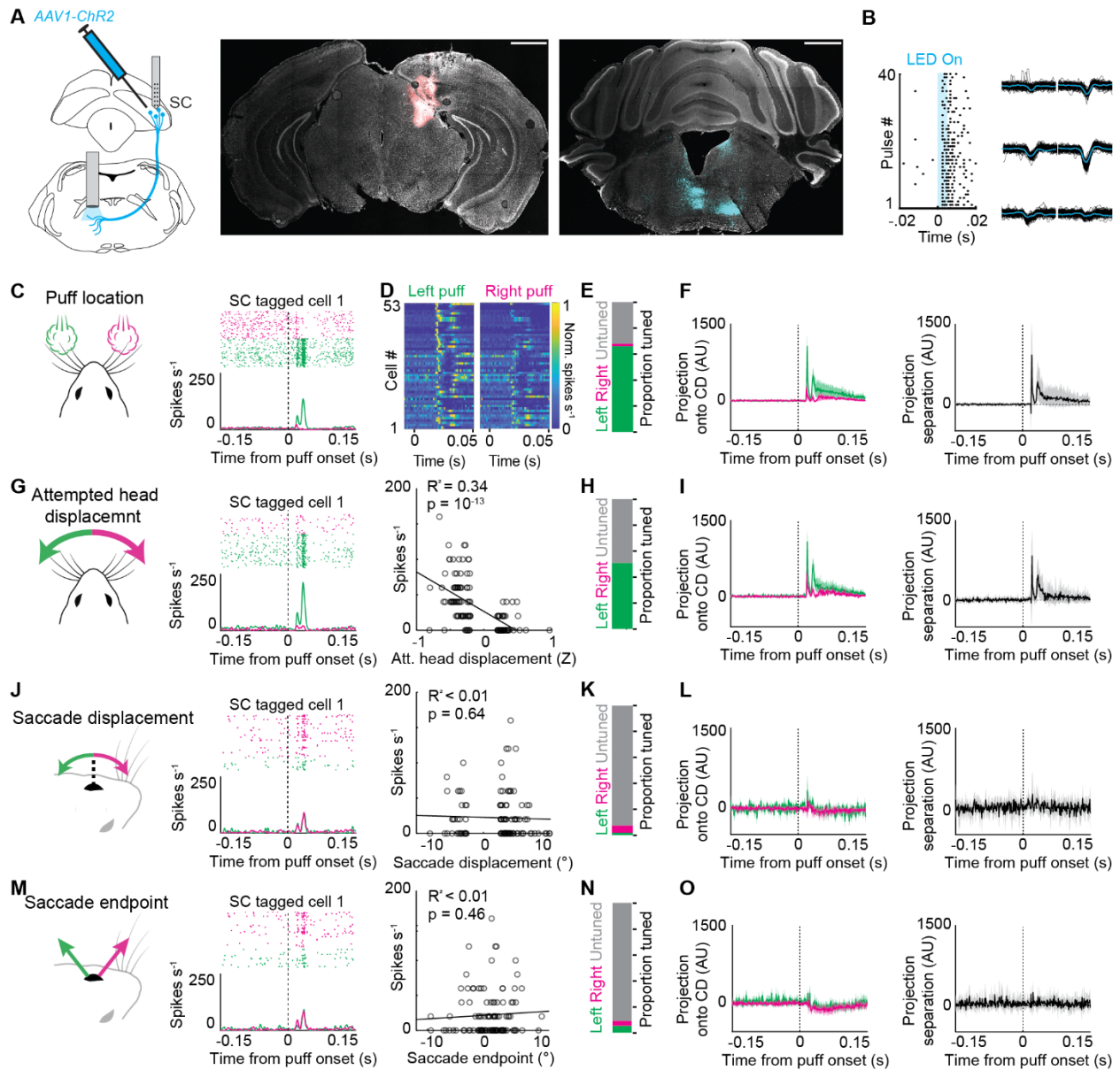


Figure 3.4: Tectoreticular neurons encode stimulus location and head displacement

A, Left, schematic of antidromic "optotagging" of tectoreticular neurons. Middle, Sample histology in SC. Right, sample histology in PMRF. Scale bar, 1 mm. **B**, Example cell. Left, raster plots of activity aligned to LED onset. Right, waveforms of spontaneously occurring (black) and light-evoked (blue) action potentials. **C**, Left, schematic of airpuff delivery to whiskers. Right, spike rasters and peri-stimulus time histogram of activity of example cell aligned to airpuff onset sorted by airpuff location. **D**, Average firing rate of each tectoreticular cell aligned to airpuff onset and normalized to its maximum response. **E**, Proportion of cells significantly tuned for left and right airpuffs. **F**, Left, trial-averaged population activity projected onto the coding dimension (CD) for left and right (*legend continued on next page*)

(legend continued from previous page)

whisker airpuffs. Right, separation between the left and right whisker airpuff activity projections. **G**, Left, schematic of left and right attempted head displacements. Middle, spike raster and peri-stimulus time histogram of activity for example cell aligned to airpuff onset sorted by attempted head displacement direction. Right, single-trial analysis of the relationship between attempted head displacement and neural activity in the 50 ms following airpuff onset for the same cell. **H**, Proportion of units significantly tuned for left and right head displacements. **I**. Left, trial-averaged population activity projected onto the coding dimension (**CD**) for left and right head displacements. Right, separation between the left and right head displacement activity projections. **J**, **M**, As in **G** for saccade displacements and saccade endpoints. **K**, **N**, As in **H** for saccade displacements and saccade endpoints. **L**, **O**, As in **I** for saccade displacements and saccade endpoints. Green and magenta denote left (contralateral to recording site) and right (ipsilateral to recording site) airpuff locations or movement parameters. Left and right saccade endpoints were defined relative to the median eye position. Tuning for left and right airpuffs was computed using Student's t-test ($p < 0.05$). Tuning for movement parameters was determined using linear regression ($p < 0.05$). The same example cell is shown each panel. Shading represents 99% confidence interval. Recordings were performed in 4 mice over 9 sessions, yielding 317 units of which 53 were identified as tectoreticular.

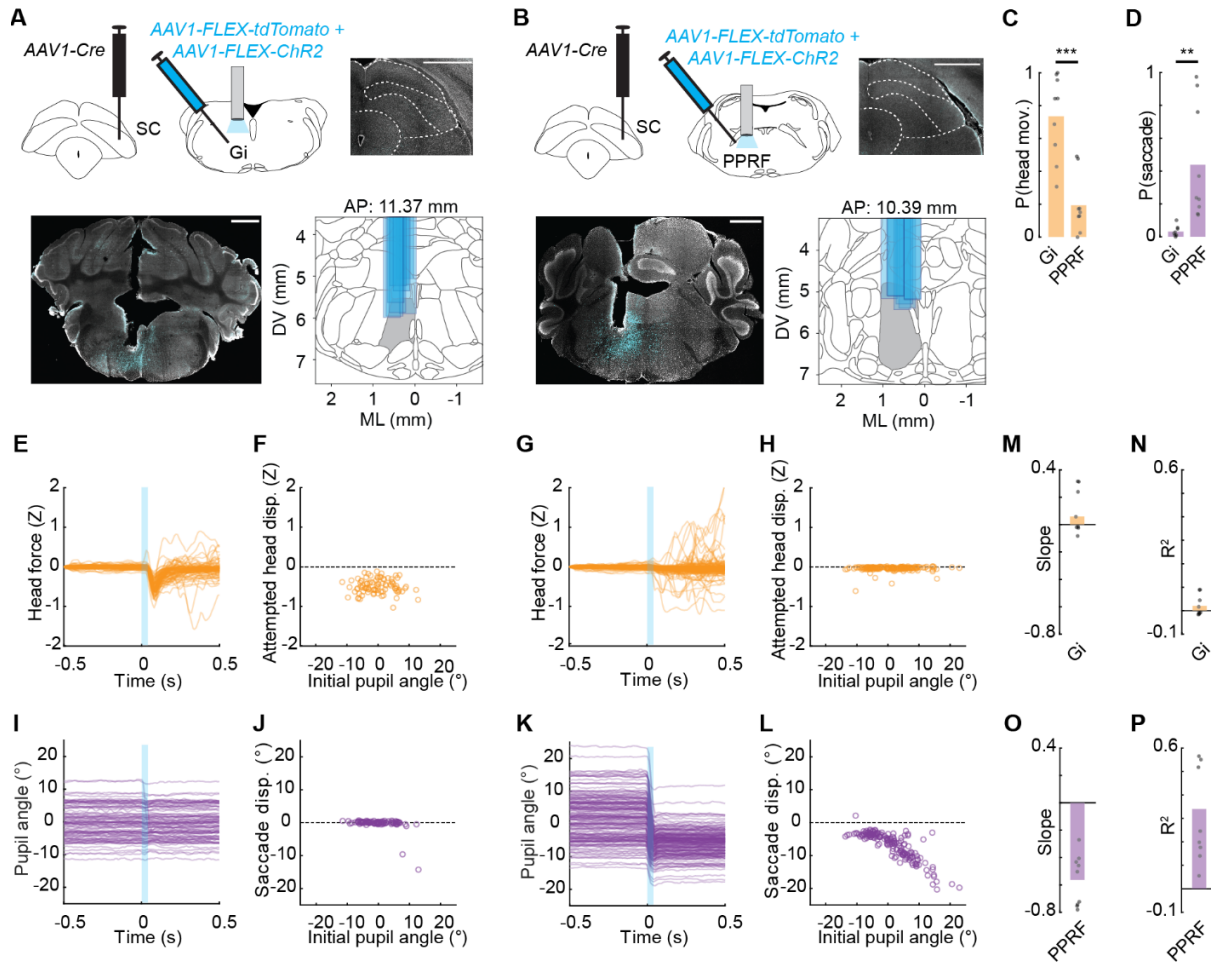


Figure 3.5: SC-recipient Gi and PPRF modules drive head movements with stereotyped displacements and saccades with stereotyped endpoints, respectively

A, Top left, schematic of anterograde labeling and stimulation approach. Top right, sample histology in SC. Bottom left, sample histology in Gi. Bottom right, fiber placements in Allen CCF. Scale bars, 1 mm. **B**, As in **A** but for SC-recipient PPRF neurons. **C**, **D**, Population summary of Gi and PPRF optogenetically evoked head movement probability (**C**) and saccade probability (**D**). **E**, Attempted head movements aligned to LED onset (blue shading) for sample Gi mouse. **F**, Relationship between initial pupil angle and head displacement for traces in **E**. **G**, **H**, as in **E**, **F** for sample PPRF mouse. **I**, Pupil traces aligned to LED onset (blue shading) for sample Gi mouse. **J**, Relationship between initial pupil angle and saccade displacement for traces in **I**. **K**, **L**, As in **I**, **J** but for SC-recipient PPRF neurons. Data in **E**, **F**, **I**, **J** derived from the same Gi stimulation animal. Data from **G**, **H**, **K**, **L** derived from the same PPRF stimulation animal. **M**, Population summary of slopes of lines of best fit for regression of Gi optogenetically evoked head displacements against initial pupil angle. **N**, As in **M** but for

(legend continued on next page)

(legend continued from previous page)

R² values. **O**, Population summary of slopes of lines of best fit for regression of PPRF optogenetically evoked saccade displacements against initial pupil angle. **P**, As in **O** but for R² values. Markers in **C**, **D**, **M-P** show individual animals (n = 9 for Gi, n = 9 for PPRF). Orange denotes head data and purple denotes eye data. Statistics performed using Student's t-test (*p < 0.05; **p < 0.01; ***p < 0.001; ns, not significant).

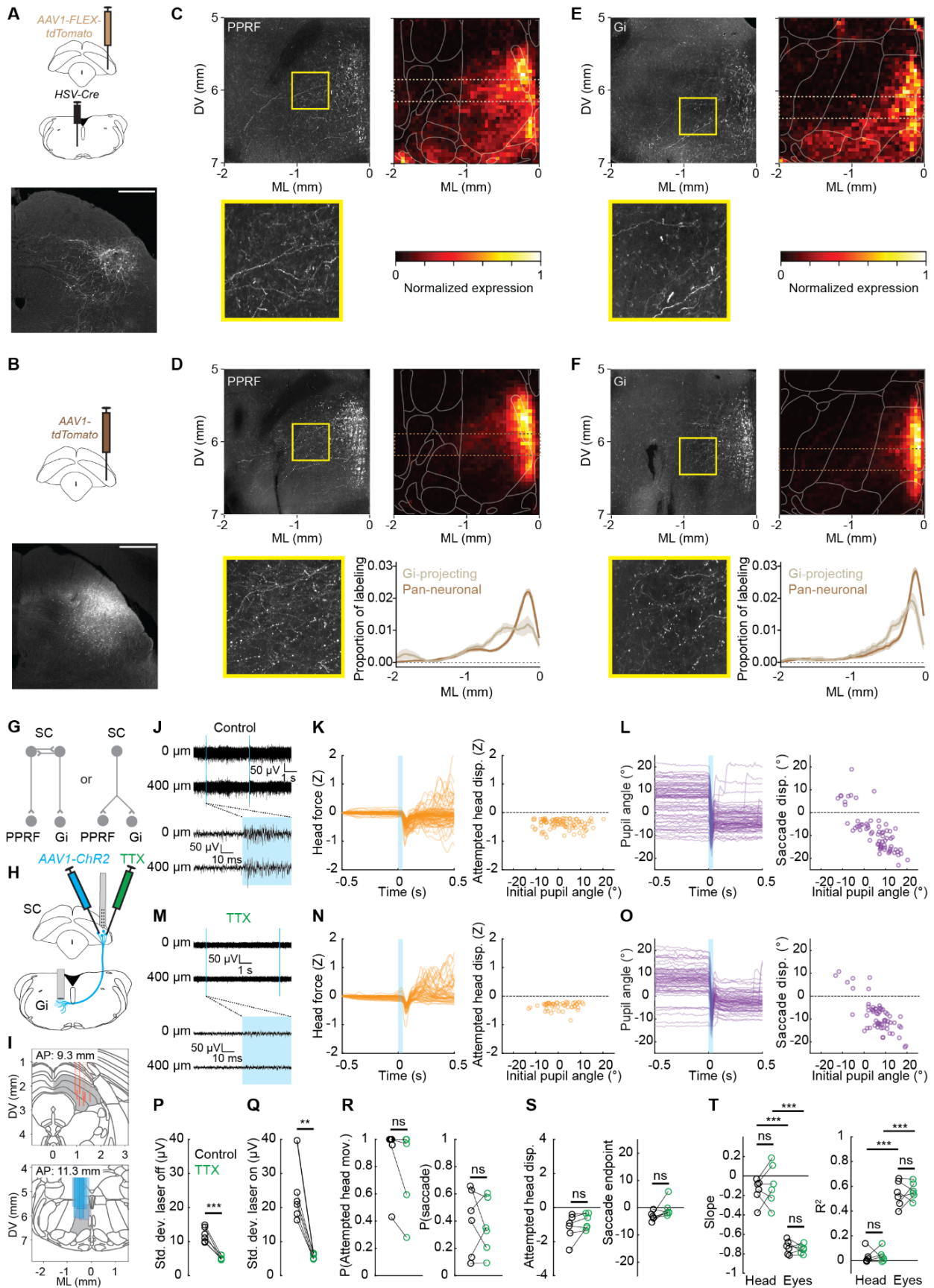


Figure 3.6: Individual tectoreticular neurons collateralizing to Gi and PPRF drive both head and eye movements

A, Top, schematic of strategy to label Gi-projecting SC neurons ($n = 3$). Bottom, representative SC histology. Scale bar, 0.5 mm. **B**, As in **A** but for pan-neuronal SC labeling ($n = 4$). **C**, Gi-projecting neurons elaborate axon terminals in PPRF. Top left, labeling in PPRF in representative animal. Yellow rectangle indicates area magnified at lower left. Top right, mean terminal density across animals. Bottom right, colormap. **D**, As in **C** for SC pan-neuronal labeling. Bottom right shows mean medial-lateral distributions of terminals in PPRF for mice with Gi-projecting SC neurons labeled ($n = 3$, light brown) and pan-neuronal SC labeling ($n = 4$, dark brown). Distributions were calculated from area outlined by dotted lines shown in the mean terminal density images. **E**, **F**, As in **C**, **D** for terminals in Gi. **G**, Schematic of possible models. Left, model wherein separate populations of neurons innervate PPRF and Gi to drive saccades and head movements, respectively. Right, model wherein single neurons collateralize to both PPRF and Gi to drive both head and eye movements. **H**, Schematic of experimental approach. *AAV1-ChR2* was injected in right SC and a fiber optic was implanted over left Gi. SC was subsequently injected with either saline or TTX and a silicon probe was used to record activity in SC. **I**, Positions of electrodes (top) and optical fibers (bottom) in Allen CCF. **J**, SC multiunit activity at 2 depths separated by 400 μ m in SC of a control (saline-injected) mouse. **K**, Attempted head movements aligned to LED onset (blue shading) (left) and relationship between initial pupil angle and head displacement (right). **L**, as in **K** for saccades. **M**, TTX injection abolishes activity in SC. **N**, **O**, as in **K**, **L** after TTX injection in SC. Data in **J-L** and **M-O** are from the same mouse on successive days. **P**, Mean standard deviation of multiunit signals detected in SC for control and TTX sessions. Markers indicate single mice; lines connect data for control and TTX sessions for each mouse. **Q**, As in **P** for antidromically evoked activity in SC. **R**, Probability of attempted head movements (left) and saccades (right) for control and TTX sessions. **S**, Size of attempted head movements (left) and saccade endpoints (right) for control and TTX sessions. **T**, Slopes (left) and R^2 (right) of linear regression of attempted head displacement and saccade displacement against initial eye position. Statistics performed using Student's t-test (* $p < 0.05$; ** $p < 0.01$; *** $p < 0.001$; ns, not significant).

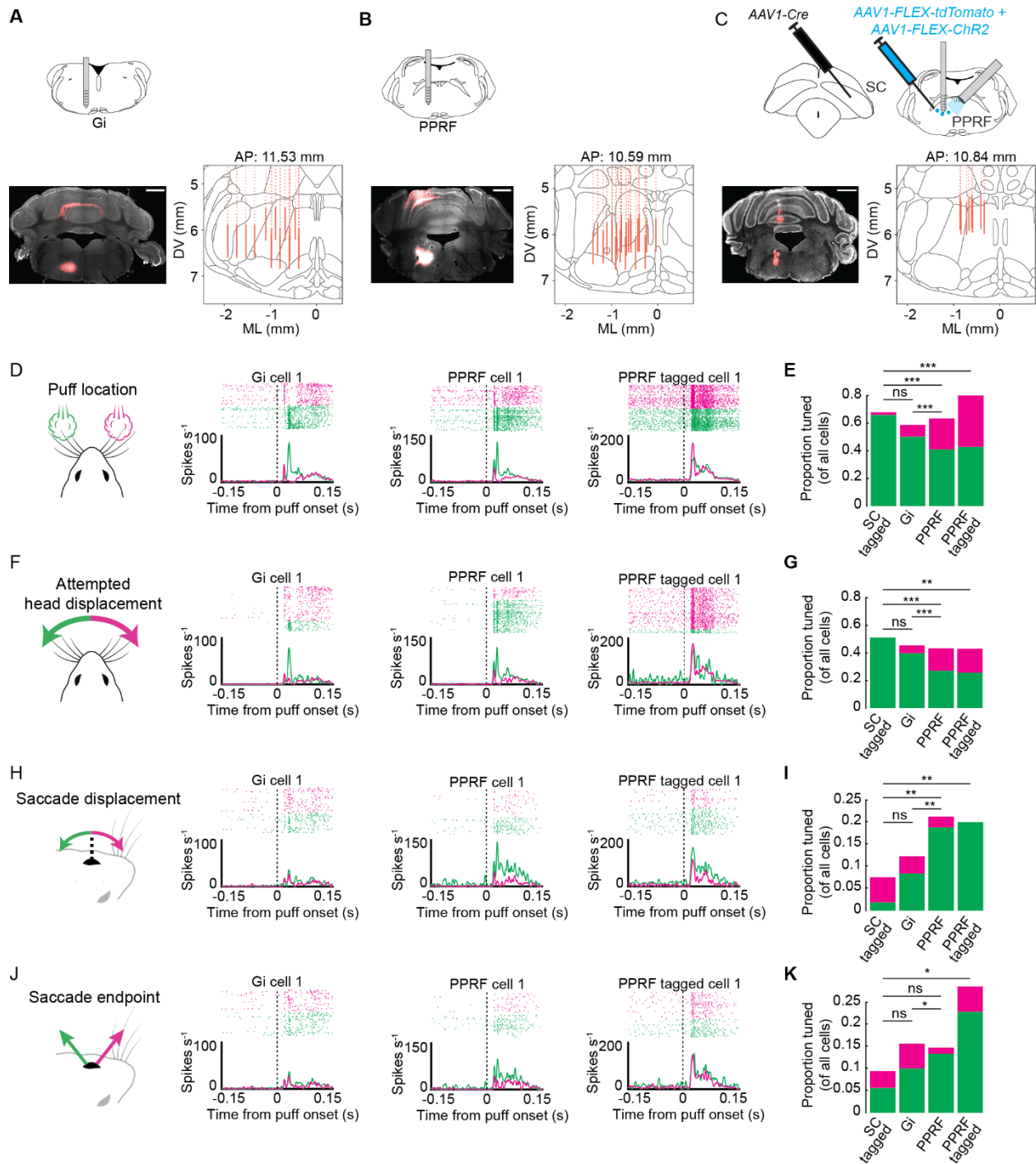


Figure 3.7: Saccade tuning emerges in PPRF

A, B, C, Top, schematics of extracellular recordings of Gi (**A**), PPRF (**B**), and optotagged SC-recipient PPRF neurons (**C**). Bottom left, sample histology of recording site. Bottom right, recording sites in Allen CCF. **D**, Responses to left and right airpuffs for example Gi (left), PPRF (middle), and optotagged SC-recipient PPRF (right) neurons. **E**, Population summaries of tuning in optotagged SC tectoreticular, Gi, PPRF, (legend continued on next page)

(legend continued from previous page)

and optotagged SC-recipient PPRF neurons. Tuning for left and right airpuffs was computed using Student's t-test ($p > 0.05$). Tuning for movement parameters was determined using linear regression ($p < 0.05$). **F-K**, as in **D, E** but for attempted head displacement (**F, G**), saccade displacement (**H, I**), and saccade endpoint (**J, K**). Each row shows a single example cell. Chi-squared tests were used to compare the proportions of left-, right-, and un-tuned units across structures (* $p < 0.05$; ** $p < 0.01$; *** $p < 0.001$; ns, not significant). Gi recordings were performed in 4 mice over 6 sessions, yielding 179 cells. PPRF recordings were performed in 6 mice over 6 sessions, yielding 292 cells. Optotagged PPRF recordings were performed in 6 mice over 9 sessions, yielding 35 cells. SC recordings are from Figure 3.2 and were performed in 4 mice over 9 sessions, yielding 53 tectoreticular cells.

3.7 SUPPLEMENTAL FIGURES

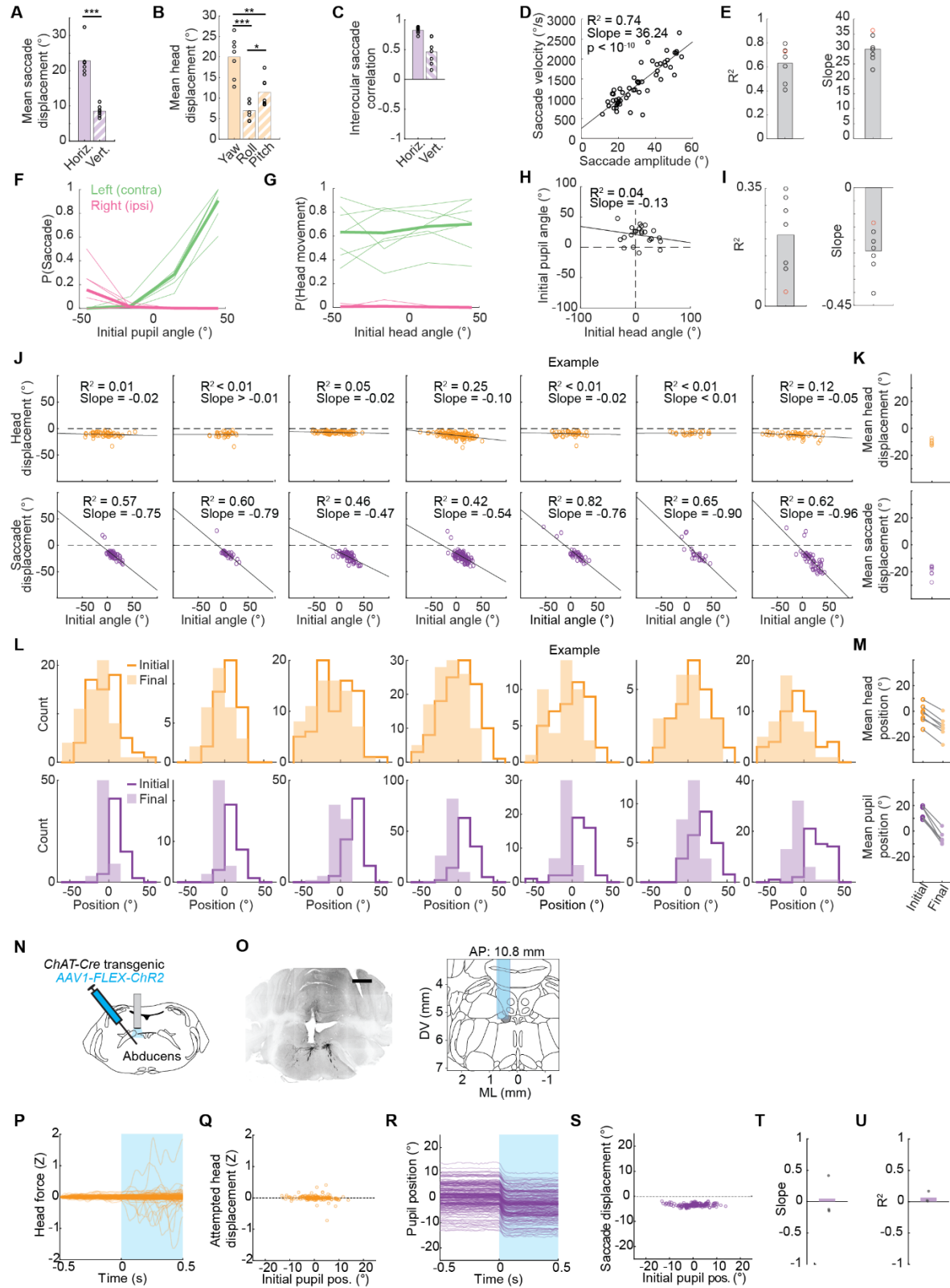


Figure S3.1: Further characterization of superior colliculus-evoked head and eye movements in freely moving mice and abducens stimulation in head-fixed mice

Data in **A-M** are from the experiment presented in Figure 3.1. **A**, Mean saccade displacement along the horizontal and vertical axes evoked by right SC stimulation. **B**, Mean head displacement along the yaw, roll, and pitch axes evoked by right SC stimulation. **C**, Pearson's correlation coefficient of evoked saccade displacements for left versus right eyes. Positive values indicate conjugate movements. **D**, Relationship between saccade amplitude and peak velocity for example animal (i.e., main sequence). **E**, Summary statistics for linear regression between saccade amplitude and peak velocity. Red markers are the example animal in **D**. **F**, Relationship between initial pupil angle and leftward (green) and rightward (magenta) saccade probability. Thick lines indicate population means. **G**, As in **F** but for relationship between head movements and initial head position. **H**, Relationship between initial head angle and initial pupil angle for example animal. **I**, Summary statistics for linear regression fits between initial head angle and initial pupil angle. Red markers are the example animal in **H**. Markers in **A-C**, **E**, **I** and thin lines in **F**, **G** represent individual mice ($n = 7$). Pairwise statistics performed using Student's t-test (* $p < 0.05$; ** $p < 0.01$; *** $p < 0.001$; ns, not significant). **J**, Relationship between head displacement and initial head-body angle (top) and initial pupil angle and saccade displacement (bottom) for all mice analyzed in Figure 3.1 ($n = 7$). **K**, Mean head (top) and saccade (bottom) displacements for each mouse. **L**, Distribution of initial (outline) and final (filled) head-body angles (top) and pupil angles (bottom) for all mice analyzed in Figure 3.1. **M**, summary of mean initial and final positions for the head (top) and eyes (bottom). **N**, Schematic illustrating strategy to selectively stimulate abducens motor neurons in head-fixed mice. *AAV1* encoding Cre-dependent ChR2 was injected in left abducens of *ChAT-Cre* transgenic mice, and a fiber was implanted over left abducens. **O**, Left, example ChR2 labeling and fiber placement. Scale bar, 1.0 mm. Right, fiber placements in Allen CCF. **P**, Attempted head movements aligned to LED onset (blue shading). **Q**, Relationship between initial pupil angle and attempted head displacement for traces in **P**. **R**, Pupil traces aligned to LED onset (blue shading) for an example animal. **S**, Relationship between initial pupil angle and saccade displacement for traces in **R**. Data in **P-S** were derived from the same animal. **T**, Population summary of slopes of lines of best fit for regression of abducens optogenetically evoked saccade displacements against initial pupil angle. **U**, As in **T** but for R^2 values. Markers in **T**, **U** show individual animals ($n = 3$). Orange denotes head data and purple denotes eye data.

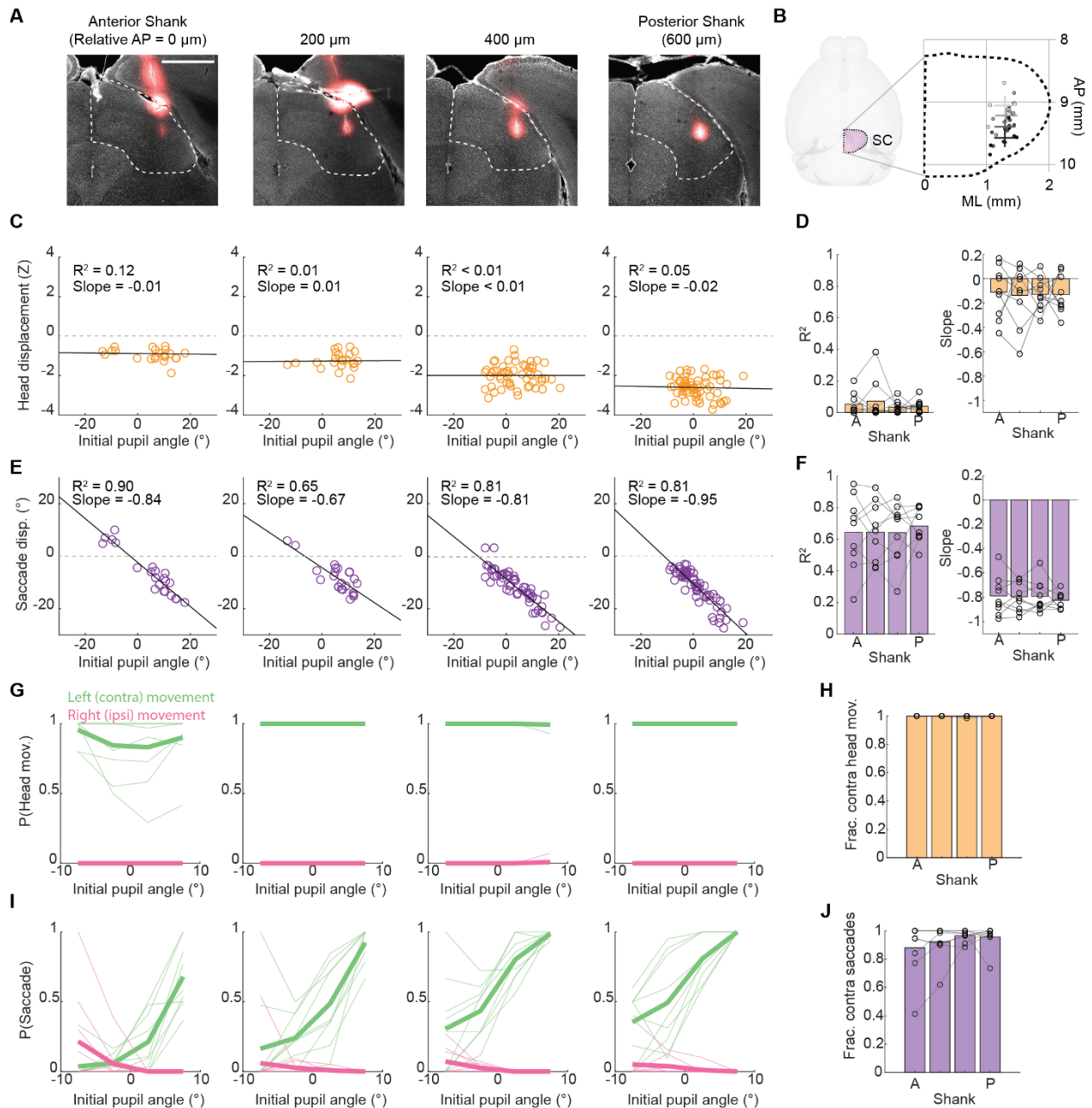


Figure S3.2: Further characterization of head and eye movements evoked by SC microstimulation along the anterior-posterior axis

A, Representative histology of shank locations (labeled with Dil) in right SC. Dashed outlines indicate borders of SC. **B**, AP and ML positions of shanks in each mouse (dots) and population means (crosshairs) in Allen CCF. **C**, Relationship between initial pupil angle and attempted head displacement across shanks for example animal. **D**, Summary statistics for linear regression between initial pupil angle and head displacement. **E**, Relationship between initial pupil angle and saccade displacement across shanks for example animal. **F**, Summary statistics for linear regression between (legend continued on next page)

(legend continued from previous page)

initial pupil angle and head displacement. **G**, Relationship between initial pupil angle and attempted head movement probability across shanks, separately analyzing leftward movements (green) and rightward movements (magenta). Dark lines indicate population means. **H**, Fraction of evoked head movements that were contralateral to stimulated SC hemisphere. **I**, Relationship between initial pupil angle and evoked saccade probability across shanks, separately analyzing leftward movements (green) and rightward movements (magenta). Dark lines indicate population means. **J**, Fraction of evoked saccades that were contralateral to stimulated SC hemisphere. Markers in **D**, **F**, **H**, and **J** and thin lines in **G**, **I** represent individual mice ($n = 9$). Orange denotes head data and purple denotes eye data.

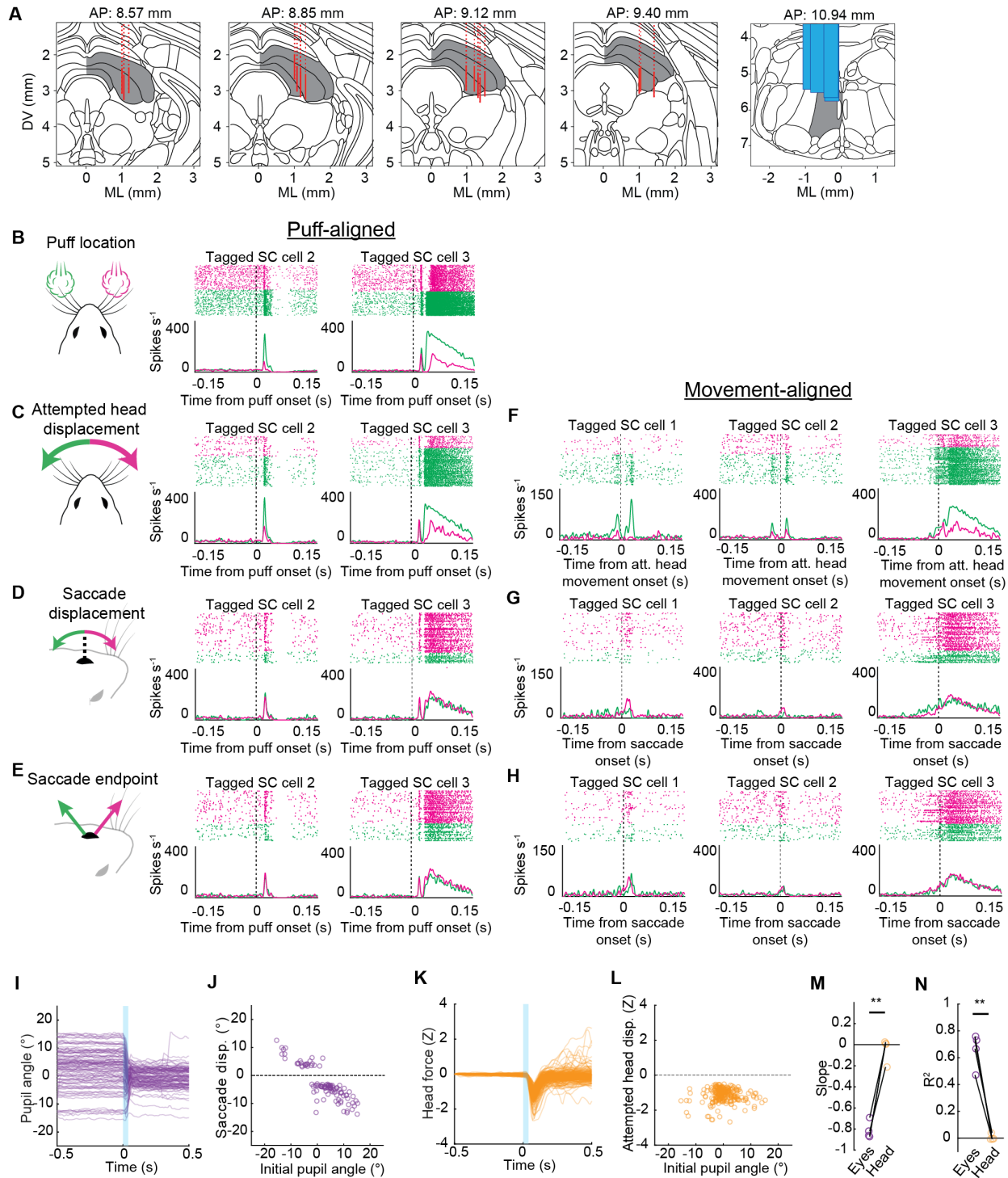


Figure S3.3: Tectoreticular recording sites and additional example cells
A, Electrode placements (solid red lines indicate recording site, dashed red lines indicate shank tracks above recording site) and fiber positions (blue) in Allen CCF. **B-E**, Puff-aligned responses of two additional tectoreticular neurons as in Figure 3.4. **F-H**, (legend continued on next page)

(legend continued from previous page)

Responses of these cells and the example cell from Figure 3.4 aligned to movement onset rather than airpuff delivery. **I-N**, Attempted head and pupil movements generated by photostimulating tectoreticular terminals in the mice used for optotagging in Figure 3.4 (n = 4 mice). **I**, Head position traces aligned to LED onset (blue shading) in an example animal. **J**, Relationship between initial pupil angle and attempted head displacement for traces in **I**. **K**, Pupil traces aligned to LED onset (blue shading). **L**, Relationship between initial pupil angle and saccade displacement for traces in **K**. Data in **I-K** were derived from the same animal. **M**, Population summary of slopes of lines of best fit for regression of tectoreticular optogenetically evoked head displacements and saccade displacements against initial pupil angle. **N**, As in **M** but for R^2 values.

Figure S3.4: Responses of tagged SC neurons to airpuffs on one side, responses of untagged SC neurons, and spatial distributions of responses within SC

A-C, Responses of the example SC cell in Figure 3.4 to airpuffs on the left side only and population summary. **D**, Puff responses for all untagged SC neurons. **E**, Population summary of response tuning in untagged SC neurons. **F**, Distribution of response tuning in intermediate SC (SCi) and deep SC (SCd). Mann-Whitney U tests were used to compare response tuning between SCi and SCd. (**p < 0.01; ns, not significant). **G-J**, Laminar distributions of tuned and/or optotagged cells in SC.

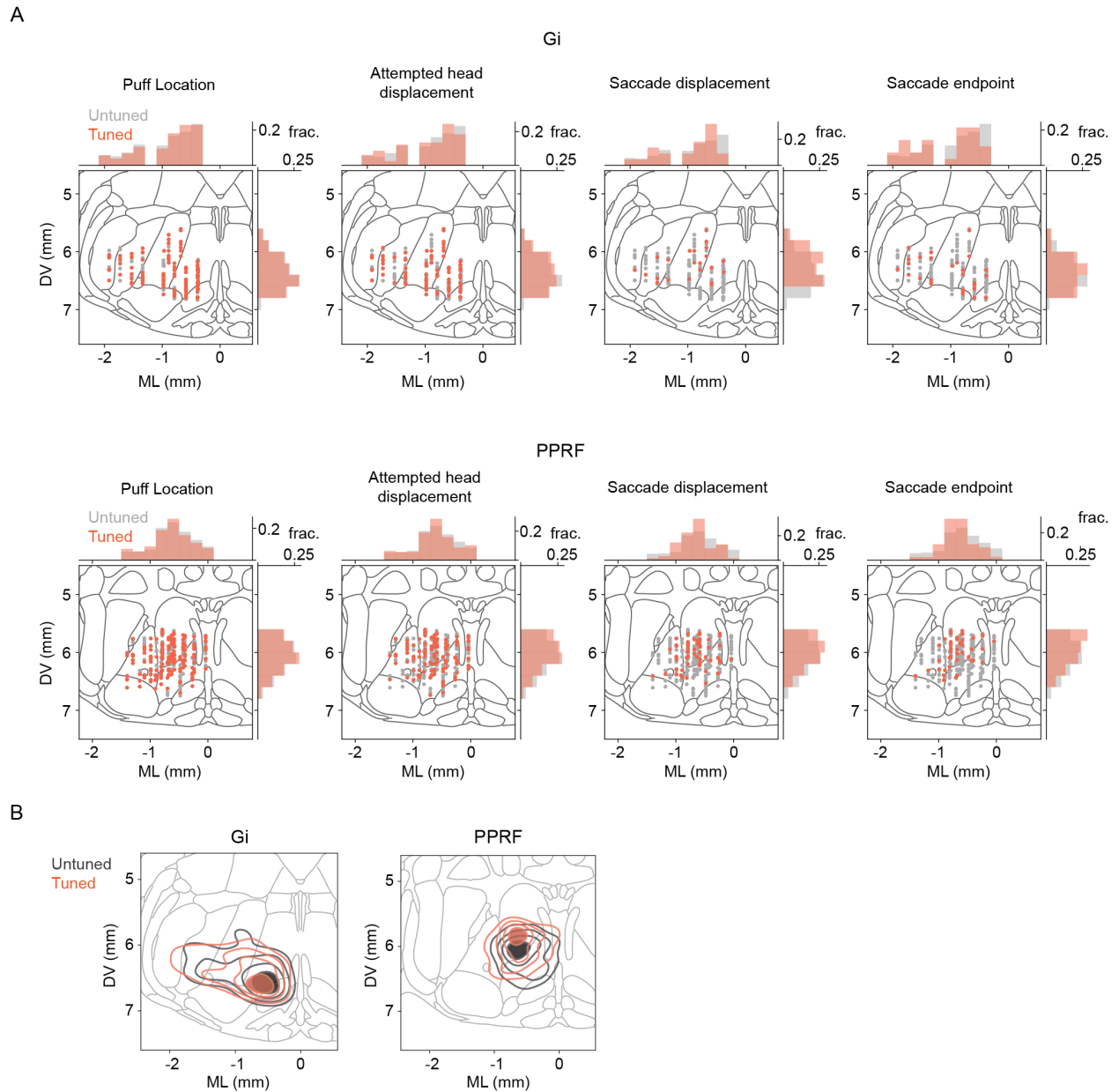


Figure S3.5: Spatial distributions of responses in Gi and PPRF

A, Locations of recorded cells in Gi (top row) and PPRF (bottom row) and response tuning for parameters measured in this study. Histograms above and below images indicate ML and DV distributions of tuned and untuned cells. **B**, Density analysis of Gi cells tuned for attempted head displacement (distance between tuned and untuned distribution medians: 71.3 mm; $p = 0.678$, permutation test) and PPRF cells tuned for saccade displacement and/or endpoint (distance between tuned and untuned distribution medians: 150.2 mm; $p = 0.007$, permutation test).

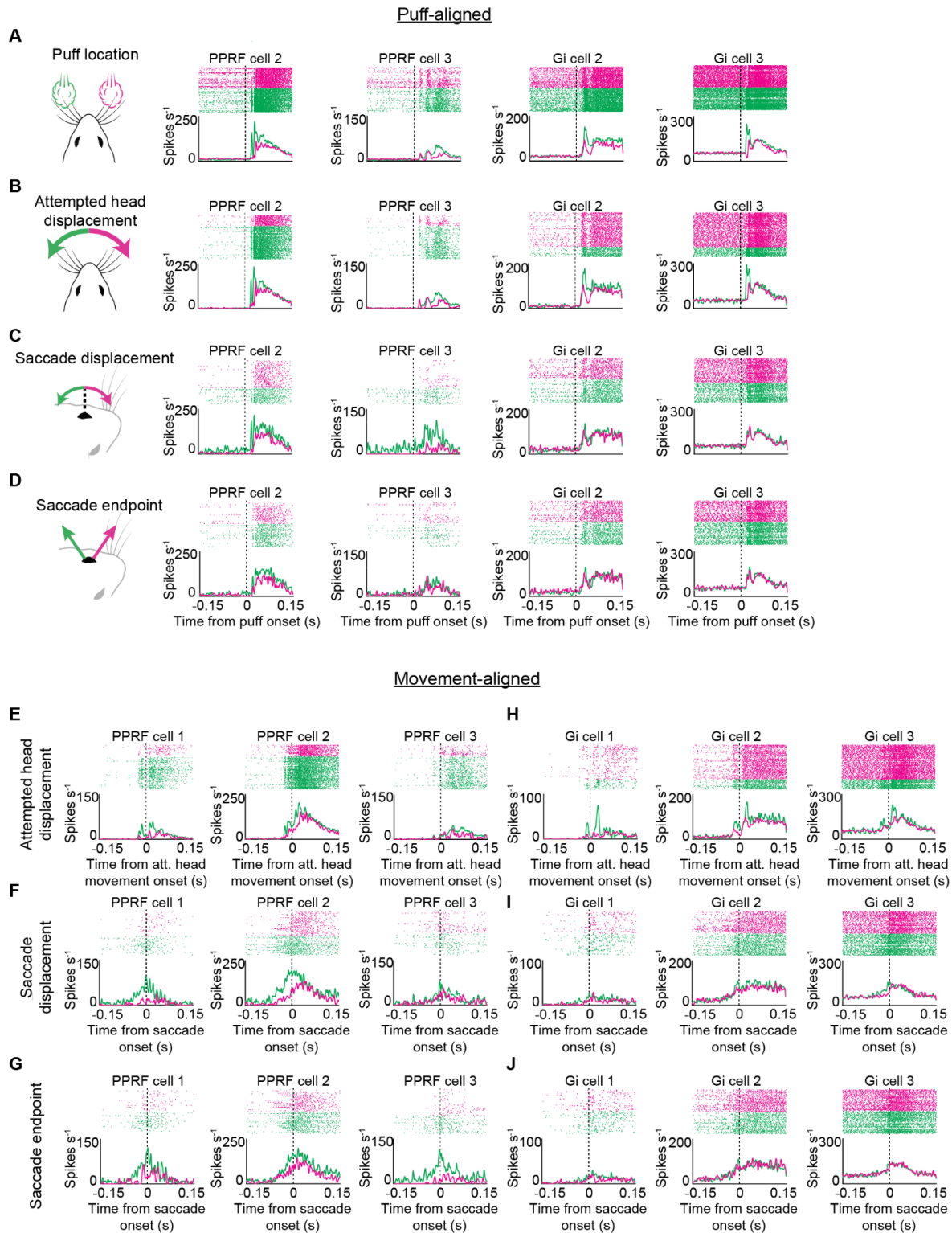


Figure S3.6: Responses of additional Gi and PPRF neurons and movement-aligned responses

A-D, Responses of 2 additional PPRF and Gi neurons as in Figure 3.7. **E-G**, Movement-aligned responses of example cells from **A-D** and Figure 3.7.

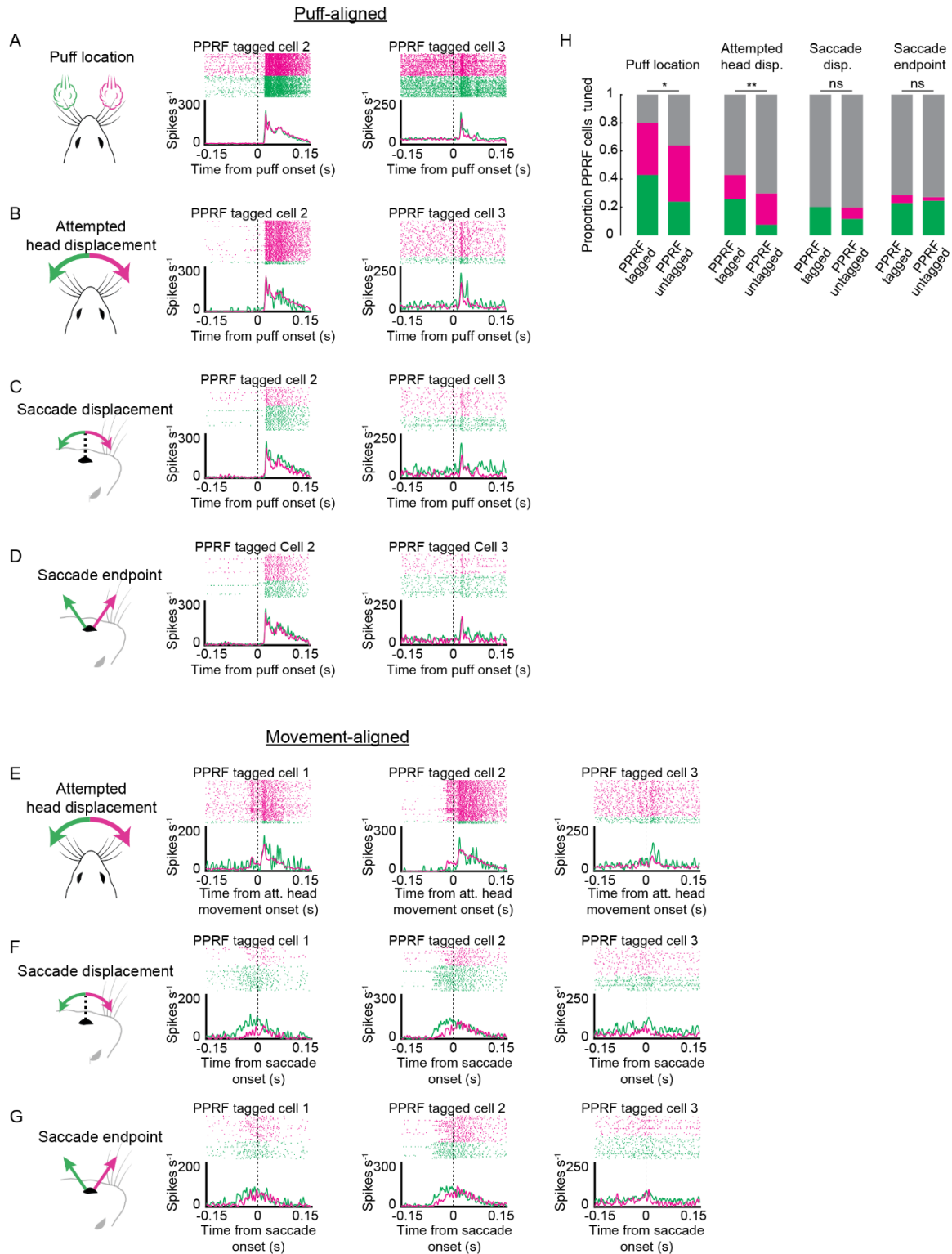


Figure S3.7: Responses of additional SC-recipient PPRF neurons and movement-aligned responses

A-D, Responses of 2 additional optotagged SC-recipient PPRF neurons as in Figure 3.7. **E-G**, Responses of example cell in Figure 3.7 and **A-D** aligned to movement onset.

3.8 REFERENCES

- Arber, S., and Costa, R.M. (2022). Networking brainstem and basal ganglia circuits for movement. *Nat. Rev. Neurosci.* 23, 342–360.
- Bergeron, A., Matsuo, S., and Guitton, D. (2003). Superior colliculus encodes distance to target, not saccade amplitude, in multi-step gaze shifts. *Nat. Neurosci.* 2003 6, 404–413.
- Bizzi, E., Kalil, R., and Tagliasco, V. (1971). Eye-head coordination in monkeys: evidence for centrally patterned organization. *Science* 173, 452–454.
- Bizzi, E., Kalil, R.E., and Morasso, P. (1972). Two modes of active eye-head coordination in monkeys. *Brain Res.* 40, 45–48.
- Bizzi, E., Giszter, S.F., Loeb, E., Mussa-Ivaldi, F.A., and Saltiel, P. (1995). Modular organization of motor behavior in the frog's spinal cord. *Trends Neurosci.* 18, 442–446.
- Bouvier, J., Caggiano, V., Leiras, R., Caldeira, V., Bellardita, C., Balueva, K., Fuchs, A., and Kiehn, O. (2015). Descending Command Neurons in the Brainstem that Halt Locomotion. *Cell* 163, 1191.
- Castro-Alamancos, M., and Favero, M. (2016). Whisker-related afferents in superior colliculus. *J Neurophysiol* 115, 2265–2279.
- Chimoto, S., Iwamoto, Y., Shimazu, H., and Yoshida, K. (1996). Monosynaptic activation of medium-lead burst neurons from the superior colliculus in the alert cat. *J. Neurophysiol.* 75, 2658–2661.

- Claudi, F., Tyson, A.L., Petrucco, L., Margrie, T.W., Portugues, R., and Branco, T. (2021). Visualizing anatomically registered data with brainrender. *Elife* 10.
- Cregg, J.M., Leiras, R., Montalant, A., Wanken, P., Wickersham, I.R., and Kiehn, O. (2020). Brainstem neurons that command mammalian locomotor asymmetries. *Nat. Neurosci.* 2020 236 23, 730–740.
- D’Avella, A., Saltiel, P., and Bizzi, E. (2003). Combinations of muscle synergies in the construction of a natural motor behavior. *Nat. Neurosci.* 6, 300–308.
- Diedrichsen, J., Shadmehr, R., and Ivry, R.B. (2010). The coordination of movement: optimal feedback control and beyond. *Trends Cogn. Sci.* 14, 31–39.
- Dudman, J.T., and Krakauer, J.W. (2016). The basal ganglia: From motor commands to the control of vigor. *Curr. Opin. Neurobiol.* 37, 158–166.
- Evans, D.A., Stempel, A.V., Vale, R., Ruehle, S., Lefler, Y., and Branco, T. (2018). A synaptic threshold mechanism for computing escape decisions. *Nature* 558, 590–594.
- Ferreira-Pinto, M.J., Kanodia, H., Falasconi, A., Sigrist, M., Esposito, M.S., and Arber, S. (2021). Functional diversity for body actions in the mesencephalic locomotor region. *Cell* 184, 4564-4578.e18.
- Freedman, E.G. (2008). Coordination of the Eyes and Head during Visual Orienting. *Exp. Brain Res.* 190, 369.
- Freedman, E., and Sparks, D. (1997). Eye-head coordination during head-unrestrained gaze shifts in rhesus monkeys. *J. Neurophysiol.* 77, 2328–2348.

- Freedman, E., Stanford, T., and Sparks, D. (1996a). Combined eye-head gaze shifts produced by electrical stimulation of the superior colliculus in rhesus monkeys. *J. Neurophysiol.* 76, 927–952.
- Freedman, E.G., Stanford, T.R., and Sparks, D.L. (1996b). Combined eye-head gaze shifts produced by electrical stimulation of the superior colliculus in rhesus monkeys. *J. Neurophysiol.* 76, 927–952.
- Gandhi, N.J., and Katnani, H.A. (2011). Motor Functions of the Superior Colliculus. *Annu. Rev. Neurosci.* 34, 205–231.
- Gandhi, N.J., Barton, E.J., and Sparks, D.L. (2008). Coordination of eye and head components of movements evoked by stimulation of the paramedian pontine reticular formation. *Exp. Brain Res.* 189, 35–47.
- Gioia, M., and Bianchi, R. (1992). Intrinsic Organization of the Paramedian Pontine Reticular Formation of the Cat. *Cells Tissues Organs* 144, 127–134.
- Gradinaru, V., Zhang, F., Ramakrishnan, C., Mattis, J., Prakash, R., Diester, I., Goshen, I., Thompson, K.R., and Deisseroth, K. (2010). Molecular and Cellular Approaches for Diversifying and Extending Optogenetics. *Cell* 141, 154–165.
- Grantyn, A., Moschovakis, A.K., and Kitama, T. (2004). Control of orienting movements: role of multiple tectal projections to the lower brainstem. *Prog. Brain Res.* 143, 423–438.
- Graziano, M.S.A., and Aflalo, T.N. (2007). Mapping Behavioral Repertoire onto the Cortex. *Neuron* 56, 239–251.

- Graziano, M.S.A., Taylor, C.S.R., and Moore, T. (2002). Complex movements evoked by microstimulation of precentral cortex. *Neuron* 34, 841–851.
- Gui-ton, D. (1992). Control of eye-head coordination during orienting gaze shifts. *Trends Neurosci.* 15, 174–179.
- Guo, J.Z., Graves, A.R., Guo, W.W., Zheng, J., Lee, A., Rodríguez-González, J., Li, N., Macklin, J.J., Phillips, J.W., Mensh, B.D., et al. (2015). Cortex commands the performance of skilled movement. *Elife* 4.
- Hooks, B.M., Papale, A.E., Paletzki, R.F., Feroze, M.W., Eastwood, B.S., Couey, J.J., Winnubst, J., Chandrashekar, J., and Gerfen, C.R. (2018). Topographic precision in sensory and motor corticostriatal projections varies across cell type and cortical area. *Nat. Commun.* 9.
- Hoy, J.L., Bishop, H.I., and Niell, C.M. (2019). Defined Cell Types in Superior Colliculus Make Distinct Contributions to Prey Capture Behavior in the Mouse. *Curr. Biol.* 29, 4130-4138.e5.
- Isa, K., Sooksawate, T., Kobayashi, K., Kobayashi, K., Redgrave, P., and Isa, T. (2020). Dissecting the Tectal Output Channels for Orienting and Defense Responses. *ENeuro* 7, 1–18.
- Isa, T., Marquez-Legorreta, E., Grillner, S., and Scott, E.K. (2021). The tectum/superior colliculus as the vertebrate solution for spatial sensory integration and action. *Curr. Biol.* 31, R741–R762.

- Kandel, E.R., Schwartz, J.H., Jessell, T.M., Siegelbaum, S.A., and Hudspeth, A.J. (2013). *Principles of Neural Science, Fifth Edition* | Neurology Collection | McGraw-Hill Medical.
- Kawato, M. (1999). Internal models for motor control and trajectory planning. *Curr. Opin. Neurobiol.* 9, 718–727.
- Keizer, K., and Kuypers, H.G.J.M. (1989). Distribution of corticospinal neurons with collaterals to the lower brain stem reticular formation in monkey (*Macaca fascicularis*). *Exp. Brain Res.* 1989 742 74, 311–318.
- Keller, E.L., McPeck, R.M., and Salz, T. (2000). Evidence against direct connections to PPRF EBNs from SC in the monkey. 84, 1303–1313.
- Khan, S.I., Della Santina, C.C., and Migliaccio, A.A. (2019). Angular vestibuloocular reflex responses in *otop1* mice. I. otolith sensor input is essential for gravity context-specific adaptation. *J. Neurophysiol.* 121, 2291–2299.
- Kita, T., and Kita, H. (2012). The subthalamic nucleus is one of multiple innervation sites for long-range corticofugal axons: a single-axon tracing study in the rat. *J. Neurosci.* 32, 5990–5999.
- Knudsen, E.I. (1989). Fused binocular vision is required for development of proper eye alignment in barn owls. *Vis. Neurosci.* 2, 35–40.
- Komiyama, T., Sato, T.R., Oconnor, D.H., Zhang, Y.X., Huber, D., Hooks, B.M., Gabbito, M., and Svoboda, K. (2010). Learning-related fine-scale specificity imaged in motor cortex circuits of behaving mice. *Nature* 464, 1182–1186.

- Krubitzer, L.A., and Prescott, T.J. (2018). The Combinatorial Creature: Cortical Phenotypes within and across Lifetimes. *Trends Neurosci.* 41, 744–762.
- Land, M.F. (2019). The Evolution of Gaze Shifting Eye Movements. In *Current Topics in Behavioral Neurosciences*, (Springer), pp. 3–11.
- Land, M.F., and Nilsson, D.-E. (2012). *Animal Eyes* (Oxford University Press).
- Lemon, R.N. (2008). Descending pathways in motor control. *Annu. Rev. Neurosci.* 31, 195–218.
- Li, N., Daie, K., Svoboda, K., and Druckmann, S. (2016). Robust neuronal dynamics in premotor cortex during motor planning. *Nat.* 2016 5327600 532, 459–464.
- Lima, S.Q., Hromádka, T., Znamenskiy, P., and Zador, A.M. (2009). PINP: A New Method of Tagging Neuronal Populations for Identification during In Vivo Electrophysiological Recording. *PLoS One* 4, 6099.
- Lin, D., Boyle, M.P., Dollar, P., Lee, H., Lein, E.S., Perona, P., and Anderson, D.J. (2011). Functional identification of an aggression locus in the mouse hypothalamus. *Nature* 470, 221.
- Masullo, L., Mariotti, L., Alexandre, N., Freire-Pritchett, P., Boulanger, J., and Tripodi, M. (2019). Genetically Defined Functional Modules for Spatial Orienting in the Mouse Superior Colliculus. *Curr. Biol.* 29.
- Mathis, A., Mamidanna, P., Cury, K.M., Abe, T., Murthy, V.N., Mathis, M.W., and Bethge, M. (2018). DeepLabCut: markerless pose estimation of user-defined body parts with deep learning. *Nat. Neurosci.* 21, 1281–1289.

- Merel, J., Botvinick, M., and Wayne, G. (2019). Hierarchical motor control in mammals and machines. *Nat. Commun.* 2019 101 10, 1–12.
- Meyer, A.F., Poort, J., O’Keefe, J., Sahani, M., and Linden, J.F. (2018). A Head-Mounted Camera System Integrates Detailed Behavioral Monitoring with Multichannel Electrophysiology in Freely Moving Mice. *Neuron* 100, 46-60.e7.
- Meyer, A.F., O’Keefe, J., and Poort, J. (2020). Two Distinct Types of Eye-Head Coupling in Freely Moving Mice. *Curr. Biol.* 30, 2116-2130.e6.
- Miall, R.C., and Wolpert, D.M. (1996). Forward models for physiological motor control. *Neural Networks* 9.
- Michaieł, A.M., Abe, E.T., and Niell, C.M. (2020). Dynamics of gaze control during prey capture in freely moving mice. *Elife* 9.
- Moschovakis, A.K., Karabelas, A.B., and Highstein, S.M. (1988a). Structure-function relationships in the primate superior colliculus. II. Morphological identity of presaccadic neurons. *J. Neurophysiol.* 60, 263–302.
- Moschovakis, A.K., Karabelas, A.B., and Highstein, S.M. (1988b). Structure-function relationships in the primate superior colliculus. I. Morphological classification of efferent neurons. *J. Neurophysiol.* 60, 232–262.
- Nelson, A., Abdelmesih, B., and Costa, R.M. (2021). Corticospinal populations broadcast complex motor signals to coordinated spinal and striatal circuits. *Nat. Neurosci.* 2021 2412 24, 1721–1732.

- Neve, R.L., Neve, K.A., Nestler, E.J., and William A. Carlezon, J. (2018). Use of herpes virus amplicon vectors to study brain disorders. *Biotechniques* 39, 381–389.
- Oommen, B.S., and Stahl, J.S. (2008). Eye orientation during static tilts and its relationship to spontaneous head pitch in the laboratory mouse. *Brain Res.* 1193, 57–66.
- Overduin, S.A., d’Avella, A., Carmena, J.M., and Bizzi, E. (2012). Microstimulation Activates a Handful of Muscle Synergies. *Neuron* 76, 1071–1077.
- Pachitariu, M., Sridhar, S., and Stringer, C. (2023). Solving the spike sorting problem with Kilosort. *BioRxiv* 2023.01.07.523036.
- Paré, M., Crommelinck, M., and Guitton, D. (1994). Gaze shifts evoked by stimulation of the superior colliculus in the head-free cat conform to the motor map but also depend on stimulus strength and fixation activity. *Exp. Brain Res.* 101, 123–139.
- Park, J., Coddington, L.T., and Dudman, J.T. (2020). Basal Ganglia Circuits for Action Specification. <https://doi.org/10.1146/annurev-neuro-070918-050452> 43, 485–507.
- Payne, H.L., and Raymond, J.L. (2017). Magnetic eye tracking in mice. *Elife* 6.
- Peters, A.J., Liu, H., and Komiyama, T. (2017). Learning in the Rodent Motor Cortex. <https://doi.org/10.1146/annurev-neuro-072116-031407> 40, 77–97.
- Redgrave, P., Mitchell, I.J., and Dean, P. (1987). Descending projections from the superior colliculus in rat: a study using orthograde transport of wheatgerm-agglutinin conjugated horseradish peroxidase. *Exp. Brain Res.* 68, 147–167.

- Rossi, J., Balthasar, N., Olson, D., Scott, M., Berglund, E., Lee, C.E., Choi, M.J., Lauzon, D., Lowell, B.B., and Elmquist, J.K. (2011). Melanocortin-4 receptors expressed by cholinergic neurons regulate energy balance and glucose homeostasis. *Cell Metab.* 13, 195–204.
- Ruder, L., and Arber, S. (2019). Brainstem Circuits Controlling Action Diversification. *Annu. Rev. Neurosci.* 42, 485–504.
- Ruder, L., Schina, R., Kanodia, H., Valencia-Garcia, S., Pivetta, C., and Arber, S. (2021). A functional map for diverse forelimb actions within brainstem circuitry. *Nature* 590, 445–450.
- Sajad, A., Sadeh, M., and Crawford, J.D. (2020). Spatiotemporal transformations for gaze control. *Physiol. Rep.* 8.
- Sakatani, T., and Isa, T. (2007). Quantitative analysis of spontaneous saccade-like rapid eye movements in C57BL/6 mice. *Neurosci. Res.* 58, 324–331.
- Schiller, P.H., and Stryker, M. (1972). Single-unit recording and stimulation in superior colliculus of the alert rhesus monkey. *J. Neurophysiol.* 35, 915–924.
- Schwenkgrub, J., Harrell, E.R., Bathellier, B., and Bouvier, J. (2020). Deep imaging in the brainstem reveals functional heterogeneity in V2a neurons controlling locomotion. *Sci. Adv.* 6.
- Scudder, C.A., Kaneko, C.R., and Fuchs, A.F. (2002). The brainstem burst generator for saccadic eye movements: A modern synthesis. *Exp. Brain Res.* 142, 439–462.

- Shamash, P., Carandini, M., Harris, K., and Steinmetz, N. (2018). A tool for analyzing electrode tracks from slice histology. *BioRxiv* 447995.
- Shang, C., Liu, A., Li, D., Xie, Z., Chen, Z., Huang, M., Li, Y., Wang, Y., Shen, W.L., and Cao, P. (2019a). A subcortical excitatory circuit for sensory-triggered predatory hunting in mice. *Nat. Neurosci.* 22, 909–920.
- Shang, C., Liu, A., Li, D., Xie, Z., Chen, Z., Huang, M., Li, Y., Wang, Y., Shen, W.L., and Cao, P. (2019b). A subcortical excitatory circuit for sensory-triggered predatory hunting in mice. *Nat. Neurosci.* 22, 909–920.
- Shenoy, K. V., Sahani, M., and Churchland, M.M. (2013). Cortical Control of Arm Movements: A Dynamical Systems Perspective. [Http://Dx.Doi.Org/10.1146/Annurev-Neuro-062111-150509](http://dx.doi.org/10.1146/annurev-neuro-062111-150509) 36, 337–359.
- Sherman, S.M. (2007). The thalamus is more than just a relay. *Curr. Opin. Neurobiol.* 17, 417–422.
- Sparks, D.L., Barton, E.J., Gandhi, N.J., and Nelson, J. (2002). Studies of the role of the paramedian pontine reticular formation in the control of head-restrained and head-unrestrained gaze shifts. *Ann. N. Y. Acad. Sci.* 956, 85–98.
- Stahl, J.S., Thumser, Z.C., May, P.J., Andrade, F.H., Anderson, S.R., and Dean, P. (2015). Mechanics of mouse ocular motor plant quantified by optogenetic techniques. *J. Neurophysiol.* 114, 1455–1467.
- Steinmetz, N.A., Aydin, C., Lebedeva, A., Okun, M., Pachitariu, M., Bauza, M., Beau, M., Bhagat, J., Böhm, C., Broux, M., et al. (2021). Neuropixels 2.0: A

miniaturized high-density probe for stable, long-term brain recordings. *Science* 372.

Strick, P.L., Dum, R.P., and Rathelot, J.A. (2021). The Cortical Motor Areas and the Emergence of Motor Skills: A Neuroanatomical Perspective.

<https://doi.org/10.1146/annurev-neuro-070918-050216> 44, 425–447.

Takahashi, M., Sugiuchi, Y., Izawa, Y., and Shinoda, Y. (2005). Commissural excitation and inhibition by the superior colliculus in tectoreticular neurons projecting to omnipause neuron and inhibitory burst neuron regions. *J. Neurophysiol.* 94, 1707–1726.

Todorov, E. (2004). Optimality principles in sensorimotor control. *Nat. Neurosci.* 7, 907–915.

Todorov, E., and Jordan, M.I. (2002). Optimal feedback control as a theory of motor coordination.

Ugolini, G., and Kuypers, H.G.J.M. (1986). Collaterals of corticospinal and pyramidal fibres to the pontine grey demonstrated by a new application of the fluorescent fibre labelling technique. *Brain Res.* 365, 211–227.

Usseglio, G., Gatier, E., Heuzé, A., Hérent, C., and Bouvier, J. (2020). Control of Orienting Movements and Locomotion by Projection-Defined Subsets of Brainstem V2a Neurons. *Curr. Biol.* 30, 4665-4681.e6.

- Wallace, D.J., Greenberg, D.S., Sawinski, J., Rulla, S., Notaro, G., and Kerr, J.N.D. (2013). Rats maintain an overhead binocular field at the expense of constant fusion. *Nature* 498, 65–69.
- Wang, L., Liu, M., Segraves, M.A., and Cang, J. (2015). Visual experience is required for the development of eye movement maps in the mouse superior colliculus. *J. Neurosci.* 35, 12281–12286.
- Wang, X., Liu, Y., Li, X., Zhang, Z., Yang, H., Zhang, Y., Williams, P.R., Alwahab, N.S.A., Kapur, K., Yu, B., et al. (2017). Deconstruction of corticospinal circuits for goal-directed motor skills. *Cell* 171, 440.
- Winnubst, J., Bas, E., Ferreira, T.A., Wu, Z., Economo, M.N., Edson, P., Arthur, B.J., Bruns, C., Rokicki, K., Schauder, D., et al. (2019). Reconstruction of 1,000 Projection Neurons Reveals New Cell Types and Organization of Long-Range Connectivity in the Mouse Brain. *Cell* 179, 268-281.e13.
- Wolpert, D.M., Miall, R.C., and Kawato, M. (1998). Internal models in the cerebellum. *Trends Cogn. Sci.* 2, 338–347.
- Xie, Z., Li, D., Cheng, X., Pei, Q., Gu, H., Tao, T., Huang, M., Shang, C., Geng, D., Zhao, M., et al. (2022). A brain-to-spinal sensorimotor loop for repetitive self-grooming. *Neuron* 110, 874-890.e7.
- Yizhar, O., Fenno, L.E., Davidson, T.J., Mogri, M., and Deisseroth, K. (2011). Optogenetics in Neural Systems. *Neuron* 71, 9–34.

- Zahler, S.H., Taylor, D.E., Wong, J.Y., Adams, J.M., and Feinberg, E.H. (2021). Superior colliculus drives stimulus-evoked directionally biased saccades and attempted head movements in head-fixed mice. *Elife* 10.
- Zingg, B., Chou, X. lin, Zhang, Z. gang, Mesik, L., Liang, F., Tao, H.W., and Zhang, L.I. (2017). AAV-Mediated Anterograde Transsynaptic Tagging: Mapping Corticocollicular Input-Defined Neural Pathways for Defense Behaviors. *Neuron* 93, 33–47.
- Zingg, B., Peng, B., Huang, J., Tao, H.W., and Zhang, L.I. (2020). Synaptic Specificity and Application of Anterograde Transsynaptic AAV for Probing Neural Circuitry. *J. Neurosci.* 40, 3250–3267.

Publishing Agreement

It is the policy of the University to encourage open access and broad distribution of all theses, dissertations, and manuscripts. The Graduate Division will facilitate the distribution of UCSF theses, dissertations, and manuscripts to the UCSF Library for open access and distribution. UCSF will make such theses, dissertations, and manuscripts accessible to the public and will take reasonable steps to preserve these works in perpetuity.

I hereby grant the non-exclusive, perpetual right to The Regents of the University of California to reproduce, publicly display, distribute, preserve, and publish copies of my thesis, dissertation, or manuscript in any form or media, now existing or later derived, including access online for teaching, research, and public service purposes.

DocuSigned by:

D8DE2AFAD28447B... Author Signature

8/27/2023
Date